Alma Mater Studiorum · University of Bologna

School of Science
Department of Physics and Astronomy
Master Degree in Physics

Ultracold Bose-Fermi mixtures with pairing: quantum phase transition, mechanical stability, and trap confinement

Supervisor:
Prof. Pierbiagio Pieri

Submitted by:
Christian Gualerzi

Academic Year 2021/2022

Ad maiora semper

Abstract

Ultracold dilute gases occupy an important role in modern physics and they are employed to verify fundamental quantum theories in most branches of theoretical physics. The scope of this thesis work is the study of Bose-Fermi (BF) mixtures at zero temperature with a tunable pairing between bosons and fermions. The mixtures are treated with diagrammatic quantum many-body methods based on the so-called T-matrix formalism. Starting from the Fermi-polaron limit, I will explore various values of relative concentrations up to mixtures with a majority of bosons, a case barely considered in previous works. An unexpected quantum phase transition is found to occur in a certain range of BF coupling for mixture with a slight majority of bosons. The mechanical stability of mixtures has been analysed, when the boson-fermion interaction is changed from weak to strong values, in the light of experimental results recently obtained for a double-degenerate Bose-Fermi mixture of ^{23}Na - ^{40}K. A possible improvement in the description of the boson-boson repulsion based on Popov's theory is proposed. Finally, the effects of a harmonic trapping potential are described, with a comparison with the experimental data for the condensate fraction recently obtained for a trapped ^{23}Na - ^{40}K mixture.

Contents

Introduction

At low temperature T, the Maxwell-Boltzmann statistics is no longer able to reproduce the correct statistical behaviour of a particle system. Quantum aspects are dominant when the interparticle distance $n^{-1/3}$ is of the same order of the De Broglie thermal wavelength $\lambda_T = h/\sqrt{2\pi m k_{\mathrm{B}} T}$, that describes the wavelength of wave-packet associated to particles with mass m. Particles are described and classified, in addition to their mass and momentum, by their spins and they can be divided into bosons and fermions. Bosons have an integer spin and follow the so called Bose-Einstein statistics which allow them to occupy macroscopically the lower energy single-particle state. This peculiar behaviour is known as Bose-Einstein condensation (BEC) and it was predicted for the first time in Ref. [1] for massless bosons (phonons) and in Ref. [2] for massive bosons. Under a certain critical temperature, a macroscopic fraction of bosons is expected to occupy the lowest single-particle energy level with zero momentum. Since then, 70 years have passed until the first experimental realization of a BEC with ^{87}Rb [3] and ^{23}Na atoms [4], or with a spin-polarized ^{7}Li gas [5].

On the other hand fermions, with an half-integer spin, are described by the Fermi statistics [6,7]. Generally, a system of N fermions is described by a function which depends on N complete sets of quantum numbers describing the quantum state of each fermion in the system. This function is antisymmetric with respect to the exchange of two of these complete sets of quantum numbers, that means two identical fermions cannot lie in the exact same quantum state. Therefore, in contrast with the bosonic statistics in which an infinite amount of particles can occupy the lowest single-particle energy state, the introduction of a new fermion in the system will cost energy because, in the non-interacting case, the lowest energy states will be already occupied by fermions in the system. The highest energy level of this non-interacting fermion system is given by the so called Fermi Energy $E_{\mathrm{F}} = (6\pi^2\hbar^3 n_{\mathrm{F}})^{2/3}/2m_{\mathrm{F}}$ for a non-interacting three-dimensional Fermi gas with particle density n_{F} and mass m_{F}.

Ultracold gases have been used over the years to study a multitude of in-

teracting system; in particular ultracold dilute gases were employed to verify fundamental quantum theories in most branches of theoretical physics. The diluteness condition is reached when both the De Broglie thermal wavelength λ_T and the interparticle distance $n^{-1/3}$ are greater with respect to the range of the interaction potential r_0. In this case, interactions can be described by a single parameter which depends on the type of interacting atoms and external fields: the s-wave scattering length a. This scattering length can be tuned by varying an external magnetic field applied to the system, by using appropriate Feshbach resonances [8]. This makes possible to explore the whole spectrum of interactions, and the interacting gas of particles can be studied under different interaction regimes.

For example, in 1957 J. Bardeen, L. N. Cooper, and J. R. Schrieffer present in Ref. [9] their famous BCS theory in which pairs of electrons with opposite spin and momentum bind together and condense below a certain critical temperature T_c (the attractive interaction between the electrons being mediated by phonons). BCS was the first microscopic theory of conventional superconductivity, a phenomenon first observed in 1911 by H. K. Onnes. However BCS theory provides a theoretical explanation of conventional superconductivity only in a weak-interaction regime, where electrons in Cooper pairs are weakly-correlated. When the pairing between electrons becomes stronger, they form diatomic molecules with bosonic statistics in a Fermi sea of unpaired electrons. The transition from a BCS state to a BEC regime has been widely studied in last decades both from a theoretical [10–16] and experimental point of view [17–21], with ultracold gases of fermions having been crucial for the experimental test of the theory.

More recently, ultracold gases have been used to investigate a different type of system: ultracold interacting mixtures with different components of bosons (BB), fermions (FF) and bosons-fermions (BF). In this thesis work we will deal with ultracold BF interacting mixtures at zero temperature, with a tunable boson-fermion interaction described by a s-wave scattering length a_{BF}. The interaction between bosons is instead assumed to be repulsive, with scattering length a a_{BB} small and positive. Fano-Feshbach resonances permit to tune the BF interaction throughout the entire resonance from a weak-coupling to a strong-coupling regime. BF mixtures with a tunable pairing interaction between bosons and fermions have been actively investigated in the context of ultracold gases where the tunability of the BF interaction has been realized and exploited in several experiments in past years.

In the weak-coupling limit at $T = 0$ the system can be described as a BEC

of bosons coexisting with a single-component Fermi sea with Fermi energy $E_{\rm F} = (6\pi^2 n_{\rm F})^{2/3}/2m_{\rm F}$, $n_{\rm F}$ being the fermion density, where we have set $\hbar = 1$. A natural length scale is then provided by the Fermi momentum $k_{\rm F} \equiv (6\pi^2 n_{\rm F})^{1/3}$ which, combined with BF scattering length $a_{\rm BF}$, defines the dimensionless coupling strength $g_{\rm F} \equiv (k_{\rm F} a_{\rm BF})^{-1}$ that we will use to characterize BF interaction. For weak BF coupling, $a_{\rm BF}$ is small and negative, i.e. $g_{\rm BF} \ll -1$ and the mixture can be studied using perturbation theory. When the BF interaction strength is increased, a new molecular bound state with a boson and a fermion will appear, and part of the BEC will be depleted in order to form BF bound states. Increasing further the coupling, the BEC may be completely depleted, and the minority species will be present only in fermionic bound states, with a residual fraction of unpaired particles of the majority species.

In particular, one can expect that for a mixture with a majority of fermions the BEC will be completely depleted in the strong-coupling limit, with a quantum phase transition from a phase with a BEC to a normal phase made of molecular bound states and unpaired fermions. This quantum phase transition was recovered also with fixed-node diffusion Monte Carlo (FNDMC) simulations [22]. Moreover for strong BF attraction, $a_{\rm BF}$ is small and positive, such that $g_{\rm BF} \gg 1$, and the system becomes effectively a mixture of molecules and unpaired fermions, which can be described again by perturbation theory (now for a FF mixture).

For a BF mixture with a majority of bosons, the BEC is, in general, not completely depleted in the strong coupling limit. However, as we will see, for mixtures with a small majority of bosons, the BEC condensate goes to zero in a certain range of BF pairing, before going back to the expected non-zero value in the extreme strong-coupling regime.

In order to study the evolution from the weak-coupling to the strong-coupling regime of BF mixtures, a non-perturbative T-matrix approach has been used in past works [23–26]. This approach recovers both weak-coupling and strong-coupling results obtained with a perturbation theory for the two opposite limits and it has been also applied to ultracold gases of fermions for BCS-BEC crossover [16, 27, 28]. These works have shown that, even at zero temperature, a sufficiently strong BF attraction suppresses completely the boson condensate in mixtures where the number of bosons does not exceed the number of fermions, i.e. $x \equiv n_{\rm B}/n_{\rm F} \geq 1$.

My work builds upon and extends previous works on Bose-Fermi ultracold mixtures [23–26], also in the light of experimental results with matched density

obtained recently for a double-degenerate BF mixture of ^{23}Na - ^{40}K [29] in a harmonic trapping potential. In particular, the novel contribution of the present work will be an in-depth analysis of mixtures with $n_{\mathrm{B}} > n_{\mathrm{F}}$, which were barely touched previously only in Ref. [30]. I will analyse the mechanical stability of BF mixtures, when the BF interaction is moved from weak to a strong values. We will see, in particular, the amount of BB repulsion required for the stability as a function of g_{BF}, for various concentrations $n_{\mathrm{B}}/n_{\mathrm{F}}$ and for different mass ratios. As a consequence I will propose an improvement of the theory, with respect to the previous works, in the description of the BB repulsion. Finally I will present a short discussion of the effect of the harmonic trapping potential on BF mixtures.

In the absence of coupling with fermions, and for a small boson gas parameter $\eta = n_{\mathrm{B}} a_{\mathrm{BB}}^3$, bosons can be described by the Bogoliubov theory [31] at $T = 0$. Bogoliubov approximation has been used to compare previous results obtained with T-matrix approximation in the weak-coupling limit and it will be used also in most of results in this thesis work. In last section of chapter 5 the Bogoliubov approximation will be substituted by a first-order Popov approximation [32]. In this approximation also diagrams containing lines associated to non-condensate bosons are considered (at first order) to construct the bosonic self-energies. The result of this new approximation is an increasing of BB repulsion by a mean-field term proportional to the density of non-condensed bosons n'_{B}. This will increase the stability of the BF mixture against mechanical collapse, one of the biggest issues in the experimental realization of ultracold BF mixtures. The mechanical stability has been treated in Ref. [33] using mean-field approximation and in Ref. [34] with a lowest-order constrained variational approximation (LOCV) in a low boson density limit. A numerical result for the stability condition of the system will be presented in this thesis work for mixtures with various density ratios $n_{\mathrm{B}}/n_{\mathrm{F}}$ and mass ratios $m_{\mathrm{B}}/m_{\mathrm{F}}$.

This thesis work is organized as follows. In chapter 1 I will present some results obtained by applying the T-matrix approximation to ultracold BF mixture at both finite and zero temperature. In chapter 2 I will present the most important results for the quantum theory of scattering in three dimensions, with a focus on Fano-Feshbach resonances. In chapter 3 I will introduce in more details the T-matrix formalism with all relevant many-body Feynman's diagrams. The key equations to study a BF mixture will be presented in chapter 4 together with a description of the numerical methods employed. In chapter 5 all the numerical results will be presented and compared, whenever possible, with analytical or perturbative results.

Chapter 1

Previous results for ultracold Bose-Fermi mixtures

1.1 Experimental techinques

In last years, ultracold Bose-Fermi mixtures have been studied rather intensively thanks to new experimental techniques which enable to cool the mixtures to very low temperatures, while varying simultaneously their interaction in a controlled way. Ultracold gases have been explored and studied with atomic traps, that make it possible to confine particles and regulate their densities. One of the most used, is a magnetic trap which uses a magnetic field gradient to trap neutral particles with a magnetic moment $\boldsymbol{\mu}$. By applying an external magnetic field to the system, the energy levels of the atoms are separated in different energy levels due to the Zeeman splitting effect $\Delta E = -\boldsymbol{\mu} \cdot \mathbf{B}$.

When a magnetic field gradient is applied, energy levels associated to atoms whose magnetic momentum is opposite to the external magnetic field increases their energy with the intensity of the magnetic field. These atoms are called low-field seekers, since their energy decreases when the external magnetic decreases. On the contrary, energy levels of those atoms (called high-field seeker atoms) whose magnetic moments are aligned with the external field display an energy decrease as the field intensity increases. A magnetic trap is designed with a local minimum in the magnetic field, which is suitable to trap low-field-seeker atoms whose kinetic energies correspond to temperatures of a fraction of a kelvin. Another trap system is the so-called magneto-optical trap (MOT), which combines a magnetic-field gradient with laser-cooling techniques (with some circularly-polarized red-detuned optical beams) to trap neutral atoms at temperature at the

order of microkelvin.

Laser cooling consists in a number of techniques in which atoms are cooled down by absorption and re-emission of photons, producing a lowering of the momentum of the atoms. The most used technique is the so called "Doppler cooling". In Doppler cooling, two sources emit photons in opposite directions, with frequency tuned slightly below (red-detuned) an electronic transition in the atom. If we consider two different type of atoms, one moving toward and the other moving away from the sources, the atoms which move towards the red-detuned source absorb more photons with respect to the atoms which move away from the light source. Atoms of the first type reduce their momenta by a quantity equal to the momentum of the photon absorbed and they pass to excited states. When they emit photons to come back to their fundamental state, photons will be released with the same amount of momentum, but in a random direction. The net result is a statistical reduction of the momentum of the atoms, and a cooling of the gas. Clearly, the temperature depends on the frequency rate of spontaneous emission of photons, and in most cases Doppler cooling (and in general laser cooling) does not allow for achieving temperatures near the BEC condensation temperature.

Evaporative cooling techniques allow experimentalists to reach much lower temperature with respect to laser cooling. For this reason, evaporative cooling is usually implemented as the final cooling stage in trapped ultracold experiments where radiofrequency fields are used to selectively drive warm atoms, with energy higher than a threshold value, away from the trap by inducing transitions between trapping and non-trapping spin states. The temperature of the gas can be taken to lower and lower values by reducing this threshold energy.

1.2 Theoretical works

One of the advantages of ultracold dilute gases is that the interaction between particles can be characterized and described in terms of a single parameter, namely, the two-particle scattering length a. Typically the scattering length is determined by properties of atoms involved in scattering processes. However, interactions properties between particles in a gas can be modified by external fields which provide the possibility to study interacting gases under different regimes of pairing. In particular, as already mentioned, Fano-Feshbach resonances are an important tool which allows one to regulate fermion-boson pairing. Most recent experiments on Bose-Fermi resonant mixtures are characterized by the smallness of the effective

range parameter r_0 of the interaction potential with respect to both the average interparticle distance and the scattering length [35–38]. This type of "broad" resonance is particularly appealing for the comparison with theoretical calculations. In Ref. [39] a broad Fano-Feshbach resonance has been used to study a ^{40}K-^{41}K mixture with tunable pairing interaction. In Ref. [40, 41] a ^{23}Na-^{40}K mixture has been used to form ultracold weakly bound Feshbach ^{23}Na-^{40}K molecules. In Ref. [42, 43] a ^{40}K-^{87}Rb resonant mixture confined in a magnetic trap lead to the formation of ^{40}K-^{87}Rb molecules. In [44] a ^{23}Na-^{6}Li mixture has been studied.

From a theoretical point of view, Bose-Fermi mixtures in the normal phase, with boson-fermion coupling tuned by a Fano-Feshbach resonance, were analysed in Ref. [23] above the condensation critical temperature T_c. Here, the single BF interaction is completely described by the s-wave scattering length a_{BF}. The system is described by the bosonic and fermionic dressed Green's functions, which have been calculated using a T-matrix formalism, in order recover the expected interactive behaviours both in the strong-coupling and weak-coupling limits. This T-matrix formalism will be described in full details in following chapters. In the weak-coupling limit, bosons and fermions behave like a non-interacting mixtures at low temperature: bosons condense at a critical temperature $T_c = 3.31 n_B^{2/3} m_B$, where n_B and m_B are the boson number density and boson mass, respectively, while fermions fill out the free Fermi sphere with a radius given by the free Fermi momentum $k_F^0 = (6\pi^2 n_F)^{1/3}$. For increasing BF coupling, the boson-fermion correlation was found to gradually decrease the boson condensation temperature and make it eventually vanish at a critical BF coupling g_c when $n_B \leq n_F$. This critical coupling is the quantum critical point which divides a BEC phase from a normal phase, where the condensate is completely depleted.

The values of the critical temperature for the bosonic condensation have been studied numerically with the T-matrix formalism for different relative concentrations $x = n_B/n_F < 1$ as a function of the BF coupling. Starting from the free value given by $T_c = 3.31 n_B^{2/3} m_B$ for a non-interacting system, it was found that T_c decreases with the increasing of the BF coupling until it goes to zero in correspondence of the critical coupling g_c. The most important result is the (approximate) universality of critical coupling value with respect to density imbalance between bosons and fermions, i.e. imb $= (n_B - n_F)/(n_B + n_F)$, as shown in Fig. 1.1, adapted from Fig. 2 of Ref. [23]. Here the temperature is expressed in terms of the Fermi energy $E_F = k_F^2/2m_F$, with the wave vector k_F given by $k_F = [3\pi^2(n_B + n_F)]^{1/3}$, while the BF interaction strength is described by the di-

mensionless quantity $g_{\mathrm{BF}} = (a_{\mathrm{BF}} k_{\mathrm{F}})^{-1}$. The mass ratio is fixed to $m_{\mathrm{B}}/m_{\mathrm{F}} = 1.0$.

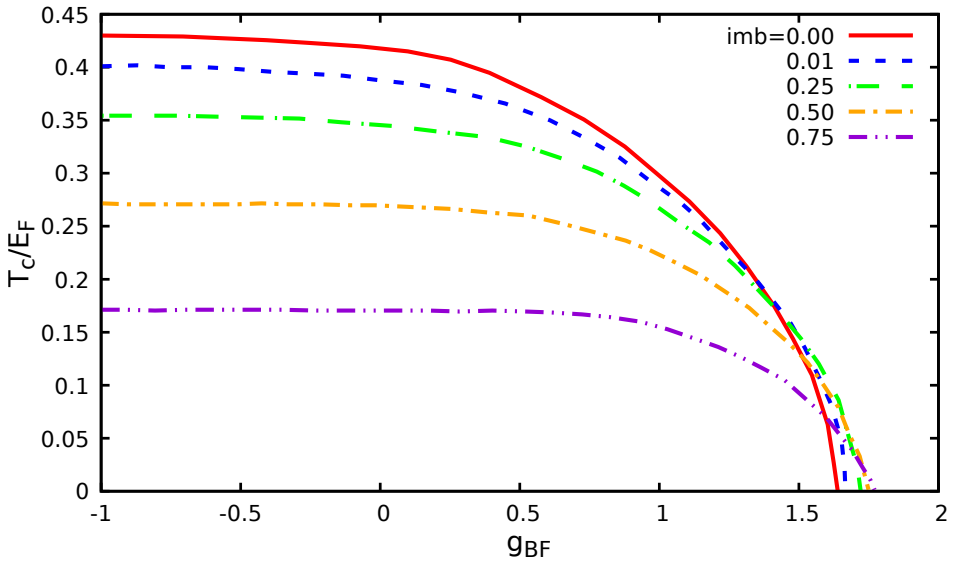

Figure 1.1: Condensation temperature for bosons vs BF coupling $g_{\mathrm{BF}} = (a_{\mathrm{BF}} k_{\mathrm{F}})^{-1}$ for different values of density imbalance $imb = (n_{\mathrm{F}} - n_{\mathrm{B}}) / (n_{\mathrm{F}} + n_{\mathrm{B}})$. The figure is adapted here from Ref. [23], where the mass ratio was fixed to $m_{\mathrm{B}}/m_{\mathrm{F}} = 1.0$.

As reported in the same work, in the limit of a single boson immersed in a Fermi sea, the critical coupling reduces to the value obtained for the polaron-to-molecule transition. In this case g_c can be calculated by solving the problem of a spin-down fermion surrounded by a Fermi sea of spin-up fermions [45].

In Ref. [24] a resonant Bose-Fermi mixture is analysed at finite temperature $T > T_{\mathrm{c}}$ for different mass imbalances. The universality of the critical coupling with respect to the density imbalance was recovered also for different mass ratios. A particular attention was given in Ref. [24] to the case $m_{\mathrm{B}}/m_{\mathrm{F}} = 87/40$ corresponding to a ^{87}Rb-^{40}K mixture. The overall behaviour of the critical temperature as a function g_{BF} is similar to the one reported in Fig. 1.1, with a minor difference corresponding to a slight increase of T_c to values just above the non-interacting critical temperature for intermediate values of imbalance (imb = 0.50 and 0.75) in a coupling range near $g_{\mathrm{BF}} = 0$. This effect can be explained by a hardening of the boson dispersion relation, with a consequent increase of the critical temperature. The competition of this effect with the condensate depletion due to molecular correlations can lead to a minor increase of the critical temperature for certain values of density imbalance which depend on a fine tuning of the mass ratio.

In Ref. [24] the value of g_c as a function of the mass ratio $m_{\mathrm{B}}/m_{\mathrm{F}}$ was studied for different values of density imbalance. It was found a significant dependence of the critical coupling on the mass ratio, especially for $m_{\mathrm{B}}/m_{\mathrm{F}} < 1$. Fig. 1.2

(adapted here from Ref. [24]) shows that, for all values of the density imbalance, g_c decreases monotonically when m_B/m_F increases towards 1, while, for higher values of m_B/m_F, g_c starts to increase with the mass ratio.

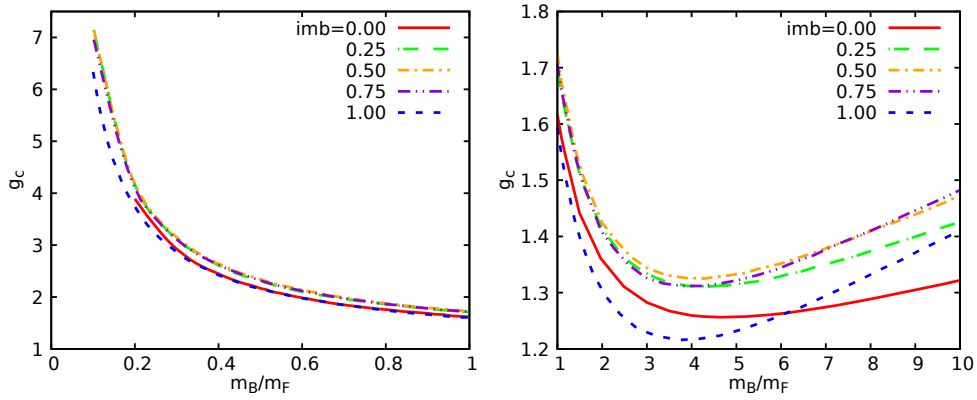

Figure 1.2: Critical coupling g_c as a function of m_B/m_F for various values of density imbalance $(n_F - n_B)/(n_B + n_F)$. In the left panel mass ratios between 0 and 1 are analysed, while in the right panel the behaviour of g_c for higher values of m_B/m_F is reported. Figure adapted from Ref. [24].

A comparison with the critical coupling for the polaron-to-molecule transition has been performed in the limit imb $\to 0$, for both $m_B/m_F > 1$ and $m_B/m_F < 1$. In this limit the BF mixture is equivalent to a strongly imbalanced two-component Fermi gas, since in the limit of one boson immersed in a Fermi sea the statistics of the impurity becomes irrelevant. An analytical expression for g_c using the T-matrix formalism is presented in Ref. [24] and compared with numerical results obtained for $T = 0$. In this thesis work the mass ratio will be fixed (unless otherwise stated) to $m_B/m_F = 23/40$ corresponding to a ^{23}Na-^{40}K mixture. Mixtures with different mass ratios will be treated explicitly in the section of chapter 5 regarding the mechanical stability of BF mixtures.

The quantum-phase transition between a superfluid phase with a condensate fraction $n_0/n_B > 0$ and a normal phase was studied also in [26]. In particular, a dilute BF mixture in the superfluid phase at temperature $T = 0$ was treated using an extension to the condensed phase of the T-matrix Feynman's diagrams used in Ref. [23, 24]. In addition to the BF interaction, a Boson-Boson (BB) point-contact repulsive interaction was considered. It should be stressed that, while a certain amount of BB repulsion is necessary for the mechanical stability of the mixture, the T-matrix calculations can be performed even in the absence of such a repulsion by working at fixed boson and fermion densities. Since, apart from guaranteeing the stability, the effect of the BB repulsion are relatively minor on

the quantities of interest, many results of Ref. [23, 24] were presented by ignoring the BB repulsion. Inclusion of the BB repulsion is instead mandatory when the system is studied in a harmonic trap, where the density is allowed to vary, or with approaches, like quantum Monte Carlo (QMC), where the density cannot be hold constant even in a uniform box-like potential. The BB interaction was described by a mean-field Bogoliubov theory with the inclusion of the corresponding normal and anomalous self-energies.

For various (fixed) values of x, the system is completely described by the bosonic and fermionic chemical potentials $\mu_{\rm B}$ and $\mu_{\rm F}$, and by the condensate fraction $n_0/n_{\rm B}$. The numerical results for the condensate fraction vs $g_{\rm BF}$ obtained in Ref. [26] are reported in Fig. 1.3 for zero BB repulsion (main plot) and for a BB repulsion corresponding to a gas parameter $\eta = n_{\rm B} a_{\rm BB}^3 = 3 \times 10^{-3}$ (inset). In the polaron $x \to 0$ limit the BF mixture can be described as a single impurity immersed in a Fermi sea. In this limit, as argued in Ref. [26], the condensate fraction should reduce to the polaron quasi-particle weight Z of a strongly-polarized two components Fermi gas. For this reason, Fig. 1.3 reports in the main panel also results for Z obtained in Ref. [46] with diagrammatic QMC. The most important

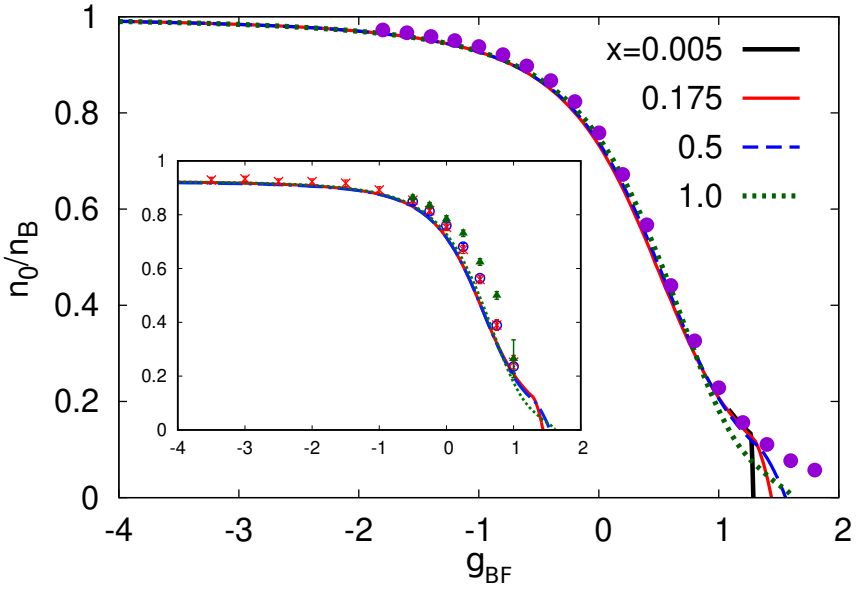

Figure 1.3: Condensate fraction vs $g_{\rm BF}$ extracted from Fig. 3 in Ref. [26] with $m_{\rm B}/m_{\rm F} = 1.0$. In the main panel the gas parameter $\eta = n_{\rm B} a_{\rm BB}^3$ is set to zero. The dottes represent the diagramatic QMC values for quasi-particle weight Z_p obatined in Ref [46]. In the inset the condensate fractions for $\eta = 3 \times 10^{-3}$ obtained in Ref. [26] with zero-temperature T-matrix approximation (FNDMC) are reported with lines (symbols).

result of Ref. [26] is the almost universal behaviour of n_0/n_B (at fixed BB interaction) for different values of x. This universality goes all the way from the weak-coupling limit to $g_{BF} \gtrsim 1$, corresponding to a condensate fraction $n_0/n_B \lesssim 0.2$. The values for n_0/n_B obtained with the T-matrix approximation at zero temperature are compared with those obtained with FNDMC simulations (represented by symbols in the inset of Fig. 1.3) for various x.

In Ref. [25] a BF mixture with $n_B \leq n_F$ in the molecular limit was studied both with a numerical and an analytical approach. When the BF attractive interaction becomes strong, the original Bose-Fermi mixture can be described as a FF mixture of Fermi molecules and unpaired fermions. In the strong-coupling limit, the two-body boson-fermion bind energy $\epsilon_0 = (2m_r a_{BF}^2)^{-1}$ is the dominant energy scale for the system and expansions can be made by using this property. Bosonic and fermionic momentum distribution functions are obtained in the molecular limit starting from T-matrix formalism and making appropriate expansions. For sufficiently low boson concentration, the formation of fermionic molecules forces to zero the bosonic momentum distribution at low momenta, in particular for momenta smaller than the momentum associated to the Fermi sphere of the molecules. On the other hand, in the strong-coupling limit the fermionic momentum distribution consists in a contribution given by the Fermi distribution function of unpaired fermions and a contribution given by a distribution of composite (molecule) fermions, which becomes dominant for large momenta. Expressions for bosonic and fermionic chemical potentials are also derived in the strong-coupling limit using perturbation theory. These results will be used in chapter 5 as a reference for the numerical results obtained in the regime $g_{BF} \gg 1$. In addition, analytic expressions for μ_B and μ_F will be reported also for a system with a majority of bosons.

In Ref. [29] a double-degenerate BF interacting mixture of ^{23}Na and ^{40}K at low temperature was analysed experimentally in order to study the quantum phase transition from a "polaronic" condensate to a molecular Fermi gas with matching of the densities of bosons and fermions. Starting from a weakly interacting mixture, a progressive depletion of the bosonic condensate was observed, leading eventually to a transition into a quantum-degenerate phase of ^{23}Na^{40}K Feshbach molecules and unpaired ^{40}K atoms. This quantum phase transition was realized with a species-dependent dipole trap at 785 nm, which is near-detuned to the D-lines of the ^{40}K atoms, providing a weaker confinement of the ^{23}Na compared to the ^{40}K atoms. In this way the BEC density is lowered and losses due to collisions

between the BEC and Fermi molecules are reduced. In this trap configuration, the trap frequencies of the K atoms are approximately three times greater than the ones of the Na atoms. The BF mixture in Ref. [29] is formed with 2.3×10^5 ^{40}K atoms at a finite temperature $T = 80$ nK and 1.3×10^5 ^{23}Na atoms with a total condensate fraction $N_0/N_B = 0.6$. The quantum phase transition was investigated both with the condensate fraction measured experimentally with a projection of the system onto free atoms and molecules, which are subsequently imaged in time of flight, and with a measure of the Feshbach molecule number. The quantum phase transition was characterized in Ref [29] by an order parameter $\phi = N_0/(N_0 + N_{CB})$, where N_0 represents the number of condensed bosons and N_{CB} represents the number of bosons confined into molecules. The order parameter ϕ as a function of the BF coupling is adapted from Ref. [29] in Fig. 1.4.

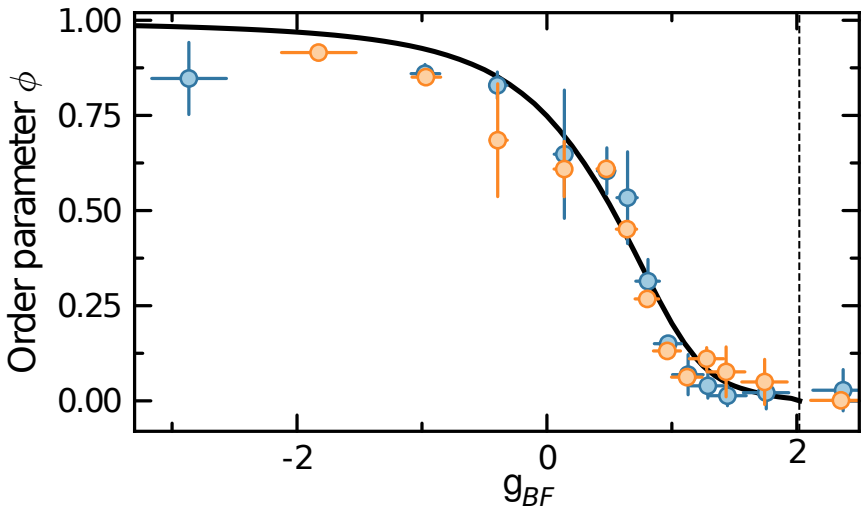

Figure 1.4: Order parameter ϕ as a function of $g_{BF} = (k_F a_{BF})^{-1}$ for boson-fermion density ratios at the center of the trap $n_B/n_F = 0.9$ (orange points) and $n_B/n_F = 1.3$ (blue points). The black solid line represents the condensate fraction n_0/n_B obtained for a homogeneous BF mixture with $n_B = n_F$ and mass ratio $m_B/m_F = 23/40$ using a T-matrix approximation.

The order parameters obtained experimentally for two different peak-density ratios at the center of the trap (points) are compared with the condensate fraction for a density-balanced homogeneous mixture obtained with T-matrix approximation (black solid line). The results of Ref. [29] for the order parameter will be compared in chapter 5 with numerical results for a homogeneous BF mixture at zero temperature obtained with a T-matrix formalism, fixing the density ratios at

$n_B/n_F = 0.9$ and $n_B/n_F = 1.3$. Density profiles of bosons and fermions are also reported in Ref. [29] for a species-dependent dipole trap at 785 nm. In the last part of chapter 5 I will try to implement a harmonic species-dependent confinement to my numerical calculation, and local density profiles will be presented for different values of BF interaction and BB repulsion.

Chapter 2

Scattering theory and resonances

In this chapter I will first give an overview on quantum scattering theory in three dimensions, recalling fundamental equations and deriving the most important results that will describe interaction processes in our BF mixture. I will focus on scattering theory for a point-contact potential, which is the most convenient model to describe short-range interactions in dilute a gas. In the last sections I will discuss Fano-Feshbach resonance, a fundamental tool in the experimental study of ultracold gases.

Quite generally, interactions between atoms might be complicated to model. Simplifications are however possible for dilute systems. In a dilute system the average interatomic distance (which in a three-dimensional gas is given by $n^{-1/3}$, where $n = N/V$ is the number density for a system of N particles in a volume V) is much larger than range r_0 of the interaction between atoms. Ultracold gas physics studies systems of particles at temperatures of the order of microkelvin and with extremely low densities. As a consequence, energies and momenta of particles are small, and the intensity of the potential is completely described by a single quantity: the scattering length a. This scattering length is linked to the specific nature of the atoms that compose the system, but it can be drastically modified by applying an external magnetic field to the system with the introduction of resonances. This dependence of the scattering length on external fields offers the possibility to test the system from weak- to strong-coupling regime simply by tuning the external field.

2.1 Introduction on scattering theory

In quantum mechanics, an interacting system of two distinguishable particles with masses m_1 and m_2 is described by the Schrödinger equation which characterizes completely the physics of the system. Following the procedure of Ref [47], the Schrödinger equation can be separated into two parts using a standard change of coordinates. The first part of the Schrödinger equation describes the motion of the center-of-mass as a free particle with energy E and mass $M = m_1+m_2$. The second part of the Schrödinger equation is the most interesting one, and it describes the relative motion of the two particles. This last part reduces to the motion of a single particle with mass equal to the reduced mass $m_r = m_1 m_2/(m_1 + m_2)$ and subject to a potential $V(\mathbf{r})$, where $V(\mathbf{r})$ is the original interaction potential between the two particles, which depends on the relative distance vector $\mathbf{r}$. This relative motion is described by the wave function $\psi(\mathbf{r})$ which solves the time-independent Schrödinger equation

$$\left[-\frac{\hbar^2\nabla^2}{2m_r} + V(\mathbf{r})\right]\psi(\mathbf{r}) = E\,\psi(\mathbf{r}). \tag{2.1}$$

If we assume $V(\mathbf{r})$ to be a short range potential and the separation between particles to be large, the wave function turns into a superposition between an incoming plane-wave state with relative momentum $\mathbf{p}$ and a spherical outgoing wave. The energy of the system is conserved in an elastic scattering and, by looking at the system in the center-of-mass frame, where it is described by an incoming plane wave of momentum $\mathbf{p}$, is given by $E = E_{\mathbf{p}} = \mathbf{p}^2/2m_r$. The time-independent scattering state can then be expressed as $\left|\psi_{\mathbf{p}}^{(+)}\right\rangle$ in a basis-independent notation, and satisfies the time-independent Schrödinger equation (2.1)

$$\left[\widehat{H}_0 + \widehat{V}\right]\left|\psi_{\mathbf{p}}^{(+)}\right\rangle = E_{\mathbf{p}}\left|\psi_{\mathbf{p}}^{(+)}\right\rangle \tag{2.2}$$

where $\widehat{H}_0 = -\hbar^2\nabla^2/2m_r$. It is easy to verify that the self-consistent solution of Eq. (2.2) is given by

$$\left|\psi_{\mathbf{p}}^{(+)}\right\rangle = |\mathbf{p}\rangle + (E_{\mathbf{p}} - \widehat{H}_0 + i0^+)^{-1}\widehat{V}\left|\psi_{\mathbf{p}}^{(+)}\right\rangle, \tag{2.3}$$

where $|\mathbf{p}\rangle$ is the free solution representing a plane wave which propagates without any scattering process. In Eq. (2.3) the infinitesimal imaginary part $i0^+ \equiv$

$\lim_{\epsilon\to 0^+} i\epsilon$ has been introduced in order to ensure that only outgoing waves are present in the second term of Eq. (2.3), which represent the scattered wave. Now, by multiplying both sides of Eq. (2.3) by $\widehat{V}$ one gets the so-called Lippmann-Schwinger equation

$$\widehat{T}\,|\mathbf{p}\rangle = \widehat{V}\,|\mathbf{p}\rangle + \widehat{V}\frac{1}{E-\widehat{H}_0+i0^+}\widehat{T}\,|\mathbf{p}\rangle\,, \tag{2.4}$$

where we have introduced the two-body scattering T-matrix, as the operator such that

$$\widehat{T}\,|\mathbf{p}\rangle = \widehat{V}\,\big|\psi^{(+)}_{\mathbf{p}}\big\rangle\,. \tag{2.5}$$

Eq. (2.4) must be satisfied for any incoming plane wave $\big|\mathbf{p}\big\rangle$. This implies that the two-body T-matrix must satisfy the self-consistent relation

$$\widehat{T} = \widehat{V} + \widehat{V}\frac{1}{E-\widehat{H}_0+i0^+}\widehat{T}. \tag{2.6}$$

The scattering wave function $\psi^{(+)}_{\mathbf{p}}(\mathbf{r})$ in coordinate representation is given by

$$\psi^{(+)}_{\mathbf{p}}(\mathbf{r}) = \frac{e^{i\mathbf{p}\cdot\mathbf{r}/\hbar}}{(2\pi\hbar)^{3/2}} + \int d\mathbf{r}'\,\langle\mathbf{r}|\,\frac{1}{E_{\mathbf{p}}-\widehat{H}_0+i0^+}\,|\mathbf{r}'\rangle\,\langle\mathbf{r}'|\,\widehat{V}\,\big|\psi^{(+)}_{\mathbf{p}}\big\rangle \tag{2.7}$$

which, for $|\mathbf{r}|$ is much larger that the range of interaction, yields

$$\begin{aligned}
\psi^{(+)}_{\mathbf{p}}(\mathbf{r}) &\simeq \frac{e^{i\mathbf{p}\cdot\mathbf{r}/\hbar}}{(2\pi\hbar)^{3/2}} - \frac{2m_r}{\hbar^2}\frac{e^{ipr/\hbar}}{4\pi r}\int d\mathbf{r}' e^{-i\mathbf{p}'\cdot\mathbf{r}'/\hbar}\,\langle\mathbf{r}'|\,\widehat{V}\,\big|\psi^{(+)}_{\mathbf{p}}\big\rangle \\
&= \frac{e^{i\mathbf{p}\cdot\mathbf{r}/\hbar}}{(2\pi\hbar)^{3/2}} - \frac{2m_r}{\hbar^2}\frac{e^{ipr/\hbar}}{4\pi r}\,\langle\mathbf{p}'|\,\widehat{V}\,\big|\psi^{(+)}_{\mathbf{p}}\big\rangle \\
&= \frac{1}{(2\pi\hbar)^{3/2}}\left[e^{i\mathbf{p}\cdot\mathbf{r}/\hbar} + f(\mathbf{p}',\mathbf{p})\frac{e^{ipr/\hbar}}{r}\right]
\end{aligned} \tag{2.8}$$

where $\mathbf{p}' = p\mathbf{r}/r$ and

$$f(\mathbf{p}',\mathbf{p}) \equiv -(2\pi\hbar)^{3/2}\frac{m_r}{2\pi\hbar^2}\,\langle\mathbf{p}'|\,\hat{V}\,\big|\psi^{(+)}_{\mathbf{p}}\big\rangle \tag{2.9}$$

is the so-called *scattering amplitude*. The scattering wave function in Eq. (2.8) at large distances is thus a superposition of an incoming plane wave with an outgoing spherical wave with an amplitude proportional to the scattering amplitude. Since we are interested in spherically symmetric potentials, the scattering amplitude $f(\mathbf{p}', \mathbf{p})$ depends only on the magnitude of the incoming relative momentum $p = |\mathbf{p}| = |\mathbf{p}'|$ and on the direction given by the scattering angle θ, which is the angle between $\mathbf{p}$ and $\mathbf{p}'$. The scattering amplitude can thus be written as a sum of partial waves

$$f(\mathbf{p}, \mathbf{p}') = f(p, \theta) = \sum_{\ell=0}^{\infty} (2\ell + 1) f_\ell(p) P_\ell(\cos\theta) \tag{2.10}$$

where P_ℓ are the Legendre polynomials. Also the plane-wave part of the scattering wave function can be written as a sum of incoming and outgoing spherical waves

$$e^{i\mathbf{p}\cdot\mathbf{r}} = \sum_{\ell=0}^{\infty} (2\ell + 1) i^\ell j_\ell(pr) P_\ell(\cos\theta) \tag{2.11}$$

where $j_\ell(pr)$ are the spherical Bessel functions. At large distances, the Bessel functions $j_\ell(pr)$ can be approximated by

$$j_\ell(pr) \simeq \frac{\sin(pr - \ell\pi/2)}{pr}. \tag{2.12}$$

Using this approximation for large distances, Eq. (2.11) becomes

$$e^{i\mathbf{p}\cdot\mathbf{r}} \simeq \sum_{\ell=0}^{\infty} (2\ell + 1) \left[\frac{e^{ipr} - e^{-i(pr - \ell\pi)}}{2ipr} \right] P_\ell(\cos\theta) \tag{2.13}$$

and Eq. (2.8) takes the form

$$\psi_{\mathbf{p}}^{(+)} \simeq \frac{1}{(2\pi)^{3/2}} \sum_{\ell=0}^{\infty} (2\ell + 1) \frac{e^{i[pr + 2\delta_\ell(p)]} - e^{-i(pr - \ell\pi)}}{2ipr} P_\ell(\cos\theta) \tag{2.14}$$

where $e^{2i\delta_\ell(k)} \equiv 1 + 2ipf_\ell(k)$ is the phase shift that the scattering wave function acquires at large distances with respect to the free radial wave function. At very low energies it is sufficient to consider s-wave scattering. Indeed in ultracold gases the range of the interaction is much smaller then the thermal de Broglie wavelength and the dominant contribution to the phase shift is given by the partial wave with

zero angular momentum $\ell = 0$, i.e. the so-called s-wave. The s-wave scattering length is defined as

$$a \equiv - \lim_{p \to 0^+} \frac{\delta_0(p)}{p}. \tag{2.15}$$

Using the definition of phase shift in Eq. (2.10) and considering only the $\ell = 0$ contribution, the scattering amplitude does not depend on the angle θ and one gets

$$f(p, \theta) \simeq f_0(p) = \frac{1}{p \cot \delta_0(p) - ip}. \tag{2.16}$$

If we expand the $\cot \delta_0(p)$ for small values of the phase, we get, for small momentum p

$$f(p, \theta) \simeq f_0(p) = -\frac{1}{1/a + ip} \tag{2.17}$$

and in the limit $p \to 0$ the scattering amplitude in Eq. (2.17) approaches $-a$.

2.2 Effective interactions and scattering length

In dilute gases, the range of interparticle interaction is very small with respect to the average interparticle distance $n^{-1/3}$. Under this condition, it is convenient to introduce the concept of effective interaction. Effective interaction describes interactions among long-wavelength degrees of freedom of a system, and can be obtained by integrating out short-wavelength degrees of freedom [48]. In coordinate space, the effective interaction between two particles in a scattering process may be taken with the form of a contact potential

$$U(\mathbf{r_1} - \mathbf{r_2}) = v_0 \delta(\mathbf{r_1} - \mathbf{r_2}), \tag{2.18}$$

where v_0 depends in some way on the s-wave scattering length. A suitable regularization of the contact potential is required to get accurate control of the many-body diagrammatic structure. The δ-function potential can be effectively regularized by introducing an ultraviolet cut-off k_0 and letting $v_0 \to 0$ as $k_0 \to \infty$, in order to keep the scattering length fixed at a chosen finite value. Let us consider the case of a separable contact potential written in momentum space as

$$U(\mathbf{k} - \mathbf{k}') = v_0 w_k w_{k'} \tag{2.19}$$

where $w_k = \Theta(k_0 - |\mathbf{k}|)$. The two-body scattering matrix in momentum space $\langle \mathbf{k}' | \widehat{T} | \mathbf{k} \rangle \equiv T(\mathbf{k}', \mathbf{k}; z)$ which solves the Lippmann-Schwinger Eq. (2.4) takes the form (for $\hbar = 1$)

$$T(\mathbf{k}', \mathbf{k}; z) = v_0 w_k w_{k'} + v_0 w_{k'} \int \frac{d^3k''}{(2\pi)^3} \frac{w_{k''}}{z - k''^2/2m_r} T(\mathbf{k}'', \mathbf{k}; z). \tag{2.20}$$

By setting $T(\mathbf{k}', \mathbf{k}; z) = T(0, 0; z) w_k w_{k'}$, we can rewrite the previous equation as

$$T(0, 0; z) = v_0 + v_0 T(0, 0; z) \int \frac{d\mathbf{k}''}{(2\pi)^3} \frac{w_{k''}^2}{z - k''^2/2m_r} \tag{2.21}$$

and consequently

$$T(0, 0; z) = \left[\frac{1}{v_0} - \int \frac{d\mathbf{k}''}{(2\pi)^3} \frac{w_{k''}^2}{z - k''^2/2m_r} \right]^{-1}. \tag{2.22}$$

Now it is possible to connect the s-wave scattering lenght a with the potential strength v_0 via the ultraviolet cut-off k_0

$$T(0, 0; 0) = \frac{2\pi a}{m_r} = \left[\frac{1}{v_0} + \frac{m_r}{\pi^2} k_0 \right]^{-1} \tag{2.23}$$

and finally

$$v_0 = \left[\frac{m_r}{2\pi a} - \frac{m_r k_0}{\pi^2} \right]^{-1}. \tag{2.24}$$

Now, for large values of k_0, we can express v_0 using a Taylor series expansion at $1/k_0 \simeq 0$

$$v_0 = \frac{\pi^2}{m_r} \frac{1}{k_0} - \frac{\pi^3}{2a m_r} \frac{1}{k_0^2} + ... \tag{2.25}$$

where the dots stand for higher order terms in $1/k_0$. This result will be used in the next chapter when the BF mixture will be treated using Feynman's diagrams within a T-matrix approximation.

2.3 Multiple-channel scattering and Feshbach resonances

Until now, we always considered scattering processes that did not change the internal states of particles involved, described by sets of quantum numbers, such

as those for the spin, angular momentum or excitation state. In treating atom-atom scattering we have so far neglected these internal degrees of freedom, but, in general, scattering processes can modify the internal quantum states of atoms. We shall refer to a possible choice of a couple of these quantum states as a "channel".

Following the description presented in Ref. [48], a couple of atoms involved in a scattering process initially in a state $|\alpha\beta\rangle = |\alpha\rangle \otimes |\beta\rangle$ (where α and β are some set of quantum numbers that identify the internal states of the two atoms) may pass into different final two-particle states $|\alpha'\beta'\rangle$ and, as a consequence, the scattering process becomes a multi-channel problem. The Hamiltonian for two interacting atoms consists of the kinetic energy associated to the centre-of-mass motion, the kinetic energy of the relative motion, the hyperfine and Zeeman energies, and the interaction contribution. We can confine our attention to the relative motion part, described by the Hamiltonian

$$H = H_0 + U(\mathbf{r}) = \frac{\mathbf{p}^2}{2m_r} + H^1_{\text{spin}} + H^2_{\text{spin}} + U(\mathbf{r}) \tag{2.26}$$

where $\mathbf{p}$ is the relative momentum between atoms, $\mathbf{r}$ is the relative distance, H^1_{spin} and H^2_{spin} are the Hamiltonian related to the internal degrees of freedom of atoms 1 and 2, respectively. As mentioned in the previous section, we are interested in short-range interactions. For relative distances far larger than the potential range r_0, the total energy for the initial and final two-atoms states is given by the eigenstate of the non-interacting Hamiltonian H_0. In particular, the total energy for the initial state $|\alpha\beta\rangle$ in the center-of-mass frame is given by

$$E_{\alpha\beta}(\mathbf{k}_{\alpha\beta}) = \frac{\hbar^2 \mathbf{k}^2_{\alpha\beta}}{2m_r} + \epsilon_\alpha + \epsilon_\beta \tag{2.27}$$

where ϵ_α and ϵ_β are the eigenvalues of the internal Hamiltonians H^α_{spin} and H^β_{spin} for atoms in initial internal states $|\alpha\rangle$ and $|\beta\rangle$, and $\mathbf{k}_{\alpha\beta}$ is relative momentum between atoms. Similarly, the total energy for the final state $|\alpha'\beta'\rangle$ takes the form

$$E_{\alpha'\beta'}(\mathbf{k}_{\alpha'\beta'}) = \frac{\hbar^2 \mathbf{k}'^2_{\alpha'\beta'}}{2m_r} + \epsilon_{\alpha'} + \epsilon_{\beta'} \tag{2.28}$$

with the obvious meaning of symbols. The main feature of multiple-channel scattering with respect to a single-channel process is that, in this case, the magnitude of relative incoming momentum $\mathbf{k}_{\alpha\beta}$ is not necessarily equal to those of the relative outgoing momentum $\mathbf{k}_{\alpha'\beta'}$. The relation between initial and final relative

momenta is provided by the condition that the total energy of the system is conserved. This translates into the condition

$$\frac{\hbar^2 \mathbf{k}'^2_{\alpha'\beta'}}{2m_r} = \frac{\hbar^2 \mathbf{k}^2_{\alpha\beta}}{2m_r} + \epsilon_\alpha + \epsilon_\beta - \epsilon_{\alpha'} - \epsilon_{\beta'}. \tag{2.29}$$

When the right-hand-side of Eq. (2.29) is less than zero, the channel $|\alpha'\beta'\rangle$ is said to be closed. In general, an energetically accessible channel is said to be "open", whereas a "closed" channel is forbidden by energy conservation. An elastic scattering processes between two atoms can be dramatically modified if the total energy in an open channel is close to the energy of a bound state in a closed channel. We speak of a Fano-Feshbach (or Feshbach) resonance, when the energy of a bound state in the closed channel approaches the energy of a scattering state in the open channel [8]. Therefore, even a weak coupling between open and closed channels can lead to a strong modification of scattering processes and represents a fundamental tool in dilute ultracold gas of atoms because channels can be coupled together by adjusting an external parameter, for example magnetic fields (magnetic Feshbach resonances) or laser fields (optical Feshbach resonances). In what follows, I will deal mostly with magnetic Feshbach resonances, even if optical Feshbach resonances are a promising alternative to the magnetically tunable resonances [49], since laser light can be focussed and controlled much faster than magnetic fields.

Let us consider a scattering process in which two different channel are associated to two distinct magnetic momenta. The energy difference between the two channels can be manipulated by applying an external magnetic field [50] and, if one of the two channel is closed, the tunable magnetic field can lead the energy difference to zero. Fano-Feshbach resonances make it possible to tune both the magnitude and the sign of the effective atom-atom interaction. By definition of a closed channel, two particles cannot scatter from open-channel states to closed-channel states. However, two particles in an open channel can scatter "virtually" to an intermediate state in a closed channel, which subsequently decays in one of the open channels. This process is the most simple resonant interaction between atoms and one would expect that the main contribution to the scattering length due to this process is a term like

$$a \sim \frac{C}{E - E_{res}} \tag{2.30}$$

where E is the the total energy of the two particles in the open channel and E_{res} is

the energy of a bound state in the closed channel, representing a sort of "threshold energy" for the resonance process. Moreover, from Eq. (2.30) one can see that the coupling between channels gives rise to a repulsive interaction if the energy of the scattering particles is greater than that of the bound state, and an attractive one if it is smaller.

After these qualitative considerations, I will pass now to describe the general formalism for Fano-Feshbach resonances [48]. The total space of states describing the spatial and spin degrees of freedom of an interacting couple of atoms can be divided into two subspaces. The first subspace, P, contains states in the open channels, i.e. two-particles states energetically available, while the second subspace Q contains states in the closed channels, which are forbidden by energy conservation. A general state-vector $|\psi\rangle$ for scattering processes can be divided into the two components

$$|\psi\rangle = |\psi_P\rangle + |\psi_Q\rangle \tag{2.31}$$

where $|\psi_P\rangle = \widehat{\mathcal{P}}\,|\psi\rangle$, $|\psi_Q\rangle = \widehat{\mathcal{Q}}\,|\psi\rangle$ and $\widehat{\mathcal{P}}$,$\widehat{\mathcal{Q}}$ are the projectors for the two subspaces P and Q. These two projection operators can be applied on both sides of the Schrödinger equation $\widehat{H}\,|\psi\rangle = E\,|\psi\rangle$. In particular, by applying $\widehat{\mathcal{P}}$ to both sides of the Schrödinger equation, and using the properties of projectors $\widehat{\mathcal{P}}+\widehat{\mathcal{Q}} = 1$ and $\widehat{\mathcal{P}}\widehat{\mathcal{Q}} = 0$, one gets

$$(E - \widehat{H}_{PP})\,|\psi_P\rangle = \widehat{H}_{PQ}\,|\psi_Q\rangle \tag{2.32}$$

where $\widehat{H}_{PP} = \widehat{\mathcal{P}}\widehat{H}\widehat{\mathcal{P}}$ and $\widehat{H}_{PQ} = \widehat{\mathcal{P}}\widehat{H}\widehat{\mathcal{Q}}$. On the other hand, by applying $\widehat{\mathcal{Q}}$ to both sides of the Schrödinger equation, and using the two previous properties, one gets

$$(E - \widehat{H}_{QQ})\,|\psi_Q\rangle = \widehat{H}_{QP}\,|\psi_P\rangle \tag{2.33}$$

where $\widehat{H}_{QQ} = \widehat{\mathcal{Q}}\widehat{H}\widehat{\mathcal{Q}}$ and $\widehat{H}_{QP} = \widehat{\mathcal{Q}}\widehat{H}\widehat{\mathcal{P}}$. Eqs. (2.32) and (2.33) are coupled equations for the two projected states $|\psi_P\rangle$ and $|\psi_Q\rangle$. One can prove that a solution for Eq. (2.33) is given by

$$|\psi_Q\rangle = (E - \widehat{H}_{QQ} + i\delta)^{-1}\widehat{H}_{QP}\,|\psi_P\rangle\,, \tag{2.34}$$

where the infinitesimal imaginary term $i\delta$ has been added in order to ensure that only outgoing wave are present in the final scattered state. Eq. (2.32) can the be

rewritten, by using Eq. (2.34), as

$$[E - \widehat{H}_{PP} - \widehat{H}'_{PP}]\,|\psi_P\rangle = 0 \tag{2.35}$$

with

$$\widehat{H}'_{PP} = \widehat{H}_{PQ}(E - \widehat{H}_{QQ} + i\delta)^{-1}\widehat{H}_{QP}. \tag{2.36}$$

This $\widehat{H}'_{PP}$ is the term that describes the Fano-Feshbach resonance. It represents an effective interaction in the P subspace due to transitions from that subspace to the Q subspace and back again to the P subspace, with a term in the denominator which diverges for $E \to E_{QQ}$, the energy eigenvalue of the closed channel.

$\widehat{H}_{PP}$ can be written as $\widehat{H}_{PP} = \widehat{H}_0 + \widehat{U}_1$, where $\widehat{H}_0$ contains the kinetic term of the Hamiltonian and all the internal energy degrees of freedom associated to spins and Hyperfine structure (similar to the H_0 term presented in Eq. (2.26)), while $\widehat{U}_1$ is the interaction term for the scattering in the P subspace. However, the total interaction term is not simply given by $\widehat{U}_1$, but it must be taken into account the interaction term related to the temporary transitions to the Q subspace, which is given by Eq. (2.36). The final interaction term then becomes $\widehat{U} \equiv \widehat{U}_1 + \widehat{U}_2$, with $\widehat{U}_2 \equiv \widehat{H}'_{PP}$, and Eq. (2.35) can be rewritten as

$$(E - \widehat{H}_0 - \widehat{U})\,|\psi_P\rangle = 0. \tag{2.37}$$

The two-body scattering matrix $\widehat{T}$ defined in Eq. (2.4), corresponding to the interaction given by $\widehat{U}$ in Eq. (2.37), takes the form

$$\widehat{T} = \widehat{U} + \widehat{U}\widehat{G}_0\widehat{T} \tag{2.38}$$

where $\widehat{G}_0 = (E - \widehat{H}_0 + i\delta)^{-1}$ is the Green's operator for the Schrödinger equation which regulates free propagation of atoms pair. the solution for the operator Eq. (2.38) is

$$\widehat{T} = (1 - \widehat{G}_0\widehat{U})^{-1}\widehat{U}. \tag{2.39}$$

By applying $\widehat{G}_0\widehat{G}_0^{-1}$ and the r.h.s. of Eq. (2.39), and using the fact that the commutator

$$\left[\widehat{U}\widehat{G}_0, (1 - \widehat{G}_0\widehat{U})^{-1}\right] = 0, \tag{2.40}$$

one can rewrite Eq. (2.39) as

$$\widehat{T} = \widehat{U}(1 - \widehat{G}_0\widehat{U})^{-1}. \tag{2.41}$$

By inserting the expression for $\widehat{G}_0$ into (2.39) we obtain

$$\begin{aligned}\widehat{T} &= (E + i\delta - \widehat{H}_0)(E + i\delta - \widehat{H}_0 - \widehat{U})^{-1}\widehat{U} \\ &= \widehat{T}_1 + (1 - \widehat{U}_1\widehat{G}_0)^{-1}\widehat{U}_2(1 - \widehat{G}_0\widehat{U})^{-1}\end{aligned} \tag{2.42}$$

where in the second line of the previous equation we have introduced $\widehat{T}_1 = \widehat{U}_1 + \widehat{U}_1\widehat{G}_0\widehat{T}_1$, which can be interpreted as the T-matrix in the P subspace if $\widehat{U}_2 = 0$, i.e. if transitions to the Q subspace are neglected. With this expression for the T-matrix operator we can obtain the scattering amplitude introduced in Eq. (2.9) by calculating the matrix element of $\widehat{T}$ between plane-wave states. Then the scattering length a is given (up to a multiplicative numerical factor) by taking the relative momenta to zero. We have

$$\langle \mathbf{k}' | \, \widehat{T} \, | \mathbf{k} \rangle = \langle \mathbf{k}' | \, \widehat{T}_1 \, | \mathbf{k} \rangle + \langle \mathbf{k}' | \, (1 - \widehat{U}_1\widehat{G}_0)^{-1}\widehat{U}_2(1 - \widehat{G}_0\widehat{U})^{-1} \, | \mathbf{k} \rangle \tag{2.43}$$

where $(1 - \widehat{G}_0\widehat{U})^{-1} \, |\mathbf{k}\rangle \equiv |\mathbf{k}; U, +\rangle$ represents the outgoing state at large separations, which consists of a plane wave and a spherical wave. On the other hand, the hermiticity of $\widehat{U}_1$ and $\widehat{H}_0$ allows us to write $\langle \mathbf{k}' | \, (1 - \widehat{U}_1\widehat{G}_0)^{-1} \equiv [|\mathbf{k}'; U_1, -\rangle]^\dagger$, a state containing incoming spherical waves at large distances. The general expression for the scattering amplitude in the P subspace results

$$\langle \mathbf{k}' | \, \widehat{T} \, | \mathbf{k} \rangle = \langle \mathbf{k}' | \, \widehat{T}_1 \, | \mathbf{k} \rangle + \langle \mathbf{k}'; U_1, - | \, \widehat{U}_2 \, | \mathbf{k}; U, + \rangle \, . \tag{2.44}$$

If we consider only first order terms in $\widehat{U}_2$, then the $\widehat{U}$ appearing in outgoing state $|\mathbf{k}; U, +\rangle$ can be replaced by $\widehat{U}_1$, which gives a matrix element between plane-wave states

$$\langle \mathbf{k}' | \, \widehat{T} \, | \mathbf{k} \rangle = \langle \mathbf{k}' | \, \widehat{T}_1 \, | \mathbf{k} \rangle + \langle \mathbf{k}'; U_1, - | \, \widehat{U}_2 \, | \mathbf{k}; U_1, + \rangle \, . \tag{2.45}$$

In the limit of zero relative momenta between particle, this reduces to the s-wave scattering length

$$\frac{2\pi\hbar^2}{m_r} a = \frac{2\pi\hbar^2}{m_r} a_{\mathrm{NR}} + \langle \mathbf{0}; U_1, - | \, \widehat{U}_2 \, | \mathbf{0}; U_1, + \rangle \, . \tag{2.46}$$

Finally by using the identity $1 = \sum_n |\psi_n\rangle \langle\psi_n|$, where the states $|\psi_n\rangle$ form a complete set in the Q subspace with energy E_n, one has

$$\frac{2\pi\hbar^2}{m_r}a = \frac{2\pi\hbar^2}{m_r}a_{\mathrm{NR}} + \sum_n \frac{|\langle\psi_n| \widehat{H}_{QP} |\mathbf{0}; U_1, +\rangle|^2}{E - E_n}. \tag{2.47}$$

In the isolated resonance approximation [51], only a single bound state $|\psi_{\mathrm{res}}\rangle$ of the closed channel gives a significant contribution to the resonance, thus Eq. (2.47) reduces to

$$\frac{2\pi\hbar^2}{m_r}a = \frac{2\pi\hbar^2}{m_r}a_{\mathrm{NR}} + \frac{|\langle\psi_{\mathrm{res}}| \widehat{H}_{QP} |\mathbf{0}; U_1, +\rangle|^2}{E - E_{\mathrm{res}}}. \tag{2.48}$$

This final expression for the s-wave scattering length is given by the sum between the single channel non-resonant (NR) scattering length a_{NR} and a resonant term which becomes dominant (see Eq. (2.36)) for E approaching the resonant energy E_{res} given by the bound-state energy in closed channel. For a magnetically tuned Feshbach resonance the difference $E - E_{\mathrm{res}}$ can be expanded as

$$E - E_{\mathrm{res}} \simeq (\mu_{\mathrm{res}} - \mu_\alpha - \mu_\beta)(B - B_0) \tag{2.49}$$

where $\mu_i = -\frac{\partial \epsilon_i}{\partial B}$ with $i = \alpha, \beta$ are the magnetic moments for the two atoms in state i in the open channel, while $\mu_{\mathrm{res}} = -\frac{\partial E_{\mathrm{res}}}{\partial B}$ is the magnetic moment of the bound state. The parameter B_0 indicates the position of the Feshbach resonance at which the scattering length diverges.

Chapter 3

T-matrix formalism for ultracold BF mixtures

In this chapter I will introduce the T-matrix formalism which was shown to be a good approximation in the study of ultracold gases with pairing interactions. In the first section, I will introduce Green's functions for a generic single-component many-body system. Then, I will concentrate on BF mixtures at zero temperature with a diagrammatic analysis of BF interactions and single particle propagators. Finally, we will obtain a set of integral equations that characterize the BF mixture for given BF and BB couplings.

3.1 Introduction to Green's function formalism in many-body theory

When we are dealing with a quantum many-body system, the Schrödinger equation, which describes the quantum evolution of each single particle in the system, is in general impossible to be solved, especially when lowest order in perturbation theory fails to recover the physical behaviour of the system. From this point of view, a better approach to describe a many-body system is provided by the quantum theory of many-particle system based on quantum field theory and Green's function formalism. Green's functions provide the most important statistical information of the system and they are directly linked to all thermodynamical quantities. Green's functions are defined from quantum field operators in the so-called Heisenberg representation, in which the quantum field becomes a time-dependent operator which acts on a time-independent quantum state. The expression of the quantum field operator in the Heisenberg representation derives from the usual

time-independent quantum field operator in the Schrödinger representation, for a single-component gas, as

$$\widehat{\psi}_{\rm K}(\mathbf{x},\tau) = e^{\widehat{K}\tau}\widehat{\psi}(\mathbf{x})e^{-\widehat{K}\tau} \tag{3.1}$$

$$\widehat{\psi}^{\dagger}_{\rm K}(\mathbf{x},\tau) = e^{-\widehat{K}\tau}\widehat{\psi}^{\dagger}(\mathbf{x})e^{\widehat{K}\tau} \tag{3.2}$$

where $\tau = it/\hbar$, and $\widehat{K} = \widehat{H} - \mu\widehat{N}$ is the grand canonical Hamiltonian operator for a single-component gas. The single-particle "dressed" Green's function at finite temperature T is then defined as

$$G(\mathbf{x},\tau;\mathbf{x}',\tau') \equiv -{\rm Tr}\left\{\widehat{\rho}_G {\rm T}_\tau\left[\widehat{\psi}_{\rm K}(\mathbf{x},\tau)\widehat{\psi}^{\dagger}_{\rm K}(\mathbf{x}',\tau')\right]\right\} \tag{3.3}$$

where $\widehat{\rho}_G = Z_G^{-1}e^{-\beta\widehat{K}}$ and Z_G is the grand canonical partition function $Z_G = {\rm Tr}e^{-\beta\widehat{K}}$, with $\beta = 1/k_{\rm B}T$. In Eq. (3.3), ${\rm T}_\tau$ is the τ-ordering operator, and the trace is taken over a complete set of states in the Hilbert space. In a similar way one can define the single-particle free (or "bare") Green's function as

$$G^0(\mathbf{x},\tau;\mathbf{x}',\tau') \equiv -{\rm Tr}\left\{\widehat{\rho}_{G_0} {\rm T}_\tau\left[\widehat{\psi}_{\rm K_0}(\mathbf{x},\tau)\widehat{\psi}^{\dagger}_{\rm K_0}(\mathbf{x}',\tau')\right]\right\} \tag{3.4}$$

where $\widehat{K}_0 = \widehat{H}_0 - \mu\widehat{N}$ and $\widehat{\rho}_{G_0} = Z_{G_0}^{-1}e^{-\beta\widehat{K}_0}$. The finite-temperature bosonic (fermionic) Green's function is periodic (antiperiodic) with respect to τ, with a period $\beta\hbar$. Then, for a homogeneous interacting system with a time-independent potential, the dressed Green's function can be written in term of its Fourier transform with respect to both space and time as

$$G(\mathbf{x},\mathbf{x}',\tau) = (\beta\hbar)^{-1}\int\frac{d\mathbf{k}}{(2\pi)^3}e^{i\mathbf{k}\cdot(\mathbf{x}-\mathbf{x}')}\sum_n e^{-i\omega_n\tau}G(\mathbf{k},\omega_n) \tag{3.5}$$

where

$$\omega_n = \begin{cases}\dfrac{2n\pi}{\beta\hbar}, & \text{for bosons}\\[2ex] \dfrac{(2n+1)\pi}{\beta\hbar}, & \text{for fermios}\end{cases} \tag{3.6}$$

are the so-called "Matsubara" frequencies [52]. In our diagrammatic theory at zero temperature we take the limit $T \to 0$ of this Matsubara formalism at finite

temperature. We will work thus on the *imaginary* frequency axis rather than on the real frequency axis, as is more standard at $T = 0$ [52]. This trick is particularly useful to avoid singularities of the Green's function on the real frequency axis.

Using the Wick theorem to rewrite the time-ordered product in Eq. (3.3), the dressed Green's function can be expressed as a sum of terms containing the bare Green's functions and the interacting potential. Each term in this summation can be represented by a Feynman's diagram containing only solid lines, corresponding to bare Green's function, and broken lines, corresponding to interaction terms. Dyson's equation allows us to express the dressed Green's function as the sum of bare Green's function with all Feynman's diagrams connecting with other parts of the diagrams by an incoming and outgoing solid line. These types of Feynman's diagrams are called "self-energies" Σ. Among all the different types of Feynman's diagrams with an incoming and outgoing solid line, the most interesting ones are the so-called "proper self-energies" $\Sigma^\star$: their peculiarity is that they cannot be separated into two disconnected parts by cutting a single solid line. Dyson's equation in momentum space for a single-component gas reads as

$$G(\mathbf{k}, \omega_n) = G^0(\mathbf{k}, \omega_n) + G^0(\mathbf{k}, \omega_n)\Sigma^\star(\mathbf{k}, \omega_n)G(\mathbf{k}, \omega_n). \tag{3.7}$$

In a single-component gas of bosons in the condensed phase, the Dyson's equation (3.7) acquires a matrix form, where the the diagonal (off-diagonal) elements of G are usually called normal (anomalous) Green's functions.

3.2 Ultracold BF mixtures and minimal Hamiltonian

We consider a homogeneous three-dimensional mixture at temperature $T = 0$ formed by single-component fermions, with particle density n_{F}, interacting with bosons, with particle density n_{B}. Since fermions are identical, we will neglect fermion-fermion scattering interaction: the first contribution to this scattering process for a short range interaction is given by the p-wave term, which can be neglected for dilute ultracold gases. On the other hand, we will consider boson-fermion (BF) and boson-boson (BB) short range interactions, with the BF interaction tuned by a Fano-Feshbach resonance. In particular, we will focus on broad Fano-Feshbach resonances, for which the effective range of the potential is much smaller than the average interparticle distance and the corresponding

scattering length. Under these assumptions, the mixture can be described by a minimal Hamiltonian, where only BF and BB scattering interactions are taken into account. The minimal Hamiltonian takes the form

$$
\begin{aligned}
H = & \sum_{\mathrm{s=B,F}} \int d\mathbf{r}\, \psi_{\mathrm{s}}^{\dagger}(\mathbf{r}) \left(-\frac{\nabla^2}{2m_{\mathrm{s}}} - \mu_{\mathrm{s}} \right) \psi_{\mathrm{s}}(\mathbf{r}) \\
& + v_0^{\mathrm{BF}} \int d\mathbf{r}\, \psi_{\mathrm{B}}^{\dagger}(\mathbf{r}) \psi_{\mathrm{F}}^{\dagger}(\mathbf{r}) \psi_{\mathrm{F}}(\mathbf{r}) \psi_{\mathrm{B}}(\mathbf{r}) \\
& + \frac{1}{2} \int d\mathbf{r} \int d\mathbf{r}'\, \psi_{\mathrm{B}}^{\dagger}(\mathbf{r}) \psi_{\mathrm{B}}^{\dagger}(\mathbf{r}') U_{\mathrm{BB}}(\mathbf{r}-\mathbf{r}') \psi_{\mathrm{B}}(\mathbf{r}) \psi_{\mathrm{B}}(\mathbf{r}')
\end{aligned}
\tag{3.8}
$$

where (for s = B, F) the field operators $\psi_{\mathrm{s}}^{\dagger}(\mathbf{r})$ and $\psi_{\mathrm{s}}(\mathbf{r})$ create and destroy, respectively, a particle of mass m_{s} at position $\mathbf{r}$. The first line corresponds to the grand canonical Hamiltonian for non interacting BF mixtures, where μ_s is the chemical potential for s = B, F, while the second and third lines in Eq. (3.8) represent BF and BB interactions. In particular, the BF interaction is described by an attractive point-contact interaction, which is suitably regularized by taking the limit $k_0 = 1/r_0 \to \infty$ of Eq. (2.24) for v_0^{BF}. The BB interaction U_{BB} is instead purely repulsive and short-ranged. In this case, the regularization (2.24) cannot be used since it is valid only for attractive short-range interactions. However, since the BB repulsion is assumed to be weak so that one can work at lowest order in perturbation theory, a simple approach where $U_{\mathrm{BB}}(\mathbf{r}-\mathbf{r}')$ is replaced by the effective interaction $\frac{4\pi a_{\mathrm{BB}}}{m_{\mathrm{B}}}\delta(\mathbf{r}-\mathbf{r}')$ in perturbative expressions can safely be taken.

3.3 T-matrix formalism

Let us focus on BF interactions. The formalism is developed entirely within the ladder diagrams or T-matrix approximation, i.e. a diagrammatic calculation that selects only the class of Feynman's diagrams formed by repeated BF interactions. This results in a sort of ladder, where each rung represents a BF interaction line and the two side rails are associated to bosons and fermions lines. In chapter 2 we have introduced the concept of two-body T-matrix to describe two-body scattering processes. In a many-body system the T-matrix can be seen (up to a numerical factor) as a scattering amplitude generalized in a background "medium" formed by the other particles in the system. The choice of the T-matrix class of diagrams

is dictated mainly by the fact that they represent the dominant contributions in both the weak-coupling limit $a_{\rm BF} \to 0^-$ and in the opposite strong-coupling limit $a_{\rm BF} \to 0^+$. Moreover, in Ref. [27, 28] the T-matrix approximation has been shown to be a good approximation to describe also the behaviour of two-component FF mixture in presence of a Fano-Feshbach resonance.

In order to arrive to the complete expression for the T-matrix, we firstly consider our system in the normal phase, where the condensed fraction of bosons n_0 is null, corresponding to a strong BF coupling regime for a BF mixture with a majority of fermions. In this case the interaction between bosons and fermions given by the T-matrix can be expressed in terms of Γ-matrix $\Gamma(\mathbf{P}, \Omega)$, where $\mathbf{P}$ and Ω are the sums of incoming momenta and frequencies for bosons and fermions. The diagram representing $\Gamma(\mathbf{P}, \Omega)$ is reported in Fig. 3.1. The expression for $\Gamma(\mathbf{P}, \Omega)$

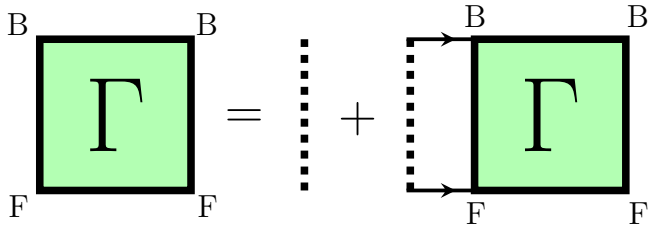

Figure 3.1: Γ-matrix diagram which describes BF interaction in a normal phase. Each dotted line represents the bare BF point-contact potential with strength $v_0^{\rm BF}$, while lines with arrow are associated to the bare bosonic and fermionic propagators $G_{\rm B}^0$ and $G_{\rm F}^0$.

can be directly derived using Feynman's rules in momentum space:

$$\Gamma(\mathbf{P}, \Omega) = v_0^{\rm BF} - v_0^{\rm BF}\Gamma(\mathbf{P}, \Omega) \int \frac{d\mathbf{q}}{(2\pi)^3}\Theta(q_0 - |\mathbf{q}|)\times \\ \times \int \frac{d\omega}{2\pi} G_{\rm F}^0(\mathbf{P} - \mathbf{q}, \Omega - \omega) G_{\rm B}^0(\mathbf{q}, \omega) \tag{3.9}$$

where we have used the regularization discussed before for a point-contact potential (see Eq. (2.19)), where the ultraviolet cut-off q_0 appearing in the Θ-function will be sent eventually to infinity, while scaling accordingly $v_0^{\rm BF}$ with the equation

$$v_0^{\rm BF} = \left[\frac{m_r}{2\pi a_{\rm BF}} - \frac{m_r q_0}{\pi^2} \right]^{-1}. \tag{3.10}$$

$G_{\rm F}^0$ and $G_{\rm B}^0$ are the fermionc and bosonic non-interacting Green's functions whose

expression is given by

$$G_{\rm F}^0(\mathbf{q},\omega) = \left[i\omega - \frac{q^2}{2m_{\rm F}} + \mu_{\rm F} \right]^{-1} = \frac{1}{i\omega - \xi_{\mathbf{q}}^F} \tag{3.11}$$

$$G_{\rm B}^0(\mathbf{q},\omega) = \left[i\omega - \frac{q^2}{2m_{\rm B}} + \mu_{\rm B} \right]^{-1} = \frac{1}{i\omega - \xi_{\mathbf{q}}^B} \tag{3.12}$$

where $m_{\rm s}$ and $\mu_{\rm s}$ (for s = B, F) are the mass and the chemical potential for bosons and fermions. From Eq. (3.9) one can write $\Gamma(\mathbf{P},\Omega)$ as

$$\Gamma(\mathbf{P},\Omega) = \left[\frac{1}{v_0^{\rm BF}} + \int \frac{d\mathbf{q}}{(2\pi)^3} \Theta(q_0 - |\mathbf{q}|) \int \frac{d\omega}{2\pi} G_{\rm F}^0(\mathbf{P}-\mathbf{q}, \Omega-\omega) G_{\rm B}^0(\mathbf{q},\omega) \right]^{-1}. \tag{3.13}$$

The integral in ω can be handled by performing a contour integral in the complex plane. The result is given by the sum of the residues of the two poles inside the contour. These poles originate from the bosonic and fermionic bare Green's functions. One obtains:

$$\Gamma(\mathbf{P},\Omega) = \left[\frac{1}{v_0^{\rm BF}} + \int \frac{d\mathbf{q}}{(2\pi)^3} \Theta(q_0 - |\mathbf{q}|) \frac{1 - \Theta(-\xi_{\mathbf{P}-\mathbf{q}}^{\rm F}) - \Theta(-\xi_{\mathbf{q}}^{\rm B})}{\xi_{\mathbf{P}-\mathbf{q}}^{\rm F} + \xi_{\mathbf{q}}^{\rm B} - i\Omega} \right]^{-1}. \tag{3.14}$$

Let us focus on the integral in Eq. (3.14). From a power counting it is clear that this integral diverges in the limit $|\mathbf{q}| \to \infty$ if the ultraviolet cut-off q_0 is taken to infinity. If we consider the contribution given by large $|\mathbf{q}|$, i.e. neglecting the chemical potentials and the frequency $i\Omega$ compared to q^2/m_r, we obtain

$$\int \frac{d\mathbf{q}}{(2\pi)^3} \Theta(q_0 - |\mathbf{q}|) \frac{1 - \Theta(-\xi_{\mathbf{P}-\mathbf{q}}^{\rm F}) - \Theta(-\xi_{\mathbf{q}}^{\rm B})}{\xi_{\mathbf{P}-\mathbf{q}}^{\rm F} + \xi_{\mathbf{q}}^{\rm B} - i\Omega} \simeq \int_{|\mathbf{q}|<q_0} \frac{d\mathbf{q}}{(2\pi)^3} \frac{2m_r}{q^2} \tag{3.15}$$

$$= \frac{m_r}{\pi^2} q_0. \tag{3.16}$$

If we subtract the r.h.s. of Eq. (3.15) to Eq. (3.14) and add Eq. (3.16) to the same expression we obtain

$$\Gamma(\mathbf{P},\Omega) = \frac{1}{\dfrac{1}{v_0^{\rm BF}} + \displaystyle\int \frac{d\mathbf{q}}{(2\pi)^3} \left[\frac{1 - \Theta(-\xi_{\mathbf{P}-\mathbf{q}}^{\rm F}) - \Theta(-\xi_{\mathbf{q}}^{\rm B})}{\xi_{\mathbf{P}-\mathbf{q}}^{\rm F} + \xi_{\mathbf{q}}^{\rm B} - i\Omega} - \frac{2m_r}{q^2} \right] + \frac{m_r}{\pi^2} q_0} \tag{3.17}$$

where the term $\Theta(q_0 - |\mathbf{q}|)$ has been removed from the integrand since now the integral converges in the limit $q_0 \to \infty$. Recalling the result for the bare strength of a contact potential in Eq. (3.10), the expression for the T-matrix in the normal phase becomes

$$\Gamma(\mathbf{P},\Omega) = \frac{1}{\dfrac{m_r}{2\pi a_{\rm BF}} + \displaystyle\int \frac{d\mathbf{q}}{(2\pi)^3}\left[\frac{1-\Theta(-\xi^{\rm F}_{\mathbf{P}-\mathbf{q}})-\Theta(-\xi^{\rm B}_{\mathbf{q}})}{\xi^{\rm F}_{\mathbf{P}-\mathbf{q}}+\xi^{\rm B}_{\mathbf{q}}-i\Omega} - \frac{2m_r}{q^2}\right]} \tag{3.18}$$

where $a_{\rm BF}$ is the boson-fermion scattering length. Let us focus on the integral over the momentum $\mathbf{q}$ in Eq. (3.18). Notice that $\Theta(-\xi^{\rm B}_q) = 0$ in Eq. (3.18), since we require that $\mu_{\rm B} < 0$ in the calculation of the T-matrix. The contribution to the integral associated to the term $\Theta(-\xi^{\rm F}_{\mathbf{P}-\mathbf{q}})$ can be evaluated analytically, and it gives

$$\begin{aligned}\int \frac{d\mathbf{q}}{(2\pi)^3}\frac{\Theta(-\xi^{\rm F}_{\mathbf{P}-\mathbf{q}})}{\xi^{\rm F}_{\mathbf{P}-\mathbf{q}}+\xi^{\rm B}_{\mathbf{q}}-i\Omega} &= \frac{m_{\rm B}\left(k^2_{\mu_{\rm F}}-k^2_{\mathbf{P}}-k^2_{\Omega}\right)}{8\pi^2 P}\log\left[\frac{(k_{\mu_{\rm F}}+k_{\mathbf{P}})^2-k^2_{\Omega}}{(k_{\mu_{\rm F}}-k_{\mathbf{P}})^2-k^2_{\Omega}}\right] \\ &- \frac{m_r k_\Omega}{4\pi^2}\left\{\log\left[\frac{(k_{\mu_{\rm F}}+k_\Omega)^2-k^2_{\mathbf{P}}}{k^2_{\mathbf{P}}-(k_{\mu_{\rm F}}-k_\Omega)}\right] + i\pi\,\mathrm{sgn}(\Omega)\right\} \\ &+ \frac{m_r k_{\mu_{\rm F}}}{2\pi^2}\end{aligned} \tag{3.19}$$

where we have set

$$k_{\mu_{\rm F}} \equiv \sqrt{2m_{\rm F}\mu_{\rm F}} \tag{3.20}$$

$$k_{\mathbf{P}} \equiv \frac{m_{\rm F}}{M}|\mathbf{P}| \tag{3.21}$$

$$k_\Omega \equiv \sqrt{-\frac{m_r}{M}|\mathbf{P}|^2 + 2m_r\mu + 2im_r\Omega} \tag{3.22}$$

with $M = m_{\rm B} + m_{\rm F}$ and $\mu = (\mu_{\rm B} + \mu_{\rm F})/2$. The remaining part in the denominator of Eq. (3.18) is referred as $\Gamma^{\rm SC}$, and is given by

$$\begin{aligned}\Gamma^{\rm SC}(\mathbf{P},\Omega) &\equiv \frac{m_r}{2\pi a_{\rm BF}} + \int \frac{d\mathbf{q}}{(2\pi)^3}\left[\frac{1}{\xi^{\rm F}_{\mathbf{P}-\mathbf{q}}+\xi^{\rm B}_{\mathbf{q}}-i\Omega} - \frac{2m_r}{q^2}\right] \\ &= \frac{m_r}{2\pi a_{\rm BF}} - \frac{m_r^{3/2}}{\sqrt{2}\,\pi}\sqrt{\frac{P^2}{2M}-2\mu-i\Omega}.\end{aligned} \tag{3.23}$$

$\Gamma^{\rm SC}$ represents the main contribution to the T-matrix in a strong-coupling (molecular) situation. By performing an analytical extension of $\Gamma^{\rm SC}(\mathbf{P},\Omega)$ to the whole complex plane by $i\Omega \to z$ we can study the analytical properties of $\Gamma^{\rm SC}(\mathbf{P},z)$. This analysis will become essential in the following chapter, when the T-matrix formalism will be solved with both numerical integrations and analytical integrations in the complex plane. $\Gamma^{\rm SC}(\mathbf{P},z)$ presents a branch cut for $\mathrm{Re}z \geq \frac{P^2}{2M} - \mu$ and a single pole for $\mathrm{Re}z = \frac{P^2}{2M} - \mu_{\rm CF}$. Here $\mu_{\rm CF} = \mu + \epsilon_0$ can be interpreted as the chemical potential associated to BF molecules which form in the strong-coupling regime. These molecules obey to the fermion statistics and will be referred to as "composite fermions" (CF). $\epsilon_0 = (2m_r a_{\rm BF}^2)^{-1}$ is the binding energy for the BF bound state.

Let us move now to study the BF interaction for a condensate density $n_0 > 0$. The Feynman's diagram for the T-matrix in the condensed phase is reported in Fig. 3.2. The full line with an arrow corresponds to a bare fermionic Green's

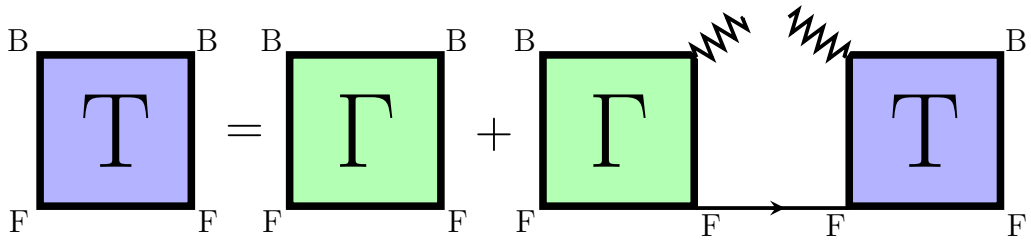

Figure 3.2: T-matrix diagram in condensed phase. The Γ-matrix blocks correspond to the diagram in Fig. 3.1. The line with an arrow, which connects the Γ-matrix and the T-matrix in the right-hand-side, is associated to the bare fermionic Green's function $G_{\rm F}^0$. Each zig-zag line gives a contribution $\sqrt{n_0}$.

functions $G_0^{\rm F}$, while the zig-zag lines correspond to a condensate factor $\sqrt{n_0}$. Following Feynman's rules in momentum space we arrive to the following equation for $\mathrm{T}(\mathbf{P},\Omega)$

$$\mathrm{T}(\mathbf{P},\Omega) = \Gamma(\mathbf{P},\Omega) + \Gamma(\mathbf{P},\Omega) n_0 G_{\rm F}^0(\mathbf{P},\Omega)\mathrm{T}(\mathbf{P},\Omega), \tag{3.24}$$

which has the formal solution

$$\mathrm{T}(\mathbf{P},\Omega) = \frac{1}{\Gamma(\mathbf{P},\Omega)^{-1} - n_0 G_{\rm F}^0(\mathbf{P},\Omega)}. \tag{3.25}$$

3.4 Self-energies and propagators

The next step in studying our zero temperature BF mixture consists in a selection of a specific class of diagrams that describes modifications of the single particle energies due to the interactions between bosons and fermions. As anticipated in previous section, Feynman's diagrams with an incoming and outgoing free propagator line are called "self-energies". Proper self-energy determines the dressed Green's function G through the Dyson's equation

$$G(\mathbf{P},\Omega) = G^0(\mathbf{P},\Omega) + G^0(\mathbf{P},\Omega)\Sigma^\star(\mathbf{P},\Omega)G(\mathbf{P},\Omega), \tag{3.26}$$

and thus

$$G(\mathbf{P},\Omega) = \frac{1}{G^0(\mathbf{P},\Omega)^{-1} - \Sigma^\star(\mathbf{P},\Omega)}. \tag{3.27}$$

In this section I will present the diagrams which contribute to the bosonic and fermionic proper self-energies. Let us start by considering the main contribution to the bosonic self-energy $\Sigma_{\rm B}$ due to BB interaction in absence of BF coupling. Our mixture then reduces to a weakly interacting gas of bosons at zero temperature with effective zero-range interaction BB given by the effective potential (for $\hbar = 1$)

$$U_{\rm BB}(\mathbf{r}-\mathbf{r}') = v_0^{\rm BB}\delta(\mathbf{r}-\mathbf{r}') = \frac{4\pi a_{\rm BB}}{m_{\rm B}}\delta(\mathbf{r}-\mathbf{r}') \tag{3.28}$$

provided $a_{\rm BB} \ll n_{\rm B}^{-1/3}$. The grand canonical Hamiltonian which describes this interacting BB mixture is given by the first line of Eq. (3.8) for s = B and by the last line of the same equation. The boson field operator $\psi_{\rm B}(\mathbf{r})$ can be separated into two parts as $\psi_{\rm B}(\mathbf{r}) = \hat{b}_{k=0}/\sqrt{V} + \tilde{\psi}_{\rm B}(\mathbf{r})$, where $\hat{b}_{k=0}$ is the Bose annihilation operator for the single-particle in the zero momentum state and $\tilde{\psi}_{\rm B}(\mathbf{r})$ is the field operator associated to non-condensed bosons. An analogous separation can be performed for the bosonic operator field $\psi_{\rm B}^\dagger(\mathbf{r})$. When the number of bosons in the zero-momentum state N_0 is a finite fraction of the total number of bosons in the system $N_{\rm B}$, the operators $\hat{b}_{k=0}$ and $\hat{b}_{k=0}^\dagger$ can be replaced by $\sqrt{N_0}$. This procedure is known as the Bogoliubov prescription. One expects that in a weakly interacting BB mixture at $T = 0$ most of the bosons remain in the zero momentum state (BEC), since only few of them are driven out of the condensate by the interactions. The fraction of non-condensate bosons with respect to the total

number of bosons is usually called "depletion". If the depletion is small, terms in the interaction Hamiltonian involving more than two non-condensed boson fields are negligible. This is the basic assumption that leads to the so-called Bogoliubov approximation [31]. In the lowest order of approximation, the normal bosonic self-energy is given by $\Sigma_{11} = 8\pi a_{\mathrm{BB}} n_0/m_{\mathrm{B}}$, while the anomalous bosonic self-energy is given by $\Sigma_{12} = 4\pi a_{\mathrm{BB}} n_0/m_{\mathrm{B}}$, provided the bosonic gas parameter $\eta = n_{\mathrm{B}} a_{\mathrm{BB}}^3 \ll 1$.

By turning on the BF coupling, the total bosonic self-energy will be given by the sum of the normal bosonic self-energy in Bogoliubov approximation and a proper normal self-energy Σ_{BF} given by BF coupling with T-diagrams presented in the previous section. If we sum all possible (proper) Feynman's diagrams that connect an incoming and outgoing bosonic line with BF interaction given only by ladder diagrams, the proper normal bosonic self-energy due to BF interaction takes the form of the diagram in Fig. 3.3.

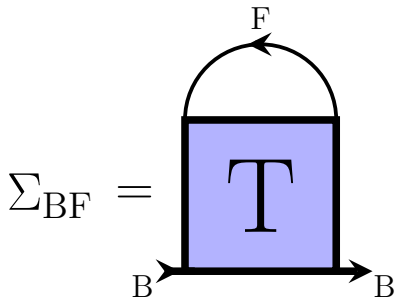

Figure 3.3: Normal bosonic self-energy due to BF interaction by ladder diagrams. The line with an arrow indicates a bare fermionic Green's function G_{F}^0, while the T-matrix block is given by the diagram in Fig. 3.2.

Using Feynman's rules in momentum space, $\Sigma_{\mathrm{BF}}(\mathbf{k}, \omega)$ can be written as

$$\Sigma_{\mathrm{BF}}(\mathbf{k}, \omega) = \int \frac{d\mathbf{P}}{(2\pi)^3} \int \frac{d\Omega}{2\pi} \mathrm{T}(\mathbf{P}, \Omega) G_{\mathrm{F}}^0(\mathbf{P} - \mathbf{k}, \Omega - \omega). \tag{3.29}$$

The complete normal bosonic self-energy is then

$$\Sigma_{\mathrm{B}}(\mathbf{k}, \omega) = \frac{8\pi a_{\mathrm{BB}} n_0}{m_{\mathrm{B}}} + \int \frac{d\mathbf{P}}{(2\pi)^3} \int \frac{d\Omega}{2\pi} \mathrm{T}(\mathbf{P}, \Omega) G_{\mathrm{F}}^0(\mathbf{P} - \mathbf{k}, \Omega - \omega). \tag{3.30}$$

The fermionic self-energy is obtained only from to the coupling with bosons. The T-matrix can be closed in the diagram either with a boson propagator or with two condensate lines. However, in this last case, we have to substitute the T-matrix given in Eq. (3.25) with the Γ-matrix given in Eq. (3.18) in order to avoid improper

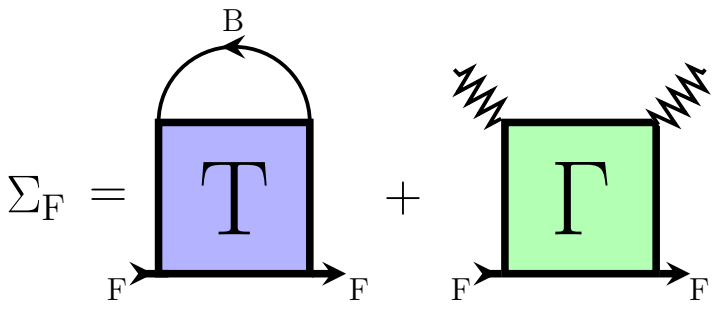

Figure 3.4: Fermionic T-matrix self-energy diagrams resulting from BF interaction. The bosonic side of the T-matrix can be closed either with a free bosonic propagator (first term) or with two condensate lines, each of them bringing a factor $\sqrt{n_0}$ (second term). Notice that in the second term the T-matrix block given in Fig. 3.2 has been replaced by the Γ-matrix in Fig. 3.1 in order to obtain a proper self-energy diagram.

self-energy diagrams. The diagram that describes the full fermionic self-energy $\Sigma_{\rm F}$ is shown in Fig. 3.4. Using Feynman's rules in momentum space, $\Sigma_{\rm F}(\mathbf{k},\omega)$ is then given by

$$\Sigma_{\rm F}(\mathbf{k},\omega) = n_0\Gamma(\mathbf{k},\omega) - \int \frac{d\mathbf{P}}{(2\pi)^3}\int \frac{d\Omega}{2\pi}\mathrm{T}(\mathbf{P},\Omega)G^0_{\rm B}(\mathbf{P}-\mathbf{k},\Omega-\omega). \tag{3.31}$$

The full (dressed) bosonic and fermionic Green's functions can be found by applying the Dyson's equation with the bosonic and fermionic self-energies just presented:

$$G_{\rm B}(\mathbf{k},\omega) = \frac{i\omega + \xi^{\rm B}_{\mathbf{k}} + \Sigma_{\rm B}(-\mathbf{k},-\omega)}{\left[i\omega + \xi^{\rm B}_{\mathbf{k}} + \Sigma_{\rm B}(-\mathbf{k},-\omega)\right]\left[i\omega - \xi^{\rm B}_{\mathbf{k}} + \Sigma_{\rm B}(\mathbf{k},\omega)\right] + \Sigma^2_{12}} \tag{3.32}$$

$$G_{\rm F}(\mathbf{k},\omega) = \frac{1}{G^0_{\rm F}(\mathbf{k},\omega)^{-1} - \Sigma_{\rm F}(\mathbf{k},\omega)}. \tag{3.33}$$

Note that in Eq. (3.32) we have obtained $G_{\rm B}(\mathbf{k},\omega)$ by solving the matrix Dyson's equation for bosons in the condensed phase (see e.g. [31]). It is important to remark that both Eqs. (3.32) and (3.32) have been calculated by setting $\mu_{\rm B} = 0$ whenever $\mu_{\rm B} > 0$ inside $\Sigma_{\rm B}$ and $\Sigma_{\rm F}$, while $\mu_{\rm B}$ can take positive values in the $\xi^{\rm B}_{\mathbf{k}}$ expression. The momentum distribution functions come from the integration over

frequencies of Eqs. (3.32) and (3.33)

$$n_{\mathrm{B}}(\mathbf{k}) = -\int \frac{d\omega}{2\pi} G_{\mathrm{B}}(\mathbf{k},\omega) e^{i\omega 0^+} \tag{3.34}$$

$$n_{\mathrm{F}}(\mathbf{k}) = \int \frac{d\omega}{2\pi} G_{\mathrm{F}}(\mathbf{k},\omega) e^{i\omega 0^+} \tag{3.35}$$

where the convergence factor $e^{i\omega 0^+}$ comes from the equal-time limit of the Green's function written in coordinate space. The number densities for bosons and fermions are obtained by momenta integration of Eqs. (3.34) and (3.35):

$$n_{\mathrm{B}} = n_0 + n'_{\mathrm{B}} = n_0 + \int \frac{d\mathbf{k}}{(2\pi)^3} n_{\mathrm{B}}(\mathbf{k}) \tag{3.36}$$

$$n_{\mathrm{F}} = \int \frac{d\mathbf{k}}{(2\pi)^3} n_{\mathrm{F}}(\mathbf{k}) \tag{3.37}$$

where with the prime symbol we indicate the number density for bosons outside the condensate. Eqs. (3.36) and (3.37), together with the equation for μ_{B} in the condensed phase given by the Hugenholtz-Pines theorem [53], i.e.

$$\mu_{\mathrm{B}} = \Sigma_{\mathrm{B}}(\mathbf{0}, 0) - \Sigma_{12} \ , \tag{3.38}$$

form a system of three non-linear integral equations, where the unknowns are μ_{B}, μ_{F} and n_0. For different values of scattering lengths a_{BF}, a_{BB}, and for various concentrations $x = n_{\mathrm{B}}/n_{\mathrm{F}}$, this integral system can be solved numerically providing us a complete description of our BF mixture at zero temperature from the Bose-polaron limit to the Fermi-polaron limit. To solve this 3×3 system of equations I have implemented a Fortran 90 numerical calculation program. This program uses both numerical integration methods and analytical properties resulting from the extension of frequencies to the whole complex plane.

Chapter 4

Analytical properties and numerical methods

In this chapter I will present a strategy for the solution of the system of equation obtained at the end of the previous chapter. This strategy consists in a combination of analytical and numerical integrations. In the first section of this chapter, I will briefly deal with the analytical properties of T-matrix and propagators. In the rest of the chapter, I will show the setting for the numerical solutions with the inclusion of useful analytical results which make numerical calculations more precise and efficient.

4.1 Analytical properties

It is now useful to investigate greater the form and properties of the T-matrix both in the normal and condensed phase, paying particular attention to its Fermi jumps in momentum space. In order to find the position of these jumps, we define the retarded T-matrix T^{R} by an analytic continuation of $\mathrm{T}(\mathbf{P}, z = i\Omega)$ to $\mathrm{T}(\mathbf{P}, z = \tilde{\Omega} + i\epsilon) \equiv \mathrm{T}^{\mathrm{R}}(\mathbf{P}, \tilde{\Omega})$, where $\tilde{\Omega}$ is a real frequency. Poles in frequency space are given by the condition

$$\mathrm{Re}\,\mathrm{T}^{\mathrm{R}}(\mathbf{P}, \tilde{\Omega}(P))^{-1} = 0 \tag{4.1}$$

when

$$\mathrm{Im}\,\mathrm{T}^{\mathrm{R}}(\mathbf{P}, \tilde{\Omega}(P))^{-1} = 0, \tag{4.2}$$

where $\tilde{\Omega}(P)$ is the dispersion relation. The condition $\tilde{\Omega}(P^\star) = 0$ gives the position of the Fermi jump at $P = P^\star$ in momentum space. Since the zero frequency is at the origin of the complex plane, the determination of momentum $P^\star$ does not require the analytic continuation, and the position of the jump can be simply found by imposing $\mathrm{Re}\,\mathrm{T}(P^\star, 0)^{-1} = 0$.

Starting with the T-matrix in the normal phase $\Gamma(\mathbf{P}, \Omega)$ given by Eq. (3.18), one can find a single jump at position P^0_Γ only for sufficiently large values of the BF attraction. On the other hand, in the condensed phase, the T-matrix T presents always a jump at momentum $P^0_{\mathrm{T}1}$. A second jump, which position is denoted as $P^0_{\mathrm{T}2}$, can appear at strong BF coupling and it is linked to the scattering between unpaired fermion and molecular binding state. Also the dressed fermionic Green's function $G_{\mathrm{F}}(\mathbf{k}, \Omega)$ given by Eq. (3.33) can present two jumps in momentum space. The position of these jumps, denoted as $k_{\mathrm{F}1}$ and $k_{\mathrm{F}2}$, can be found by imposing $\mathrm{Re}\,G_{\mathrm{F}}(\mathbf{k}, 0)^{-1} = 0$. These jumps are separated by the divergence of $\mathrm{Re}\,G_{\mathrm{F}}(\mathbf{k}, 0)^{-1}$ at momentum P^0_Γ. $k_{\mathrm{F}1} > P^0_\Gamma$ exists across the entire resonance, while the second jump at $k_{\mathrm{F}2} < P^0_\Gamma$ appears only for sufficiently strong BF coupling.

4.2 The program

To find the numerical solution of the 3×3 system of Eqs. (3.36 - 3.38) I have implemented a combination of a 2×2 SR1 (Symmetric rank 1) method with a bisection method. The SR1 is a quasi-Newton method that updates the value of the Jacobian matrix using derivatives calculated in two points. Starting with trial values for fermionic chemical potential $\mu^{(0)}_{\mathrm{F}}$ and condensate density $n^{(0)}_0$, an initial value for the bosonic chemical potential $\mu^{(0)}_{\mathrm{B}}$ can be found by solving Eq. (3.38) with the bisection method. This last value of $\mu^{(0)}_{\mathrm{B}}$ together with the trial $\mu^{(0)}_{\mathrm{F}}$ and $n^{(0)}_0$ are inserted in the r.h.s of Eqs. (3.36) and (3.37) to determine the trial initial densities $n^{(0)}_{\mathrm{B}}$ and $n^{(0)}_{\mathrm{F}}$. In the first cycle, the 2×2 Jacobian matrix $H^{(0)}$ is calculated numerically by slightly changing one at a time the starting values of $\mu^{(0)}_{\mathrm{F}}$ and $n^{(0)}_0$, and by computing n_{B} and n_{F} using Eqs. (3.36) and (3.37). The new values for the fermionic chemical potential $\mu^{(1)}_{\mathrm{F}}$ and condensate density $n^{(1)}_0$ are obtained by multiplying the inverse of $H^{(0)}$ by $n^{(0)}_{\mathrm{B}}$ and $n^{(0)}_{\mathrm{F}}$. With these new values $\mu^{(1)}_{\mathrm{F}}$ and $n^{(1)}_0$ one can find $\mu^{(1)}_{\mathrm{B}}$ from Eq. (3.38), and successively $n^{(1)}_{\mathrm{B}}$ and $n^{(1)}_{\mathrm{F}}$ can be computed by using Eqs. (3.36 - 3.38). At this point we have obtained two values of the densities n_{B}, n_{F} corresponding to two values for μ_{F} and n_0. The difference between the two values of the densities, together with the difference

between the two values of $\mu_{\rm F}$ and n_0, determines the updating matrix for the Jacobian $H^{(1)}$. Once we obtain this new Jacobian matrix, the method restarts using $\mu_{\rm F}^{(1)}$ and $n_0^{(1)}$ as starting values and $H^{(1)}$ to update these two values, i.e. to find $\mu_{\rm F}^{(2)}$ and $n_0^{(2)}$. The process stops at the $k-$cycle, when Eqs. (3.36) and (3.37) are satisfied for values $\mu_{\rm B}^{(k)}$, $\mu_{\rm F}^{(k)}$ and $n_0^{(k)}$ with some fixed precision.

In order to solve Eqs. (3.36 - 3.38), integrals were calculated with the *Gauleg* subroutine which implements the Gauss-Legendre quadrature method for definite integrals. The integration is broken into intervals to optimize the precision by taking more points in intervals where the integrand gives more contribution to the integral or it varies rapidly. However functions with jumps are not precisely integrated with the *Gauleg* method using a small number of points. To efficiently integrate such functions one can join two intervals exactly at the position of the jump. With this trick the function becomes more regular in the two separate intervals and the integral can be performed with a smaller number of points, saving computational time. It is for this reason that the determination of the Fermi step momenta P_Γ^0, $P_{\rm T1}^0$, $P_{\rm T2}^0$ and $k_{\rm F1}$, $k_{\rm F2}$ is important.

Most of the integrals that appear on the r.h.s. of Eqs. (3.36) and (3.37) are over unbounded regions in momentum or frequency space. To evaluate numerically these integrals, I have fixed a cut-off as upper bound limit for the numerical integration and I have integrated analytically the asymptotic expression of the integrand from the cut-off to infinity. Such cut-off values are chosen big enough to not affect significantly the final result. Another sensitive issue is the convergence of the integrals. For example by looking at Eqs. (3.34) and (3.35), the convergence factor $e^{i\omega 0^+}$ is required to ensure the convergence for the ω-integration. In order to evaluate these integrals numerically one can add and subtract an auxiliary function with the same behaviour of the integrand for large values of ω. The resulting convergent integral can be computed numerically using the *Gauleg* subroutine, while the integral of the auxiliary function is determined analytically.

4.3 Numerical integrals and analytical results

In our calculations, the trace over momenta and frequencies of the T-matrix (3.25) is fundamental in the evaluation of the integrations on the r.h.s. of Eqs. (3.36) and (3.37) for high frequencies and for large momenta. I will refer to this trace

value as Δ^2_∞

$$\Delta^2_\infty = \int \frac{d\mathbf{P}}{(2\pi)^3} \int \frac{d\Omega}{2\pi} \mathrm{T}(\mathbf{P},\Omega) e^{i\Omega 0^+}, \tag{4.3}$$

where the convergence factor $e^{i\Omega 0^+}$ here is necessary since $\mathrm{T} \sim 1/\sqrt{\Omega}$ for large Ω, which would give a divergent contribution when integrated numerically over frequency. To deal with this divergent behaviour one can add and subtract $\Gamma^{\mathrm{SC}}(\mathbf{P},\Omega)$, given by Eq. (3.23), which has the same behaviour of $\mathrm{T}(\mathbf{P},\Omega)$ for large Ω. Considering for the moment only the frequency integral one has

$$\begin{aligned} \int_{-\infty}^{+\infty} \frac{d\Omega}{2\pi} \mathrm{T}(\mathbf{P},\Omega) e^{i\Omega 0^+} &= \int_{-\infty}^{+\infty} \frac{d\Omega}{2\pi} \left[\mathrm{T}(\mathbf{P},\Omega) - \Gamma^{\mathrm{SC}}(\mathbf{P},\Omega)\right] \\ &+ \int_{-\infty}^{+\infty} \frac{d\Omega}{2\pi} \Gamma^{\mathrm{SC}}(\mathbf{P},\Omega) e^{i\Omega 0^+}, \end{aligned} \tag{4.4}$$

where the convergence factor can be eliminated from the first integrand (which goes as Ω^{-2} for large frequencies [30]). The first line of Eq. (4.4) can be computed numerically, while the integral in the second line can be evaluated via a contour integration in the complex plane with the extension $i\Omega \to z$

$$\Gamma^{\mathrm{SC}}(\mathbf{P},z)^{-1} = \frac{m_r}{2\pi a_{\mathrm{BF}}} - \frac{m_r^{3/2}}{\sqrt{2}\,\pi} \sqrt{\frac{P^2}{2M} - 2\mu - z}\,. \tag{4.5}$$

$\Gamma^{\mathrm{SC}}(\mathbf{P},z)$ in Eq. (4.5) has a pole at $\mathrm{Re}z = \xi^{\mathrm{CF}}_{\mathbf{P}}(z) = P^2/2M - 2\mu + \epsilon_0$, where $\epsilon_0 = (2m_r a^2_{\mathrm{BF}})^{-1}$, and a branch cut for $\mathrm{Re}z = z_c > P^2/2M - \mu$. The second integral in Eq. (4.4) then yields:

$$\begin{aligned} \int_{-\infty}^{+\infty} \frac{d\Omega}{2\pi} \Gamma^{\mathrm{SC}}(\mathbf{P},\Omega) e^{i\Omega 0^+} &= \frac{2\pi}{m_r^2 a_{\mathrm{BF}}} \Theta(-\xi^{\mathrm{CF}}_{\mathrm{P}}) \Theta(a_{\mathrm{BF}}) \\ &- \Theta(-z_c) \left[\frac{-2\sqrt{2}}{m_r^{3/2}} \sqrt{-z_c} + \frac{2}{m_r^2 a_{\mathrm{BF}}} \mathrm{atan} \sqrt{-2 m_r a^2_{\mathrm{BF}} z_c} \right]. \end{aligned} \tag{4.6}$$

On the other hand, the first integral in Eq. (4.4), introducing the cut-off Ω_c, can be written as:

$$\begin{aligned} \int_{-\infty}^{+\infty} \frac{d\Omega}{2\pi} \left[\mathrm{T}(\mathbf{P},\Omega) - \Gamma^{\mathrm{SC}}(\mathbf{P},\Omega)\right] &= 2\mathrm{Re} \int_0^{\Omega_c} \frac{d\Omega}{2\pi} \left[\mathrm{T}(\mathbf{P},\Omega) - \Gamma^{\mathrm{SC}}(\mathbf{P},\Omega)\right] \\ &+ 2\mathrm{Re} \int_{\Omega_c}^{+\infty} \frac{d\Omega}{2\pi} \left[\mathrm{T}(\mathbf{P},\Omega) - \Gamma^{\mathrm{SC}}(\mathbf{P},\Omega)\right], \end{aligned} \tag{4.7}$$

where the general property of the T-matrix $\mathrm{T}(\mathbf{P},\Omega) = \mathrm{T}(\mathbf{P},-\Omega)^*$ has been used for both the T- and the Γ^{SC}-matrix. The first integral on the r.h.s. of Eq. (4.7) can be computed numerically, while the second integral can be evaluated analytically using the asymptotic behaviour of the integrand. In particular, for large frequencies one has from Eq. (3.19)

$$\int \frac{d\mathbf{q}}{(2\pi)^3} \frac{\Theta(-\xi^{\mathrm{F}}_{\mathbf{P}-\mathbf{q}})}{\xi^{\mathrm{F}}_{\mathbf{P}-\mathbf{q}} + \xi^{\mathrm{B}}_{\mathbf{q}} - i\Omega} \simeq -\frac{n_{\mu_{\mathrm{F}}}}{i\Omega} \tag{4.8}$$

where $n_{\mu_{\mathrm{F}}} = \dfrac{k^3_{\mu_{\mathrm{F}}}}{6\pi^2}$. One thus has for large Ω

$$\mathrm{T}(\mathbf{P},\Omega) - \Gamma^{\mathrm{SC}}(\mathbf{P},\Omega) \simeq \frac{2\pi^2}{m_r^3} \frac{n_0 - n_{\mu_{\mathrm{F}}}}{\Omega^2}, \tag{4.9}$$

and consequently

$$2\mathrm{Re}\int_{\Omega_c}^{+\infty} \frac{d\Omega}{2\pi} \left[\mathrm{T}(\mathbf{P},\Omega) - \Gamma^{\mathrm{SC}}(\mathbf{P},\Omega)\right] = \frac{2\pi}{m_r^3} \frac{n_0 - n_{\mu_{\mathrm{F}}}}{\Omega_c} + O(\Omega_c^{-2}) \tag{4.10}$$

where higher order terms in $1/\Omega_c$ have been neglected. We now sum all the contributions coming from the integral over frequency and perform the numerical integration over momenta. The angular part gives a contribution of 4π, while the integration over $P = |\mathbf{P}|$ needs to be evaluated numerically with Gauss–Legendre quadrature. In particular, the integrand can have a jump for some coupling values at momentum P^0_{T2}, and vanishes for momenta larger than P^0_{T1}. The momentum P^0_{T1} is always present across the entire resonance, while P^0_{T2} is present only for coupling higher then a certain value, and it is associated to the molecular binding of a boson and a fermion.

Let us now move to the evaluation of the integrals on r.h.s. of Eqs. (3.30) and (3.31) for the self-energies. The integrals over frequencies can be evaluated numerically using Gauss–Legendre quadrature in the range $[-\Omega_c, \Omega_c]$, while integrals in the intervals $[-\infty, -\Omega_c]$ and $[\Omega_c, \infty]$ have to be evaluated analytically using the asymptotic expressions of the integrands. In particular, one can find that for high frequencies Ω the T-matrix goes like

$$\mathrm{T}(\mathbf{P},\Omega) = -\frac{\sqrt{2}\pi}{m_r^{3/2}\sqrt{-i\Omega}} + \frac{\pi}{a_{\mathrm{BF}} m_r^2} \frac{1}{i\Omega} + \sqrt{2}\pi \frac{m_r \left(\frac{q^2}{M} - 4\mu\right) - \frac{2}{a^2_{\mathrm{BF}}}}{m_r^{5/2}(-i\Omega)^{3/2}} + O(\Omega^{-2}). \tag{4.11}$$

Moreover one can find that

$$\int_0^\pi d\theta G_{\rm B}^0(\mathbf{P}-\mathbf{k},\omega-\Omega) = \frac{2}{i\Omega} + \frac{\dfrac{P^2+k^2}{2m_{\rm B}} - \mu_{\rm B}}{(-i\Omega)^2} + O(\Omega^{-3}) \tag{4.12}$$

$$\int_0^\pi d\theta G_{\rm F}^0(\mathbf{P}-\mathbf{k},\omega-\Omega) = \frac{2}{i\Omega} + \frac{\dfrac{P^2+k^2}{2m_{\rm F}} - \mu_{\rm F}}{(-i\Omega)^2} + O(\Omega^{-3}) \tag{4.13}$$

where θ is the angle between momenta $\mathbf{P}$ and $\mathbf{k}$. The product between the r.h.s. of Eq. (4.11) with the r.h.s. of Eq. (4.12) or of Eq. (4.13) gives the two asymptotic behaviours at large Ω for the integrands in Eqs. (3.30) and (3.31), respectively, which can then be integrated analytically in the intervals $[-\infty,-\Omega_c]$ and $[\Omega_c,\infty]$, neglecting terms smaller then $\Omega_c^{-5/2}$. The remaining integrals over frequencies in Eqs. (3.30) and (3.31) have been performed numerically with Gauss–Legendre quadrature. Finally the sums of all contributions obtained from integration over frequency have been integrated numerically over $P=|\mathbf{P}|$ after a trivial integration over the azimuth angle. The integrand for the bosonic self-energy in Eq. (3.30) has two jumps at $P_{\rm T1}^0$ and $P_{\rm T2}^0$, and two jumps when $\mu_{\rm F}>0$ at $|k_{\mu_{\rm F}}-k|$ and $k_{\mu_{\rm F}}+k$. We ordered the values of these 4 jumps in ascending order and broke the Gauss-Legendre integration into different intervals in order to have the jumps at the extremes of the intervals.

As mentioned above, in order to obtain the momentum distributions $n_{\rm B}(\mathbf{k})$ and $n_{\rm F}(\mathbf{k})$, the bosonic and fermionic dressed Green's functions given by Eqs. (3.32) and (3.33) have to be integrated over frequencies using the convergence factor $e^{i\omega 0^+}$, as reported in Eqs. (3.34) and (3.35). These integrations can be performed numerically by adding and subtracting functions with the same asymptotic behaviours as the dressed Green's functions, but which can be integrated analytically in the whole frequency range $[-\infty,\infty]$. Starting form the bosonic dressed Green's function, the r.h.s. of Eq. (3.34) can be rewritten as

$$n_{\rm B}(\mathbf{k}) = -\int_{-\infty}^{+\infty}\frac{d\omega}{2\pi}\left[G_{\rm B}(\mathbf{k},\omega) - G_{\rm B}^{0\,\prime}(\mathbf{k},\omega)\right] - \int_{-\infty}^{+\infty}\frac{d\omega}{2\pi}G_{\rm B}^{0\,\prime}(\mathbf{k},\omega)e^{i\omega 0^+} \tag{4.14}$$

where $G_{\rm B}^{0\,\prime}(\mathbf{k},\omega)$ is a bare Bogoliubov Green's function

$$G_{\rm B}^{0\,\prime}(\mathbf{k},\omega) = \frac{i\omega + \xi_{\mathbf{k}}^{\rm B} + 2\Sigma_{12}}{\left[i\omega + \xi_{\mathbf{k}}^{\rm B} + 2\Sigma_{12}\right]\left[i\omega - \xi_{\mathbf{k}}^{\rm B} - 2\Sigma_{12}\right] + \Sigma_{12}^2} \tag{4.15}$$

which is obtained simply by neglecting the second term in Eq. (3.30), i.e. the interaction between bosons and fermions. The integral for the first term on the r.h.s. of Eq. (4.14) now converges and the factor $e^{i\omega 0^+}$ can be dropped. The same procedure can be repeated for fermions using the bare fermionic Green's function $G^0_{\rm F}(\mathbf{k},\omega)$ instead of a bare Bogoliubov Green's function. Then Eq. (3.35) can be rewritten as

$$n_{\rm F}(\mathbf{k}) = \int_{-\infty}^{+\infty} \frac{d\omega}{2\pi} \left[G_{\rm F}(\mathbf{k},\omega) - G^0_{\rm F}(\mathbf{k},\omega) \right] + \int_{-\infty}^{+\infty} \frac{d\omega}{2\pi} G^0_{\rm F}(\mathbf{k},\omega) e^{i\omega 0^+}. \tag{4.16}$$

Using the property $G(\mathbf{k},\omega) = G(\mathbf{k},-\omega)^*$, the first terms on the r.h.s. of Eqs. (4.14) and (4.16) are equal to two times their real parts, considering the integration only over positive frequencies. These two integrals can be performed numerically in the frequency range $[0,\Omega_c]$, neglecting contributions coming from higher frequencies. Moreover in the range $[100E_{\rm F},\Omega_c]$ we have used the asymptotic expressions for $\Sigma_{\rm B}(\mathbf{k},\omega/E_{\rm F}\to\infty)$ and $\Sigma_{\rm F}(\mathbf{k},\omega/E_{\rm F}\to\infty)$, obtained directly from their original expressions in Eqs. (3.30) and (3.31):

$$\Sigma_{\rm B}(\mathbf{k},\omega/E_{\rm F}\to\infty) = 2\Sigma_{12} + n_{\mu_{\rm F}} {\rm T}(\mathbf{k},\omega) - \Delta^2_\infty G^0_{\rm F}(\mathbf{k},\omega) \tag{4.17}$$

$$\Sigma_{\rm F}(\mathbf{k},\omega/E_{\rm F}\to\infty) = n_0 \Gamma(\mathbf{k},\omega) + \Delta^2_\infty G^0_{\rm B}(\mathbf{k},\omega), \tag{4.18}$$

By using these two expressions (which were reported in Ref. [30]) in the calculation of $G_{\rm B}$ and $G_{\rm F}$, one commits a negligible error for frequencies ω higher then $100E_{\rm F}$. Finally the integration for the second terms on the r.h.s. of Eqs. (4.14) and (4.16) can be evaluated analytically, yielding:

$$\int_{-\infty}^{+\infty} \frac{d\omega}{2\pi} G^{0\,\prime}_{\rm B}(\mathbf{k},\omega) e^{i\omega 0^+} = \frac{1}{2}\left[\frac{\xi^{\rm B}_{\mathbf{k}} + 2\Sigma_{12}}{\sqrt{(\xi^{\rm B}_{\mathbf{k}})^2 + 3\Sigma^2_{12} + 4\Sigma_{12}\xi^{\rm B}_{\mathbf{k}}}} - 1 \right] \tag{4.19}$$

$$\int_{-\infty}^{+\infty} \frac{d\omega}{2\pi} G^0_{\rm F}(\mathbf{k},\omega) e^{i\omega 0^+} = \Theta(-\xi^{\rm F}_{\mathbf{k}}). \tag{4.20}$$

Putting all these contributions together, one gets an expression for $n_{\rm B}(\mathbf{k})$ and $n_{\rm F}(\mathbf{k})$ that can be integrated numerically over momentum $\mathbf{k}$. The integration over the angular part is trivial and gives a factor of 4π. The integration over $k = |\mathbf{k}|$ is performed numerically, up to a value $k_c > k_{\rm F}$. For momenta $k > k_c$,

an analytical integration of the asymptotic expressions of Eqs. (3.34) and (3.35) has been carried out. In particular, using Eqs. (3.32), (3.33) and (4.15), one finds that

$$n_{\mathrm{B}}(k \gg k_{\mathrm{F}}) = \frac{\Delta_{\infty}^2}{4\left(\frac{k^2}{4m_r} - \mu\right)^2} + \frac{\Sigma_{12}^2}{4\left(\frac{k^2}{2m_{\mathrm{B}}} - \mu_{\mathrm{B}}\right)^2} \tag{4.21}$$

$$n_{\mathrm{F}}(k \gg k_{\mathrm{F}}) = \frac{\Delta_{\infty}^2}{4\left(\frac{k^2}{4m_r} - \mu\right)^2}. \tag{4.22}$$

Taking $k_c = 4k_{\mathrm{F}}$ will imply a negligible error in the final result. The bosonic momentum distribution function has a divergence at low momentum, which is compensated by the k^2 term resulting from the transformation of the integral to spherical coordinates, and it has no jumps. Therefore a single interval has been used in Gauss-Legendre quadrature method. The fermionic momentum distribution function has instead two jumps at momenta k_{F1} and k_{F2}, and 3 intervals joined at these two points are necessary to compute accurately the integral over k.

Chapter 5

Numerical results

In this chapter I will present numerical results obtained by the solution of Eqs. (3.36 - 3.38). *Condensate depletion and the chemical potential values will be presented for various density ratios* $x = n_{\rm B}/n_{\rm F}$. *These results have been obtained across the entire BF resonance and they have been compared to the corresponding asymptotic behaviours obtained from perturbation theory. In the first section I will show results for a BF mixture with a majority of fermions, paying particular attention to the relevant case* $x = 0.9$, *realized with a trapped* ^{23}Na - ^{40}K *mixture* [29]. *In the second section I will deal in detail with a mixture with a majority of bosons* ($x > 1$), *showing some unexpected results in the limit* $x \to 1^+$. *In the remaining sections the mechanical stability of a BF mixture will be analysed, with a comparison between the T-matrix approximation results and previous studies on stability. This stability condition is fundamental in the investigation of trapped BF mixtures.*

5.1 Numerical results for $x < 1$

In this section, I will show the numerical results for $\mu_{\rm B}$, $\mu_{\rm F}$ and n_0 obtained from the system of Eqs. (3.36 - 3.38) for a mixture with a majority of fermions. In particular, I will consider a mass ratio $m_{\rm B}/m_{\rm F} = 0.575$, corresponding to the experimental case of a ^{23}Na - ^{40}K mixture, and two different values of gas parameters $\eta = n_{\rm B} a_{\rm BB}^3 = 0$, and 3×10^{-3}. Chemical potentials will be reported in units of the Fermi energy $E_{\rm F} = k_{\rm F}^2/2m_{\rm F}$, with $k_{\rm F} = (6\pi^2 n_{\rm F})^{1/3}$, while the condensate density will be showed in units of the total boson density $n_{\rm B}$ for various values of $x = n_{\rm B}/n_{\rm F}$. Chemical potentials and condensate density are given as functions of the dimensionless BF coupling $g_{\rm BF} = (k_{\rm F} a_{\rm BF})^{-1}$ from a weak- to a strong-coupling regime. Repulsions between bosons are fixed by the gas parameter

η and they are given in terms of the dimensionless quantity $\zeta = k_{\rm F} a_{\rm BB}$. I have studied mixtures with 4 different values of $x < 1$: $x = 0.01$, 0.175, 0.49, and 0.9.

5.1.1 Chemical potentials

In the limit in which we can neglect interaction between bosons and fermions, $\mu_{\rm B}$ is given by the mean-field Bogoliubov result $\mu_B = 4\pi a_{\rm BB} n_0/m_{\rm B}$, while $\mu_{\rm F} = E_{\rm F} = k_{\rm F}^2/2m_{\rm F}$. For a weak BF coupling one expects the bosonic and fermionic chemical potentials μ_B and μ_F to tend to these asymptotic values obtained by perturbation theory in Ref. [54]:

$$\mu_{\rm B} = \frac{4\pi a_{\rm BB} n_0}{m_{\rm B}} + \frac{2\pi a_{\rm BF} n_{\rm F}}{m_r}\left[1 + \frac{k_{\rm F} a_{\rm BF}}{\pi} f(\delta)\right] \tag{5.1}$$

$$\mu_{\rm F} = E_{\rm F} + \frac{2\pi a_{\rm BF} n_0}{m_r}\left[1 + \frac{4 k_{\rm F} a_{\rm BF}}{3\pi} f(\delta)\right] \tag{5.2}$$

where $f(\delta)$ is given by

$$f(\delta) = 1 - \frac{3+\delta}{4\delta} + \frac{3(\delta+1)^2(\delta-1)}{8\delta^2}\ln\left(\frac{1+\delta}{1-\delta}\right) \tag{5.3}$$

with $\delta = m_{\rm B}/m_{\rm F}$. On the other hand, in the opposite strong-coupling limit, one expects the condensate fraction to vanish due to BF correlation, leading the system to a normal phase. In this regime, μ_B and $\mu_{\rm F}$ should be given by the following strong-coupling expansions (see Ref. [24]):

$$\mu_{\rm B} = \frac{(6\pi^2 n_{\rm B})^{2/3}}{2M} + \frac{4\pi a_{\rm BF}}{m_r}(n_{\rm F} - 2n_{\rm B}) - \frac{\left[6\pi^2(n_{\rm F} - n_{\rm B})\right]^{2/3}}{2m_{\rm F}} - \epsilon_0 \tag{5.4}$$

$$\mu_{\rm F} = \frac{\left[6\pi^2(n_{\rm F} - n_{\rm B})\right]^{2/3}}{2m_{\rm F}} + \frac{4\pi a_{\rm BF}}{m_r} n_{\rm B}. \tag{5.5}$$

The explanation of Eqs. (5.4) and (5.5) is fairly intuitive. In a system with a majority of fermions, all bosons are bounded into molecules composed by a fermion and a boson in the strong BF coupling limit. One thus have a density of molecules (dimers) $n_{\rm M} = n_{\rm B}$ and a density of unpaired fermions $n_{\rm UF} = n_{\rm F} - n_{\rm B}$. The molecules are repelled by the unpaired fermions by a mean-field interaction $2\pi a_{\rm DF} n_{\rm UF}/m_{\rm DF}$ where $m_{\rm DF} = M m_{\rm F}/(m_{\rm F} + M)$ is the reduced mass of a dimer

and one fermion, while the dimer-fermion scattering length $a_{\rm DF} = \gamma a_{\rm BF}$ (where the coefficient $\gamma = \frac{(1+m_{\rm F}/m_{\rm B})^2}{1/2+m_{\rm F}/m_{\rm B}}$ within the present approach [24]). Similarly, the unpaired fermions are repelled by the molecules by a term $2\pi a_{\rm DF} n_{\rm M}/m_{\rm DF}$. Both molecules and unpaired fermions are fermions, with Fermi energies $(6\pi^2 n_{\rm M})^{2/3}/2M$ and $(6\pi^2 n_{\rm UF})^{2/3}/2m_{\rm F}$, respectively. The expression (5.4) for $\mu_{\rm B}$ can be rewritten as

$$\mu_{\rm B} = \frac{(6\pi^2 n_{\rm M})^{2/3}}{2M} + \frac{2\pi a_{\rm DF}}{m_{\rm DF}} n_{\rm UF} - \epsilon_0 - \left[\frac{(6\pi^2 n_{\rm UF})^{2/3}}{2m_{\rm F}} + \frac{2\pi a_{\rm DF}}{m_{\rm DF}} n_{\rm M}\right]. \qquad (5.6)$$

Now, the addition of a boson to the system will result in the formation of a new dimer, with binding energy $-\epsilon_0$, kinetic energy $(6\pi^2 n_{\rm M})^{2/3}/2M$, and mean-field repulsion $2\pi a_{\rm DF} n_{\rm UF}/m_{\rm DF}$, corresponding to the first three terms in Eq. (5.6), and the destruction of an unpaired fermion of kinetic energy $(6\pi^2 n_{\rm UF})^{2/3}/2m_{\rm F}$ and mean-field repulsion $2\pi a_{\rm DF} n_{\rm M}/m_{\rm DF}$, corresponding to the last two terms in Eq. (5.6).

If instead we add a fermion, it will be placed at the Fermi energy of unpaired fermions with kinetic energy given by the first term in Eq. (5.5) and a mean-field repulsion with molecules given by the second term in Eq. (5.5).

In Figs. 5.1 and 5.2 the bosonic chemical potentials are reported as functions of the BF dimensionless coupling $g_{\rm BF}$, for boson gas parameters $\eta = 3 \times 10^{-3}$ and $\eta = 0$, respectively. In order to compare the values of $\mu_{\rm B}$ obtained numerically in the strong-coupling limit with the expected behaviours given by Eq. (5.4), the dominant contribution due to the binding energy $-\epsilon_0$ has been subtracted to $\mu_{\rm B}$ for positive values of $g_{\rm BF}$, when $\epsilon_0 \neq 0$. Staring from a weak-coupling condition, the bosonic chemical potential decreases from the Bogoliubov mean-field value with a good agreement with Eq. (5.1), represented by a dash-dotted line in the weak-coupling region. For each value of x, $\mu_{\rm B}$ reaches a minimum near the unitarity region ($g_{\rm BF} = 0$), with its position almost independent from x. For larger values of $g_{\rm BF}$, the bosonic chemical potential starts to increase reaching a maximum value for the critical BF coupling value g_c where the condensate depletion is complete. When the condensate is completely depleted $\mu_{\rm B}$ changes abruptly its behaviour with an angular point and then follows the evolution given by Eq. (5.4), represented by a dash-dotted line in the strong-coupling region.

In Figs. 5.3 and 5.4 the fermionic chemical potentials $\mu_{\rm F}$ obtained numerically are reported for gas parameters $\eta = 3 \times 10^{-3}$ and $\eta = 0$, respectively. The fermionic chemical potential shows a non-monotonic behaviour which can be

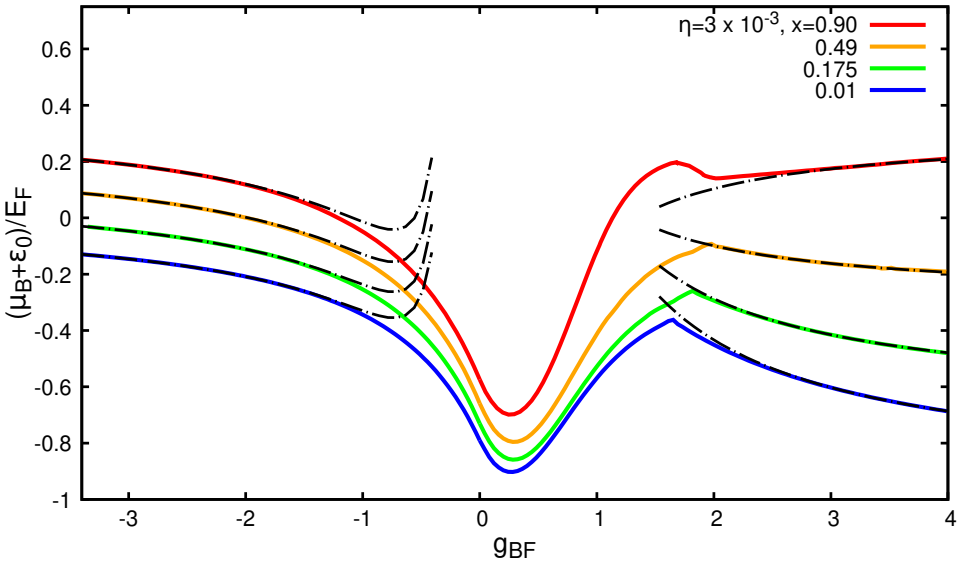

Figure 5.1: $\mu_{\rm B} + \epsilon_0$ (for $g_{\rm BF} \geq 0$) considering various values of $x < 1$ and $\eta = 3 \times 10^{-3}$. The dash-dotted lines represent the asymptotic results for $\mu_{\rm B}$ in the weak- and strong-coupling regions.

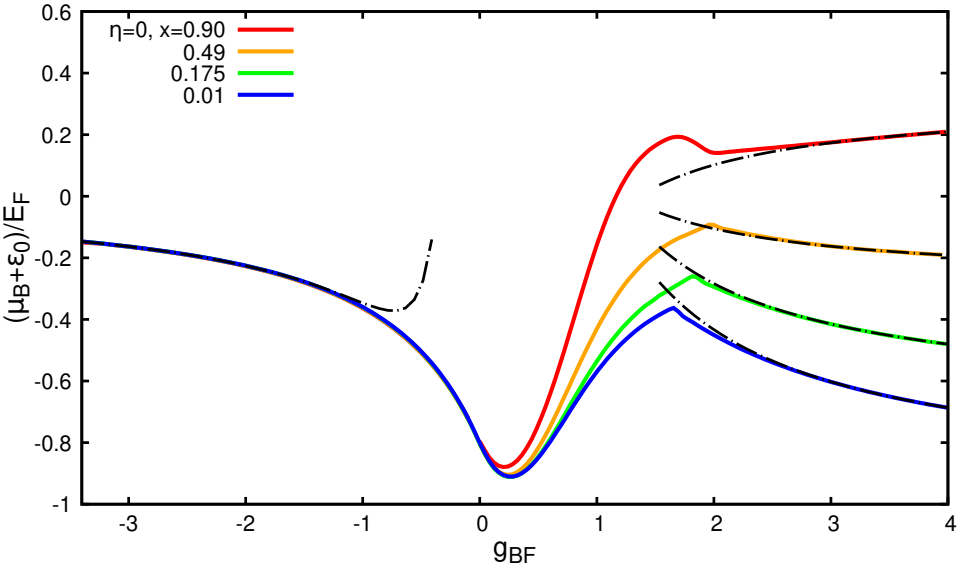

Figure 5.2: $\mu_{\rm B} + \epsilon_0$ (for $g_{\rm BF} \geq 0$) considering various values of $x < 1$ and $\eta = 0$. The dash-dotted lines represent the expected results for $\mu_{\rm B}$ in weak- and strong-coupling regions.

explained as follows. The initial decrease of $\mu_{\rm F}$ for increasing $g_{\rm BF}$ in the weak-coupling region is simply due to the mean-field attractive interaction with bosons, as described by Eq. (5.2) (corresponding to the dash-dotted curves on the weak-coupling side of Fig. 5.3). The chemical potential $\mu_{\rm F}$ then continues to decrease because molecules are formed and the number of unpaired fermions decreases, with a corresponding decrease of the Fermi energy of the unpaired fermions. At

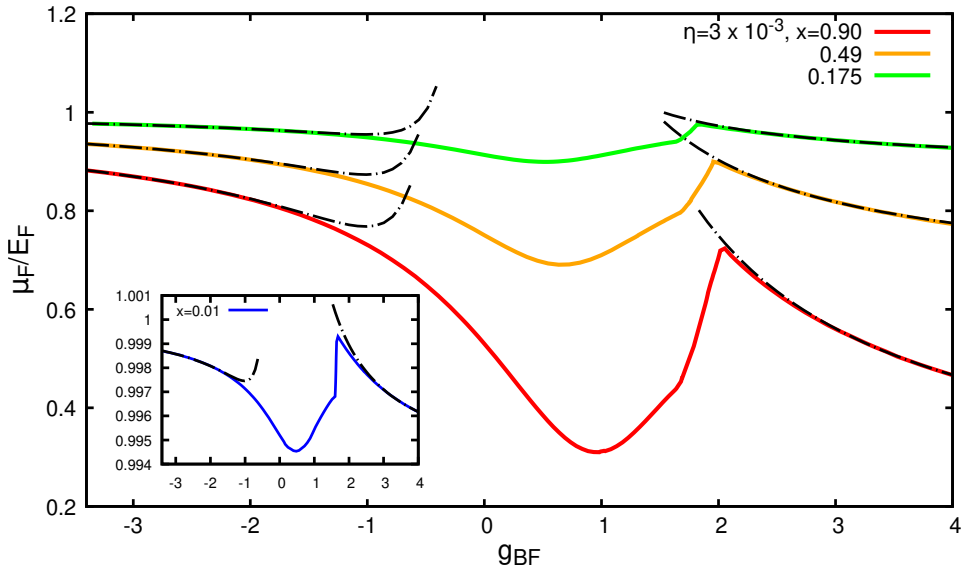

Figure 5.3: Fermionic chemical potentials vs g_{BF} for $\eta = 3\times10^{-3}$. The behaviour of μ_{F} has been reported for various values of $x < 1$. For the sake of clarity I have isolated the polaronic case $x = 0.01$ in the inset. The dash-dotted lines represent the weak- and strong-coupling behaviours given by Eqs. (5.2) and (5.5), respectively.

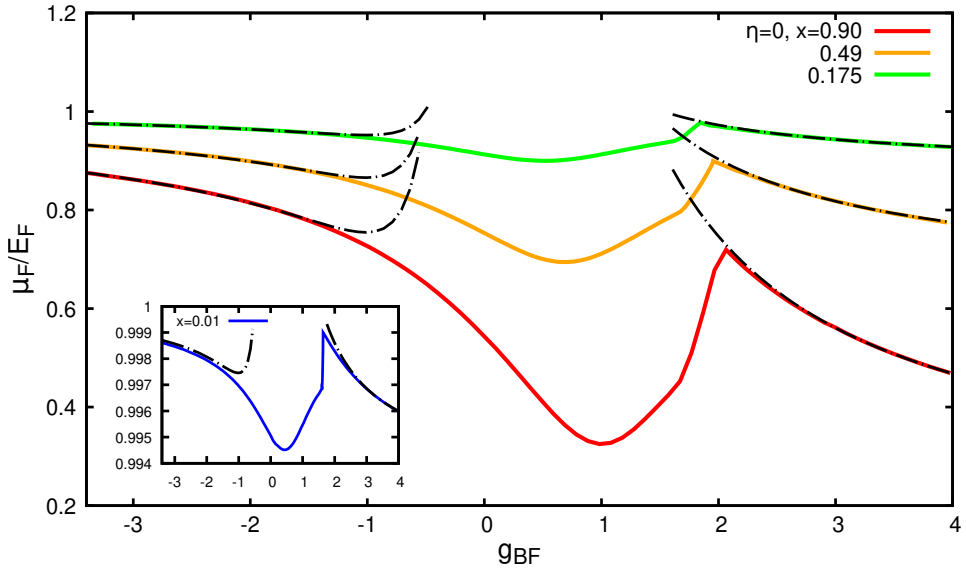

Figure 5.4: Fermionic chemical potentials vs g_{BF} for $\eta = 0$. The behaviour of μ_{F} has been reported for various values of $x < 1$. The polaronic case $x = 0.01$ is reported in the inset. The dash-dotted lines represent the weak- and strong-coupling behaviours of Eqs. (5.2) and (5.5).

the same time, however, the increasing number of molecules will exert a repulsion on the unpaired fermions (cf. second term in Eq. (5.5) with n_{M} instead of n_{B}). This effect eventually dominates and explains the rise of the curve of μ_{F} for $g_{\mathrm{BF}} \gtrsim 1$. Finally, when the condensate vanishes, the number of molecules reaches

its maximum value $n_M = n_B$ and thus the curve decreases again, following the asymptotic expression (5.5).

5.1.2 Condensate fraction

The condensate fractions n_0/n_B are reported in the following figures for various values of $x < 1$ throughout the entire BF resonance. The most important feature of the condensate fraction as a function of g_{BF} is its universality with respect to the density ratio $x = n_B/n_F$, as already found in Ref. [26]. This result is presented in Fig. 5.5 for different concentrations, including the relevant case $x = 0.9$, with a mass ratio fixed to $m_B/m_F = 0.575$. Taking different values of $x < 1$ and the

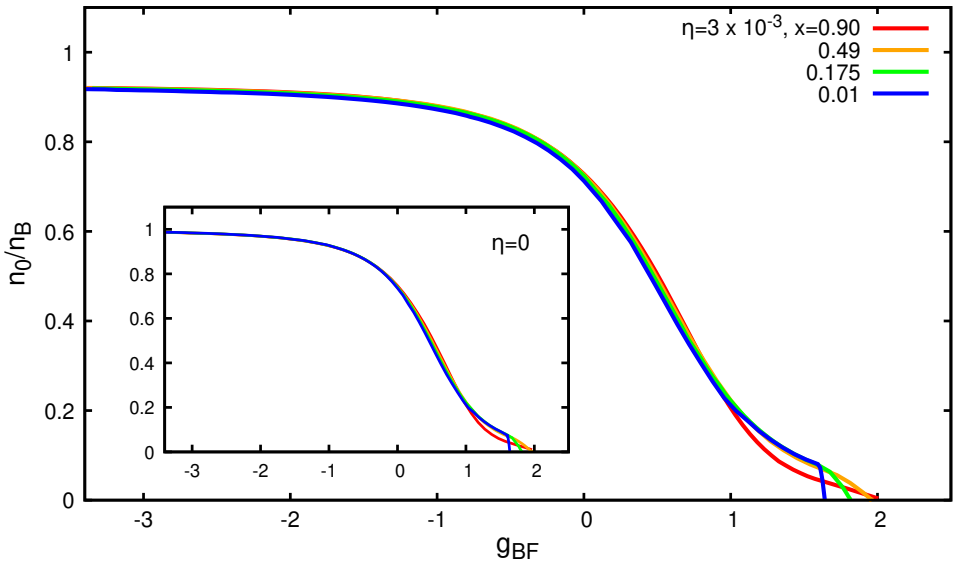

Figure 5.5: Condensate fraction n_0/n_B vs g_{BF} for $\eta = 3 \times 10^{-3}$. In the inset the condensate fraction is reported for a BF mixture with a boson gas parameter $\eta = 0$.

same value of η, the curves for the condensate fraction fall on the top of each other across almost the entire range of BF couplings, up to the strong-coupling region where the condensate fraction is completely suppressed and the system becomes an interacting gas of unpaired fermions and fermion molecules. The universality is preserved also in the Fermi-polaron regime ($x \simeq 0$) up to $g_{BF} \sim 1.5$ where the condensate fraction goes to zero faster and faster as the bosonic concentration goes to zero, with a jump in the polaron limit $x \to 0$.

If we switch-off the BF pairing, one expects to recover the Bogoliubov result for the condensate fraction [31]

$$\frac{n_0}{n_B} = 1 - \frac{8}{3}\sqrt{\frac{\eta}{\pi}} \tag{5.7}$$

where the gas parameter η is given in terms of the BB scattering length $a_{\rm BB}$ as $\eta = n_{\rm B} a_{\rm BB}^3$. This is the condensate fraction of an interacting Bose gas surrounded by a gas of non-interacting fermions. When the BF interaction is switched-on, $n_0/n_{\rm B}$ should follow the perturbative behaviour (to the second order in $g_{\rm BF}$) [55]:

$$\frac{n_0}{n_{\rm B}} = 1 - \frac{8}{3}\sqrt{\frac{\eta}{\pi}} - \frac{1}{(\pi g_{\rm BF})^2}\frac{1 + m_{\rm B}/m_{\rm F}}{1 - m_{\rm B}/m_{\rm F}} \ln\left(\frac{m_{\rm B}}{m_{\rm F}}\right). \tag{5.8}$$

In Figs. 5.6 - 5.8 I have compared the condensate fractions for a fixed value of density ratio considering two different values of the gas parameter η. The dash-dotted

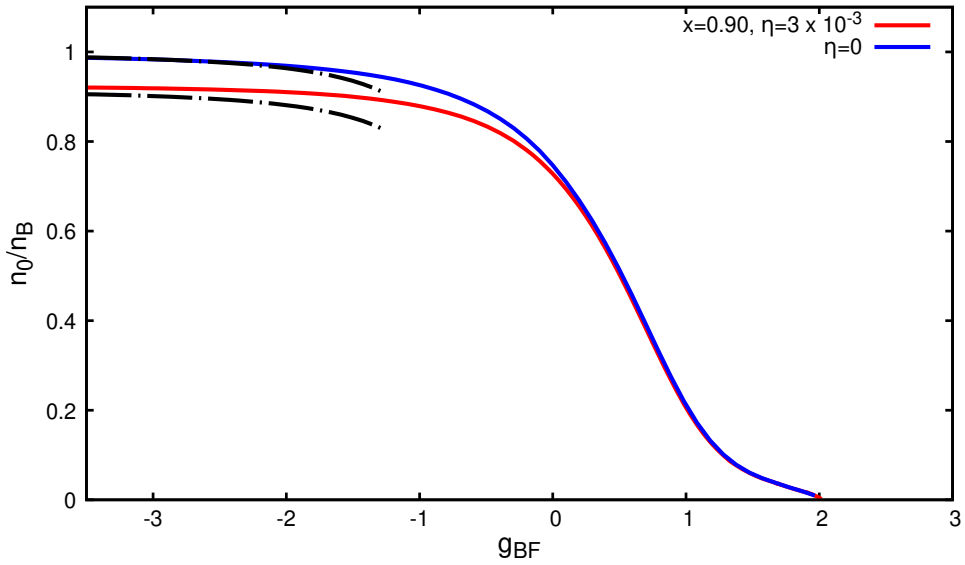

Figure 5.6: Condensate fractions $n_0/n_{\rm B}$ for $x = 0.9$ considering two different values of gas parameter η. The dash-dotted lines represent the perturbative expression (5.8).

lines represent the expected behaviours reported in Eq. (5.8) in the weak-coupling limit. At a fixed value of the concentration x the difference in the behaviour of $n_0/n_{\rm B}$ for $\eta = 3 \times 10^{-3}$ and $\eta = 0$ is manifest only in the weak-coupling region where most of the bosons are not bounded with fermions and the condensate fraction is dominated by the Bogoliubov result. Starting from unitarity, the condensate fraction is no longer dependent on the gas parameter and the critical value g_c results independent on η.

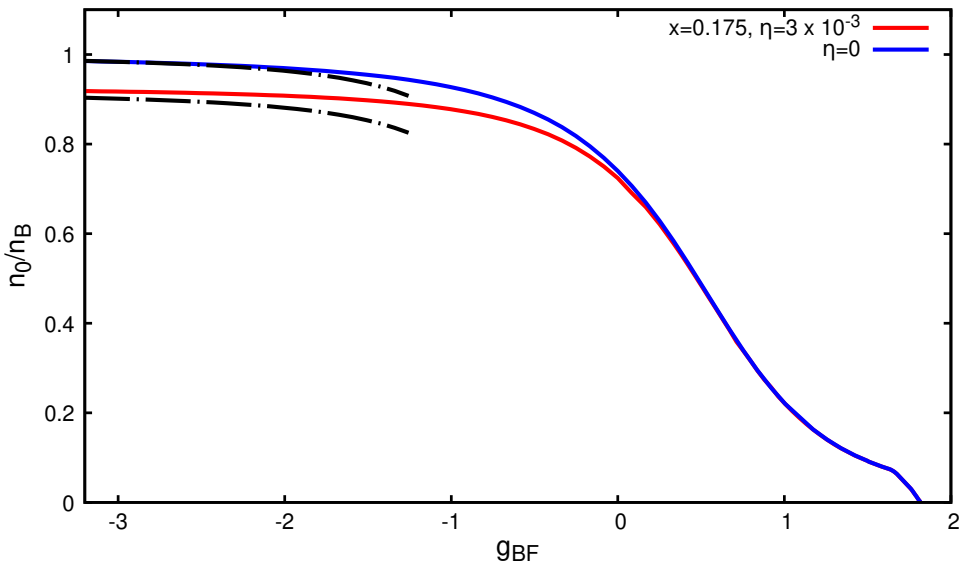

Figure 5.7: Condensate fractions n_0/n_B for $x = 0.175$ considering two different values of gas parameter η. The dash-dotted lines represent the perturbative expression (5.8).

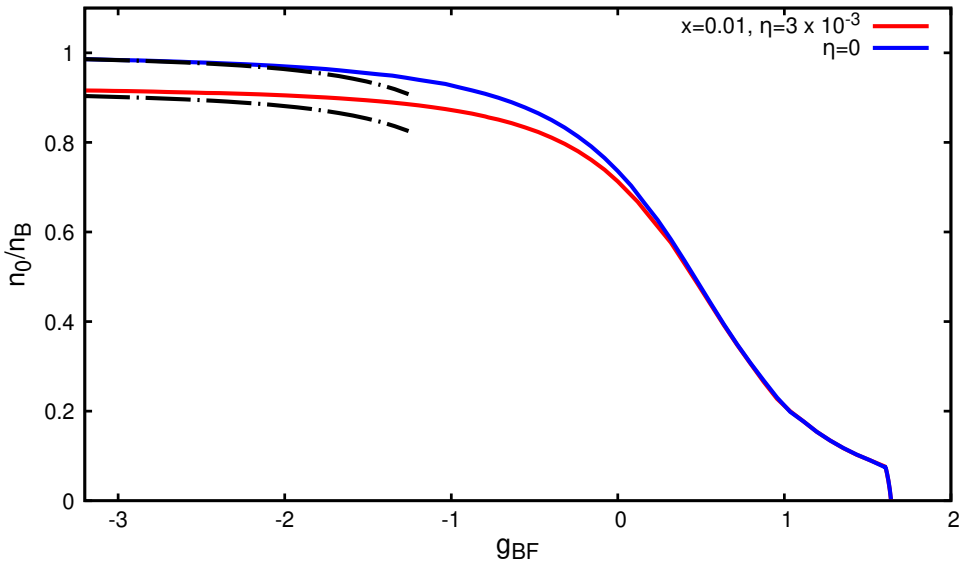

Figure 5.8: Condensate fractions n_0/n_B for $x = 0.01$ considering two different values of gas parameter η. The dash-dotted lines represent the perturbative expression (5.8).

5.2 BF mixtures with a majority of bosons

In this section I will present the numerical results obtained for an interacting Bose-Fermi mixture with a majority of bosons. As we will see, contrary to what one can expect, under some conditions even in this case the condensate fraction goes to zero in a certain BF coupling range. In this range the condensate fraction is completely suppressed showing a possible quantum phase transition from BEC

to a normal phase also in a mixture with a majority of bosons.

5.2.1 Asymptotic results for $x > 1$

In the weak coupling-regime, the expressions (5.1) and (5.2) for the chemical potentials μ_{B} and μ_{F} hold also for $x > 1$. The asymptotic expressions for the chemical potentials need instead to be modified in the strong-coupling limit for $x > 1$. This is because for $x > 1$ there will be a residual condensate density n_0 in the strong-coupling limit since for $n_{\mathrm{B}} > n_{\mathrm{F}}$ not all bosons can pair into molecules. One obtains in this limit for the bosonic chemical potential

$$\mu_{\mathrm{B}} = \frac{4\pi n_0 a_{\mathrm{BB}}}{m_{\mathrm{B}}} + \frac{2\pi n_{\mathrm{F}} a_{\mathrm{DB}}}{m_{\mathrm{DB}}} \tag{5.9}$$

where m_{DB} is the boson-dimer reduced mass $m_{\mathrm{DB}} = m_{\mathrm{B}} M/(m_{\mathrm{B}} + M)$ and a_{DB} is the boson-dimer s-wave scattering length. Its expression depends on the mass ratio $m_{\mathrm{B}}/m_{\mathrm{F}}$ as

$$a_{\mathrm{DB}} = -\frac{(1 + m_{\mathrm{B}}/m_{\mathrm{F}})^2}{1 + 2m_{\mathrm{B}}/m_{\mathrm{F}}} a_{\mathrm{BF}}. \tag{5.10}$$

The first term in Eq. (5.9) is the standard Bogoliubov result for a repulsive dilute Bose gas, while the second term in Eq. (5.9) is obtained by expanding Eq. (3.29) in the strong-coupling limit. In this case, the major contribution to the bare fermionic Green's function comes from the fermionic chemical potential μ_{F} which is large and negative and can be replaced by $-\epsilon_0$ with good approximation in this regime. The integral in Eq. (3.29) then reduces to Δ_∞^2, which in the strong-coupling limit is given by $\Delta_\infty^2 = 2\pi n_{\mathrm{F}}/\left(m_r^2 a_{\mathrm{BF}}\right)$. By combining this expression for Δ_∞^2 with ϵ_0 one recovers the second term in Eq. (5.9). It is important to notice the minus sign in front of the r.h.s. of the boson-dimer scattering length in Eq. (5.10). The interaction between unpaired bosons and Fermi molecules is attractive in a strong-coupling regime with a majority of bosons. This is due to the attraction between unpaired bosons and fermions bounded inside the molecules. On the contrary the strong-coupling scattering length is positive in a system with a majority of fermions, since the attraction between unpaired fermions and bounded bosons is strongly suppressed by the Pauli exclusion principle.

For the fermionic chemical potential in the strong-coupling limit one has

$$\mu_{\mathrm{F}} = \frac{(6\pi^2 n_{\mathrm{F}})^{2/3}}{2M} + \frac{2\pi a_{\mathrm{DB}}(n_{\mathrm{B}} - 2n_{\mathrm{F}})}{m_{\mathrm{DB}}} - \frac{4\pi a_{\mathrm{BB}}}{m_{\mathrm{B}}} n_0 - \epsilon_0. \tag{5.11}$$

Expression (5.11) can be explained very similarly to Eq. (5.4) for μ_{B} in the case $x < 1$.

It is indeed important to notice the exchanged role of bosonic and fermionic chemical potentials in the strong-coupling regime when one passes from $x < 1$ to $x > 1$. The asymptotic structure of μ_{B} for $x < 1$ in Eq. (5.4) is similar to the asymptotic expression for μ_{F} when $x > 1$ in Eq. (5.11). In both cases the chemical potentials tend to a value which contains the binding energy $-\epsilon_0$. The first term of Eq. (5.11) (which represents the Fermi energy of the fermionic molecules) is obtained form an analogous term in Eq. (5.4) by replacing n_{B} with n_{F} in the current case for $x > 1$, since in the situation with a majority of bosons the density of molecules is determined by n_{F} in the strong-coupling limit. Moreover the term representing the Fermi energy for unpaired fermions in Eq. (5.4) disappears when there are only unpaired bosons in the strong-coupling limit.

In the same way the chemical potentials μ_{F} in Eq. (5.5) and μ_{B} in Eq. (5.9) are related. In both cases, the second terms are connected with the BF interaction. The sign difference is due to the fact that, as it was said before, the BF interaction between unpaired bosons and fermions bounded with bosons is attractive in the strong-coupling limit, while the interaction between unpaired fermions and bounded bosons is compensated by the Pauli exclusion principle, resulting in a repulsive residual interaction. Finally, the difference between the two first terms of Eqs. (5.5) and (5.9) is due to the fact that a boson added to the system for $x > 1$ will experience a mean-field repulsion with the condensed bosons, while a fermion added to the system for $x > 1$ will be placed at the Fermi level of the unpaired fermions.

5.2.2 Numerical results for $x > 1$

The bosonic chemical potentials obtained numerically are reported in Fig 5.9 throughout the entire BF resonance for some values of $1.4 \leq x \leq 1.9$. The perturbative expression in the weak-coupling limit and the asymptotic result in the strong-coupling regimes are also shown as a comparison with the numerical results. In the weak-coupling region, the bosonic chemical potential decreases with the increasing of the BF interaction, following Eq. (5.1). It then reaches a minimum value, whose position depends weakly on the density ratio. From this value of coupling, the bosonic chemical potential starts to increase because of a decrease of the attraction between unpaired bosons and Fermi molecules which scales with $\frac{1}{g_{\mathrm{BF}}}$. In the strong-coupling limit μ_{B} then follows the asymptotic

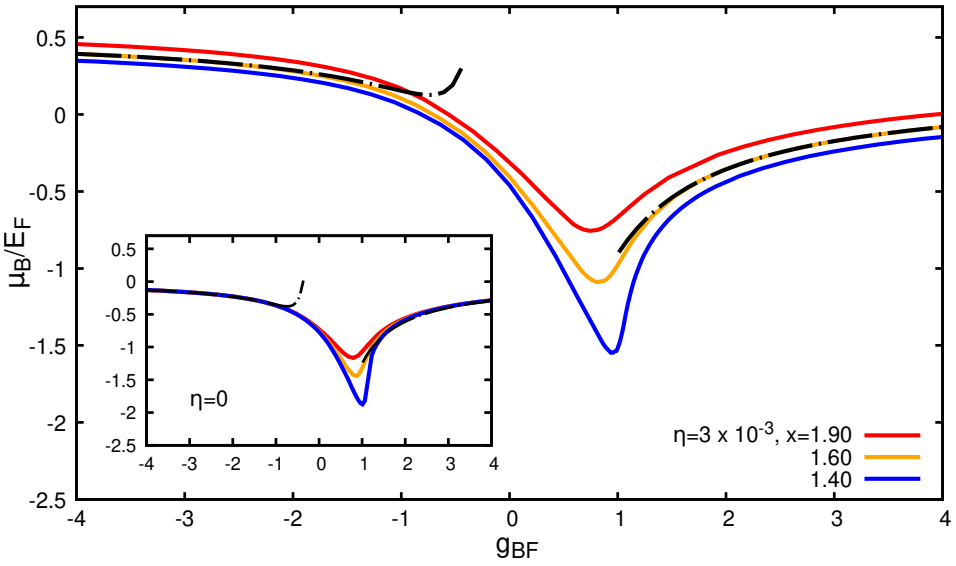

Figure 5.9: Bosonic chemical potentials vs g_{BF} for different values of $x \geq 1.4$. The main plot reports the results for a BF mixture with a gas parameter $\eta = 3 \times 10^{-3}$. The dash-dotted lines represent the weak and strong asymptotic behaviours (reported only for $x = 1.6$ for clarity). In the inset, the bosonic chemical potentials are reported for a gas parameter $\eta = 0$.

behaviour given by Eq (5.9).

The fermionic chemical potentials are instead reported in Figs. 5.10 and 5.11 for gas parameters $\eta = 0$ and $\eta = 3 \times 10^{-3}$, respectively. In the main plots the binding energy $-\epsilon_0$ has been subtracted to the value μ_{F} obtained numerically for positive values of g_{BF}, while in the insets we report μ_{F} without this subtraction (to emphasize its monotonic behaviour). One can notice that, in the main plots, the slope of the curve in the strong-coupling region is reduced by increasing the value of x and it will change sign for $x \geq 2$, as it is shown by the second term of Eq. (5.11).

The condensate fractions n_0/n_{B} obtained for $x \geq 1.4$ are reported in Fig. 5.12. In the weak-coupling limit the condensate fractions tend to the Bogoliubov value given by Eq. (5.7), while for $g_{\mathrm{BF}} \gg 1$ the system reduces to a mixture of unpaired bosons and fermionic molecules, with an expected value for the condensate density given by

$$n_0 = \left[1 - \frac{8}{3}\sqrt{\frac{n_{\mathrm{UB}} a_{\mathrm{BB}}}{\pi}}\right] n_{\mathrm{UB}} \tag{5.12}$$

where $n_{\mathrm{UB}} = n_{\mathrm{B}} - n_{\mathrm{F}}$ is the density of the unpaired bosons. In Fig. 5.12 the condensate fractions have been reported for more values of x with respect to the previous graphs regarding chemical potentials in order to underline the evolution

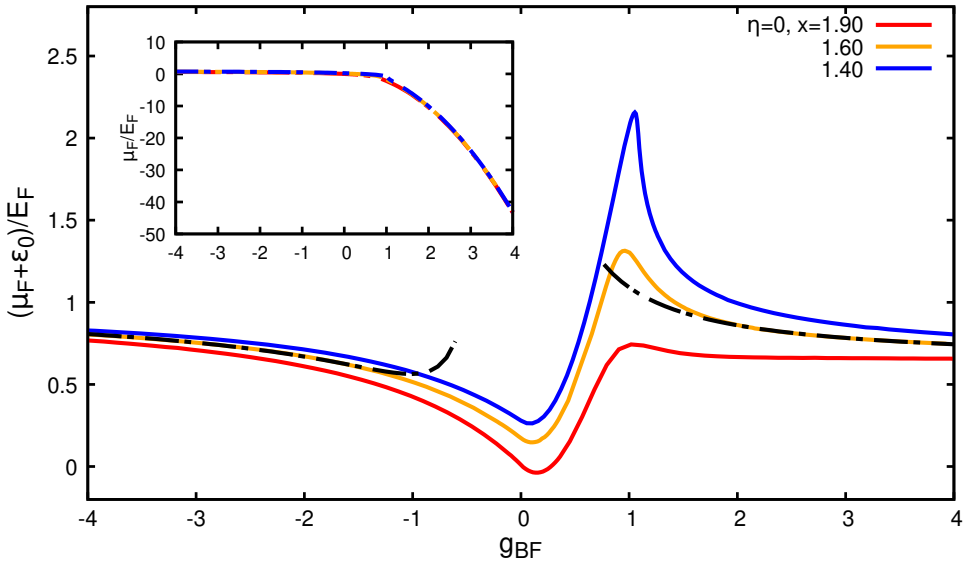

Figure 5.10: Fermionic chemical potentials minus the binding energy $-\epsilon_0$ (for positive values of $g_{\rm BF}$) vs $g_{\rm BF}$ for various values of $x \geq 1.4$ and $\eta = 0$. In the inset the values of $\mu_{\rm F}$ are reported. In the weak-coupling limit the fermionic chemical potential tends to $E_{\rm F}$ following the analytical behaviour (5.2) (dash-dotted line in the weak-coupling region), while in the strong-coupling regime $\mu_{\rm F} + \epsilon_0$ follows the behaviour of Eq. (5.11) (dash-dotted line in the strong-coupling region).

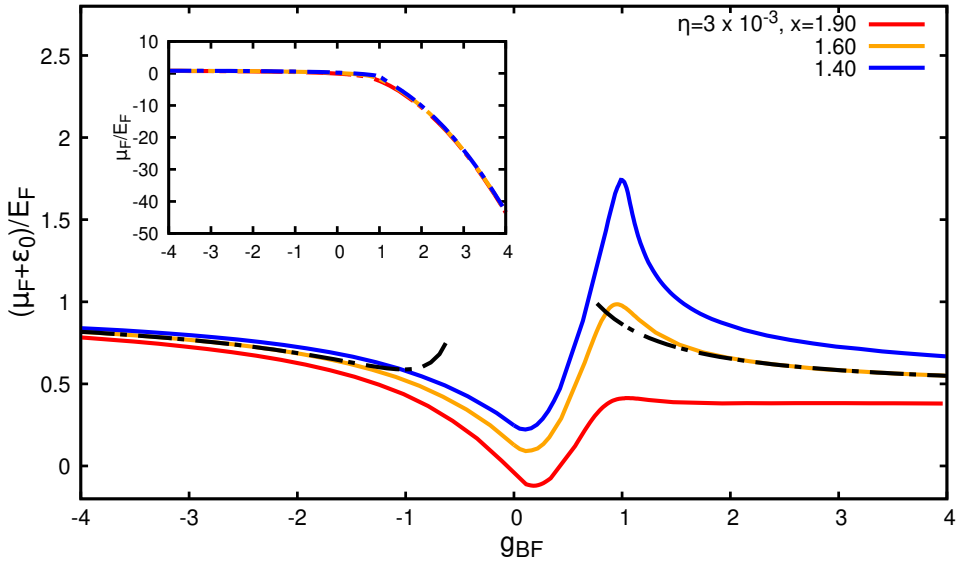

Figure 5.11: Fermionic chemical potentials minus the binding energy $-\epsilon_0$ (for positive values of $g_{\rm BF}$) vs $g_{\rm BF}$ for various $x > 1.4$ and $\eta = 3 \times 10^{-3}$. In the inset are reported the values of $\mu_{\rm F}$ as functions of $g_{\rm BF}$. In the weak-coupling limit the fermionic chemical potential tends to $E_{\rm F}$ following the analytical behaviour in Eq. (5.2) (dash-dotted line in the weak-coupling region), while in the strong-coupling limit the dash-dotted line represents the expression given by Eq. (5.11).

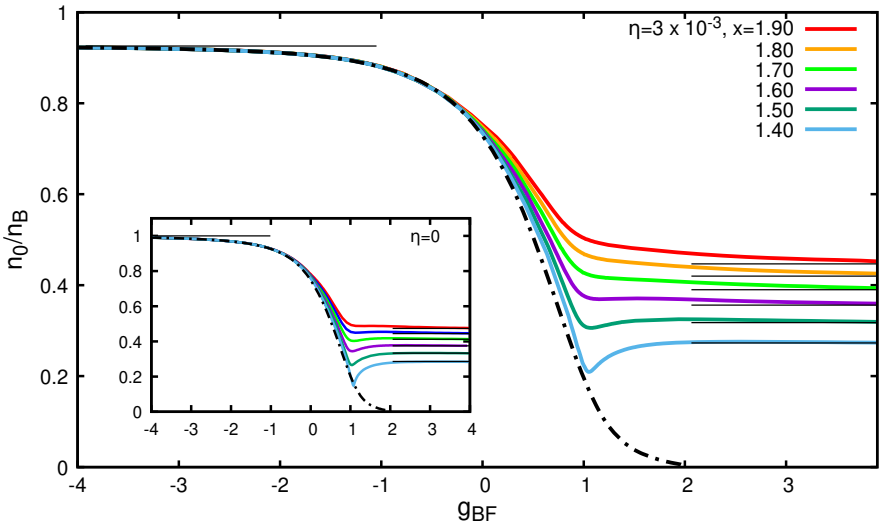

Figure 5.12: Condensate fractions n_0/n_B vs g_{BF} for some values of $x \geq 1.4$. The condensate fractions obtained for $\eta = 3 \times 10^{-3}$ are presented in the main plot. The dash-dotted line represents the condensate fraction behaviour obtained numerically for $x = 1$. Both in the weak-coupling and strong-coupling limits n_0/n_B approaches the Bogoliubov values (black full lines) given in Eqs. (5.7) and (5.12). The condensate fractions for a null gas parameter $\eta = 0$ are shown in the inset.

of the curves for decreasing values of x, starting from $x = 1.9$. One notice that the universal behaviour of n_0/n_B previously found for $x \leq 1$ is now valid only for the initial part of the curve, until $g_{BF} \simeq 0$, after which the different asymptotic values of n_0, given by Eq. (5.12), rule the behaviours of the corresponding curves. In particular, one sees that as x decreases from 1.9 to 1.4, the condensate fraction follows the curve corresponding to the case $x = 1$ (dash-dotted line) over a larger and larger range of g_{BF}, until it comes to a minimum to then reach from bellow the asymptotic value given by Eq. (5.12). We will see now that in the range $1.0 < x \lesssim 1.3$ the minimum value of n_0 may reach 0, with the presence of an unexpected quantum phase transition.

In the range of the density ratio $1.0 < x \lesssim 1.3$, the values of μ_B, μ_F, and n_0 obtained by solving Eqs. (3.36 - 3.38), present unexpected behaviours in a range of BF couplings between unitarity and the strong-coupling limit. In particular, in this range of coupling I have found multiple solutions for $1.04 \lesssim x \lesssim 1.3$ and no solutions with $n_0 \neq 0$ in the range $1.0 < x \lesssim 1.04$. In the following figures the solutions of Eqs. (3.36 - 3.38) will be presented in a small range of BF coupling where multiple or no solutions with $n_0 \neq 0$ have been found. Outside of this range the numerical results follow the same behaviour presented in Figs. 5.9 - 5.12 reaching the expected values, through the various asymptotic behaviours reported

previously, both in the weak-coupling and strong-coupling limits.

Let us start from the condensate fraction which presents the most interesting pattern for $1.0 < x \lesssim 1.3$. In Figs. 5.13 and 5.14 the condensate fractions obtained numerically are presented for some values of $1.01 \leq x \leq 1.3$ and for $\eta = 3 \times 10^{-3}$ and $\eta = 0$, respectively. Each of these two figures has been divided into three panels corresponding to three different behaviours of the condensate fraction occurring in this range of x. Coming from small values of $g_{\rm BF}$, the condensate fraction goes to zero as in the case of a mixture with a majority of fermions for different values of the BF interaction depending on the concentration of the system. These critical values of $g_{\rm BF}$ become greater and greater as x decreases, tending to the value obtained for $x = 1$ (dashed line in the last panel). This result was not expected for a system with majority of bosons, since in the strong-coupling limit the expectation value of the condensate fraction in Eq. (5.7) is different from zero. In order to understand better the situation, I have searched for solutions starting from the strong-coupling limit, using as trial starting values for $\mu_{\rm F}$ and n_0 the expressions in Eqs. (5.11) and (5.12). The values of the condensate fraction which solve Eqs. (3.36 - 3.38) in the strong-coupling limit correspond to the right branches in Figs. 5.13 and 5.14. For $1.1 \leq x \leq 1.3$, coming from higher values of $g_{\rm BF}$, the condensate fraction decreases with $g_{\rm BF}$ until it vanishes at the same $g_{\rm BF}$ obtained by following the left branch of the curve.

However for $1.04 \leq x < 1.1$ (second panel in Figs. 5.13 and 5.14), g_c obtained from the left branch overcomes the value of g_c obtained by following the right branch, with a double solution in a limited range of couplings. The stable solution should be found in principle by comparing the energy of the two solutions, a calculation that we did not perform in the present work. Finally for $1 < x \leq 1.04$ a gap appears between the two branches, corresponding to a region where $n_0 = 0$. The extension of this gap progressively increases as $x \to 1^+$, with the right branch of the solution with $n_0 \neq 0$ being pushed to larger and larger coupling, with the left branch instead approaching the curve corresponding to $x = 1$.

The various values of $\mu_{\rm B}$ obtained numerically for $1.01 \leq x \leq 1.3$ are reported in Fig. 5.15 for $\eta = 3 \times 10^{-3}$ and in Fig. 5.16 for $\eta = 0$, while the values of $\mu_{\rm F}$ are reported in Fig. 5.17 for $\eta = 3 \times 10^{-3}$ and in Fig. 5.18 for $\eta = 0$.

Comparing the graphs for $\mu_{\rm B}$ obtained for $1.01 \leq x \leq 1.3$ with those for $1.4 \leq x \leq 1.9$ (Fig. 5.9), one can see that the minimum of $\mu_{\rm B}$ becomes more and more pronounced for decreasing values of x. In addiction, for $x < 1.3$ $\mu_{\rm B}$ presents a jump, after which it recovers the expected strong-coupling value. The numerical

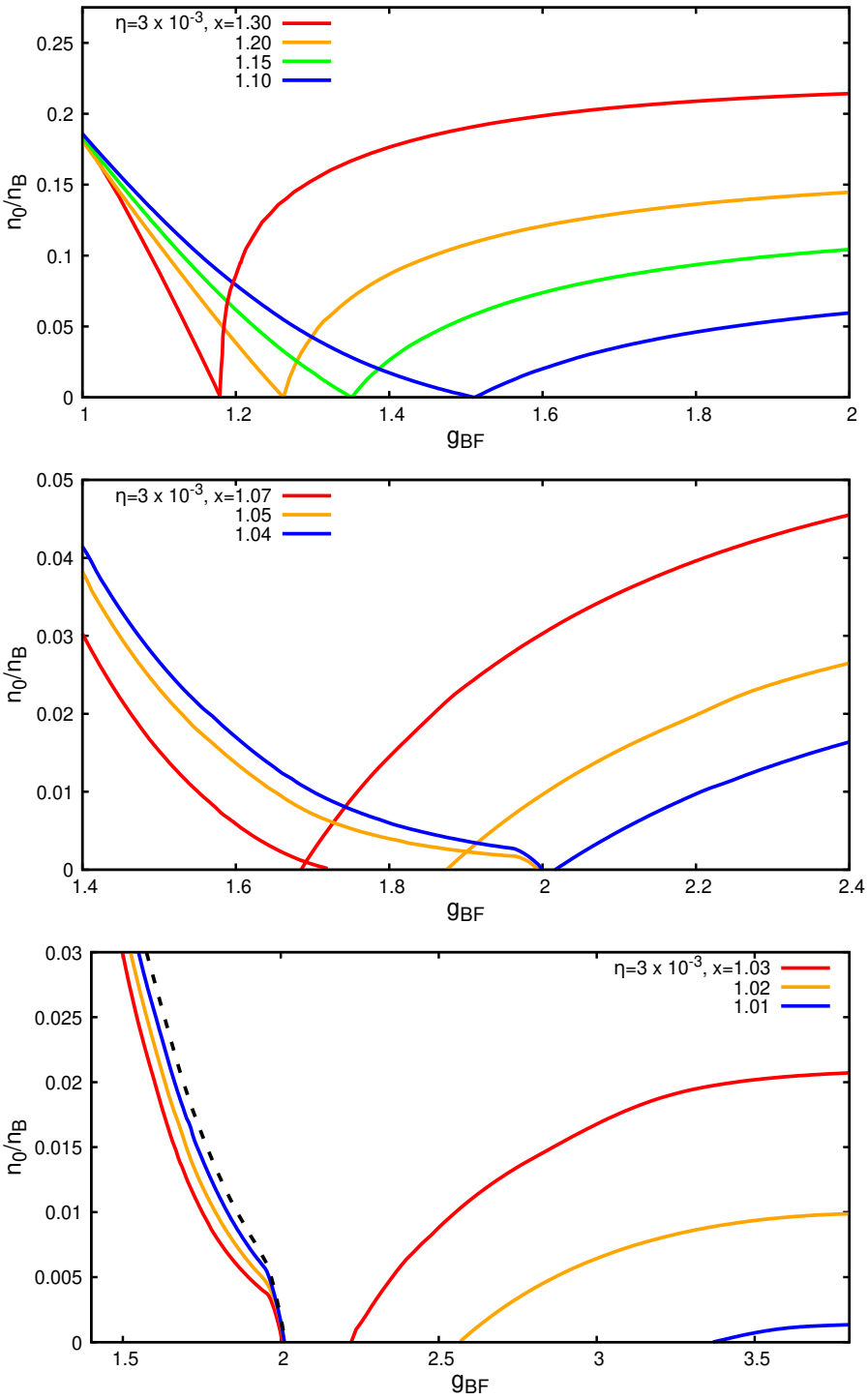

Figure 5.13: Condensate fractions n_0/n_B for different values of $1.0 < x \lesssim 1.3$ as functions of g_BF for a gas parameter $\eta = 3 \times 10^{-3}$. The dashed line in the bottom panel represents the numerical result obtained for $x = 1$.

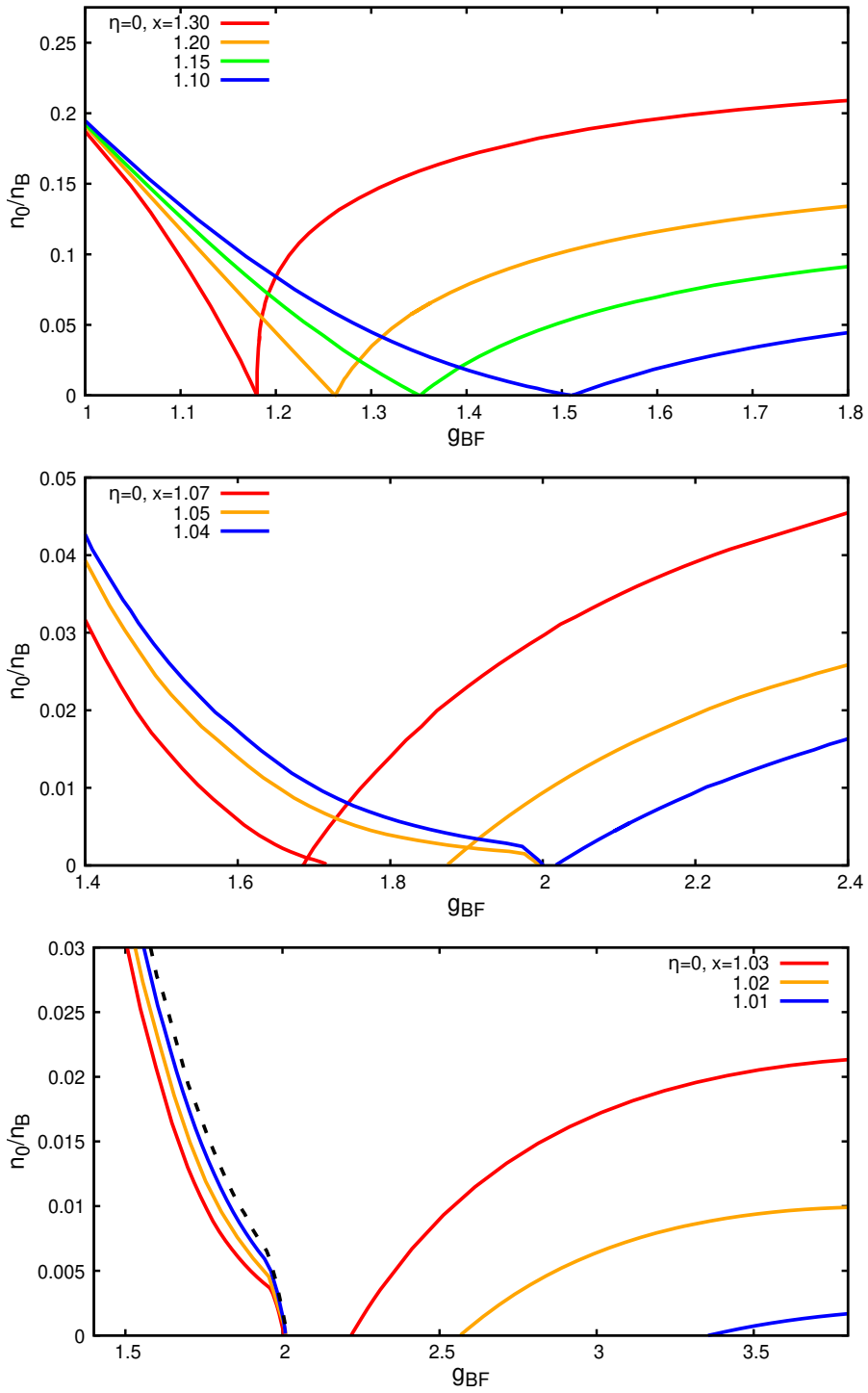

Figure 5.14: Condensate fractions n_0/n_{B} for different values of $1.0 < x \lesssim 1.3$ as functions of g_{BF} for a gas parameter $\eta = 0$. The dashed line in the bottom panel represents the numerical result obtained for $x = 1$.

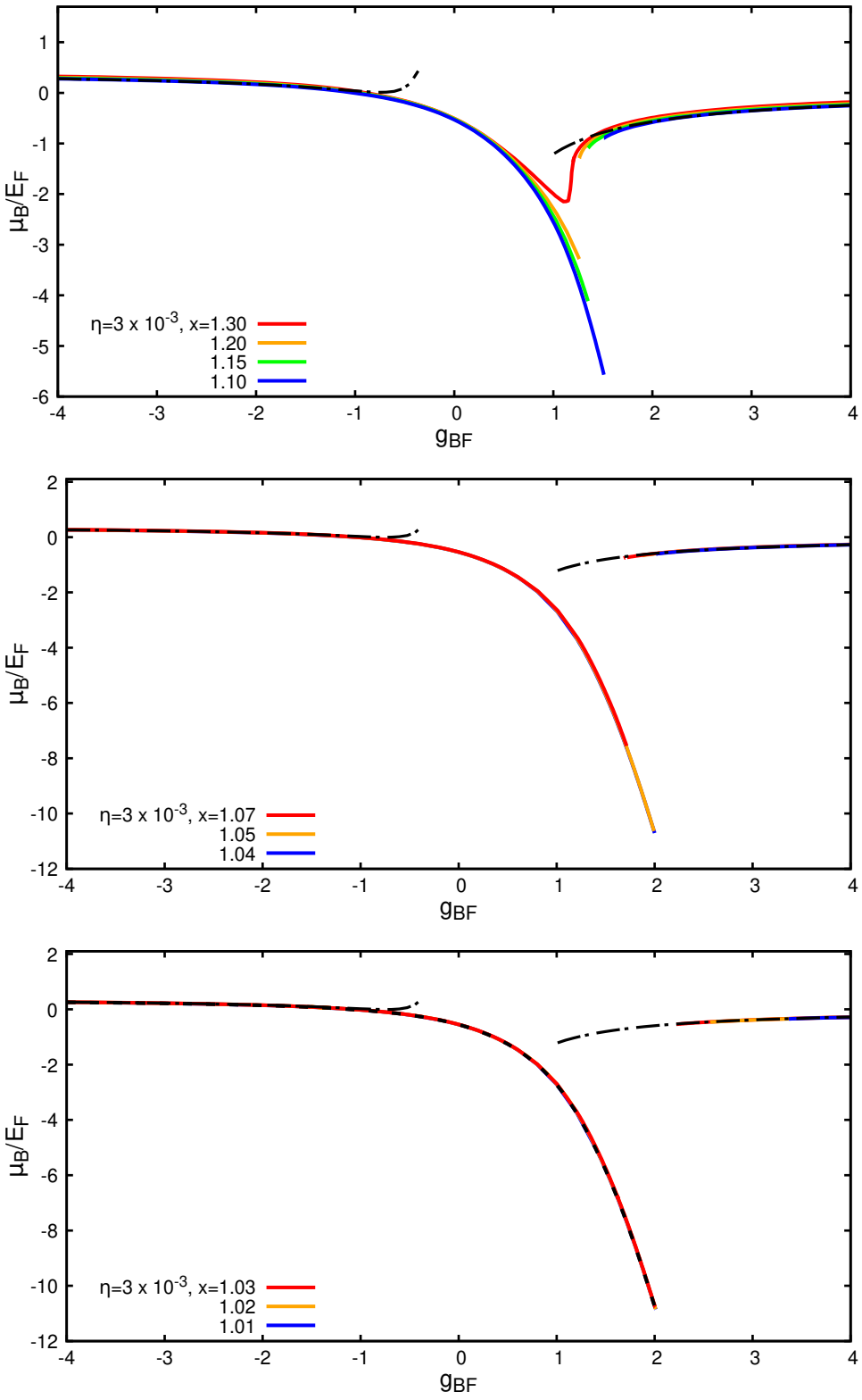

Figure 5.15: Bosonic chemical potentials obtained for different values $1.01 \leq x \lesssim 1.3$ and $\eta = 3 \times 10^{-3}$. The dash-dotted lines represent the asymptotic values for μ_{B} given by Eq. (5.1) in the weak-coupling region and the asymptotic expression given by Eq. (5.9) in the strong-coupling region. The dotted line in the last panel represents the numerical result obtained for $x = 1$

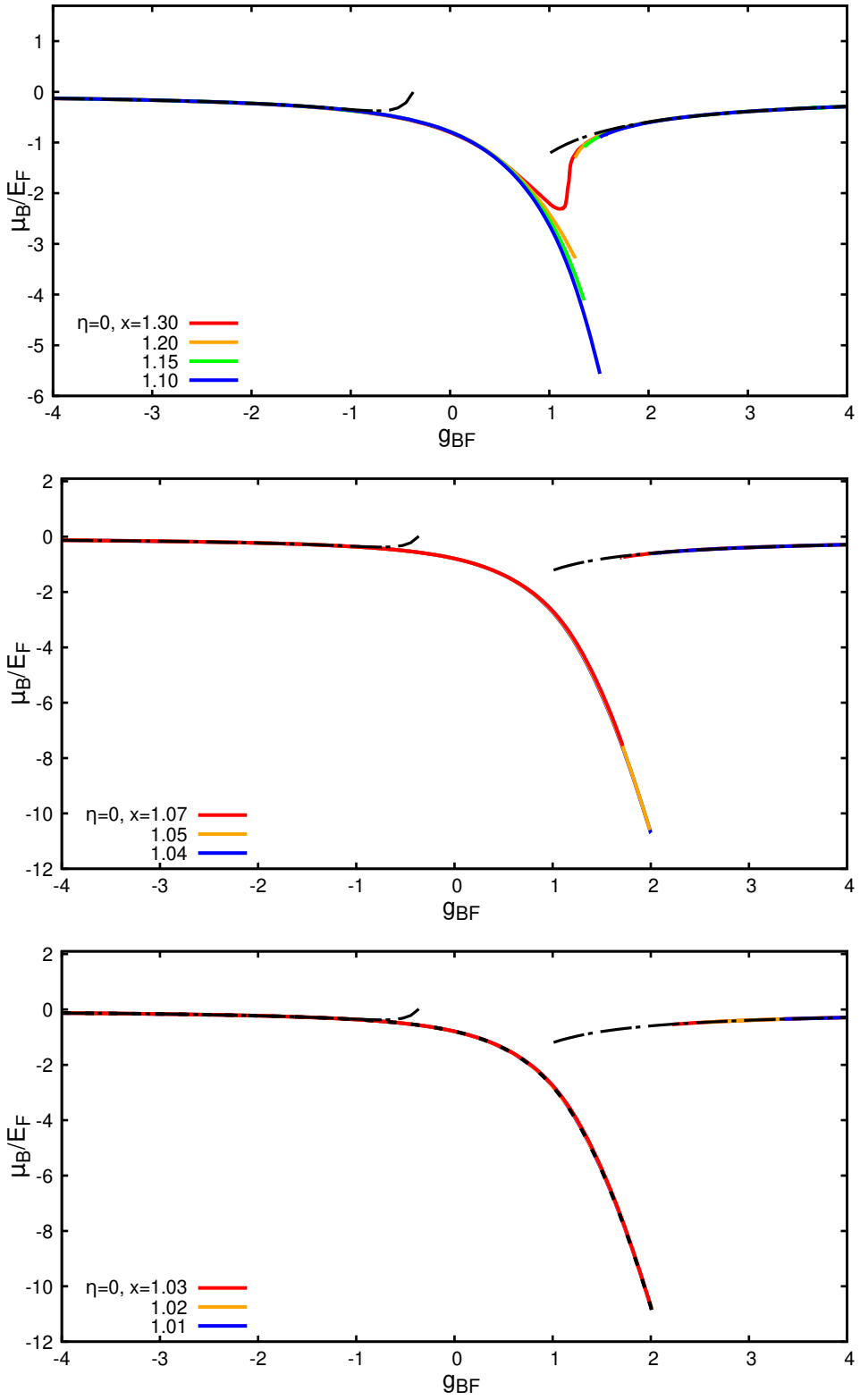

Figure 5.16: Bosonic chemical potentials obtained for various values $1.01 \leq x \lesssim 1.3$ and $\eta = 0$. The dash-dotted lines represent the expectation values for μ_{B} given by Eq. (5.1) in the weak-coupling region and by Eq. (5.9) in the strong-coupling region. The dotted line in the bottom panel represents the numerical result obtained for $x = 1$

values for $\mu_{\rm B}$ obtained for $x = 1$ are represented by a dash line in the last panel.

For the fermionic chemical potential instead, it is the maximum of $\mu_{\rm F} + \epsilon_0$ that becomes more and more prominent as $x \to 1^+$ (see Figs. 5.10 and 5.11) before approaching the strong-coupling asymptotic value. As it was for $\mu_{\rm B}$, also the fermionic chemical potential experiences a discontinuity for $1.01 \leq x \leq 1.3$ in the range of $g_{\rm BF}$ in which the condensate fraction goes to zero or it has a double solution.

In order to understand better the behaviour of the BF mixture in the parameter region where $n_0/n_{\rm B}$ presents a gap, I have studied the system at two specific values of density ratio $x = 1.01, 1.03$ and in the specific range of the BF coupling where the condensate fractions exhibit a gap, setting $n_0/n_{\rm B} = 0$ identically. In particular, I looked for the bosonic and fermionic chemical potentials which connect the two branches obtained for $n_0 > 0$. In Figs 5.19 and 5.20 I reported in the same plot the values of $\mu_{\rm B}$ and $\mu_{\rm F}$ for $x = 1.03$ and $x = 1.01$, respectively, using a gas parameter $\eta = 3 \times 10^{-3}$ ($\eta = 0$ in the insets). The dashed and dotted lines represent the numerical solutions obtained in the range of $g_{\rm BF}$ where the condensate fraction presents a gap, i.e. where in Eqs. (3.36) and (3.37) I have set $n_0 = 0$ identically. The full lines correspond instead to the values of $\mu_{\rm B}$ and $\mu_{\rm F}$ found for values of the BF coupling where $n_0 \neq 0$. The left branches of $\mu_{\rm B}$ and $\mu_{\rm F}$ in the condensed phase go on in a smooth way in the normal phase into a solution with $n_0 \neq 0$ (dotted line) which ends at values of $g_{\rm BF}$ where the right branch already exists. The right branch with $n_0 \neq 0$ continues instead in a normal phase solution (dashed line) with an angular point. This solution, by reducing $g_{\rm BF}$, merges into the solution (dotted line) obtained by following the left branch with a second angular point. So, also in this case, two solutions exist in a certain coupling range, and a minimization of the energy should be performed to find the stable one. From Fig. 5.19 one can notice that there is a sort of exchange of role between the chemical potentials $\mu_{\rm B}$ and $\mu_{\rm F}$ when passing from the left branch to the right branch through the gap region.

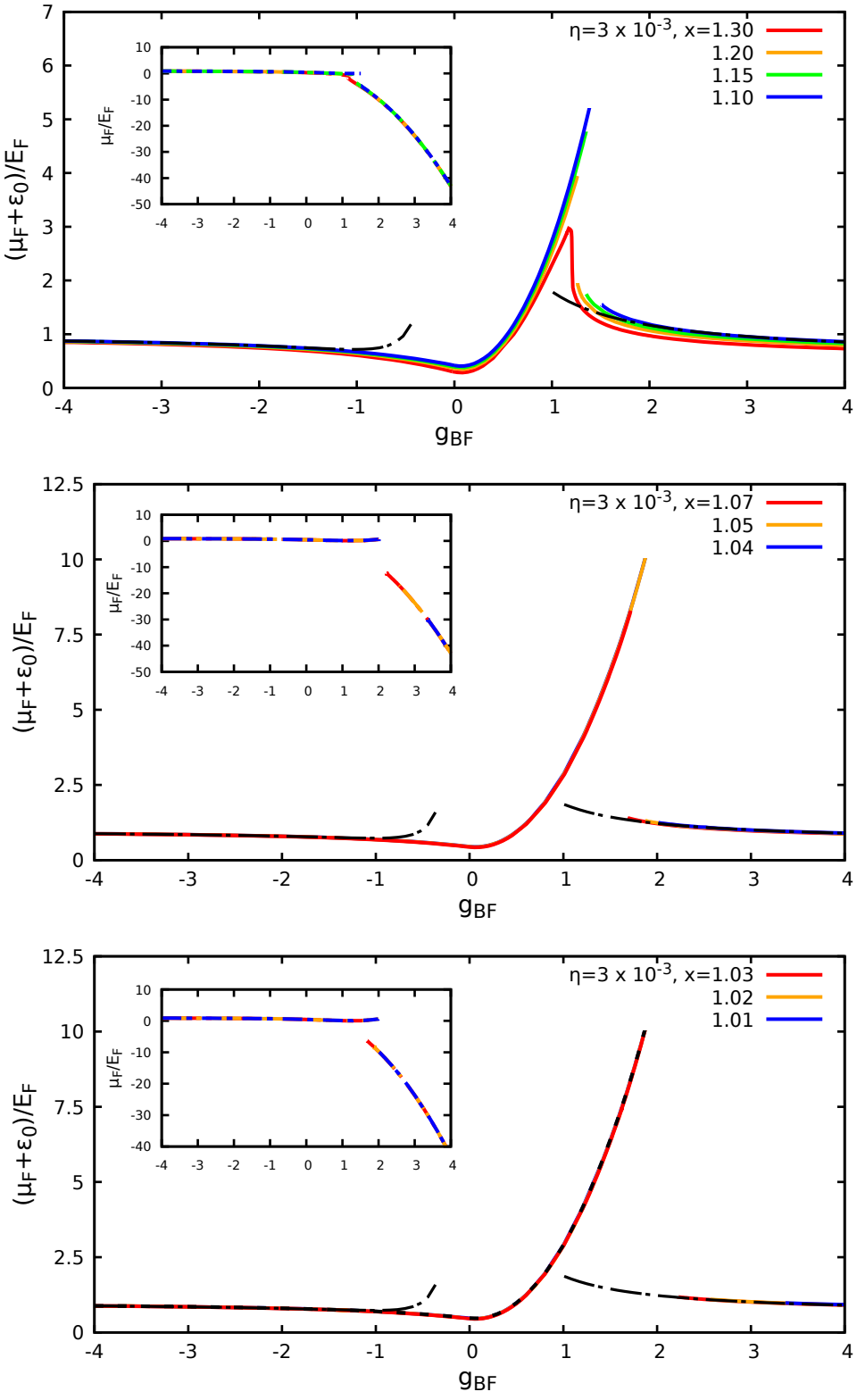

Figure 5.17: Fermionic chemical potentials minus the binding energy (for $g_{\mathrm{BF}} \geq 0$) obtained for various values $1.01 \leq x \lesssim 1.3$ and $\eta = 3 \times 10^{-3}$. The dash-dotted lines represent the asymptotic values for μ_{F} given by Eq. (5.2) in the weak-coupling region and by Eq. (5.11) in the strong-coupling region. The dotted line corresponds to the case $x = 1$.

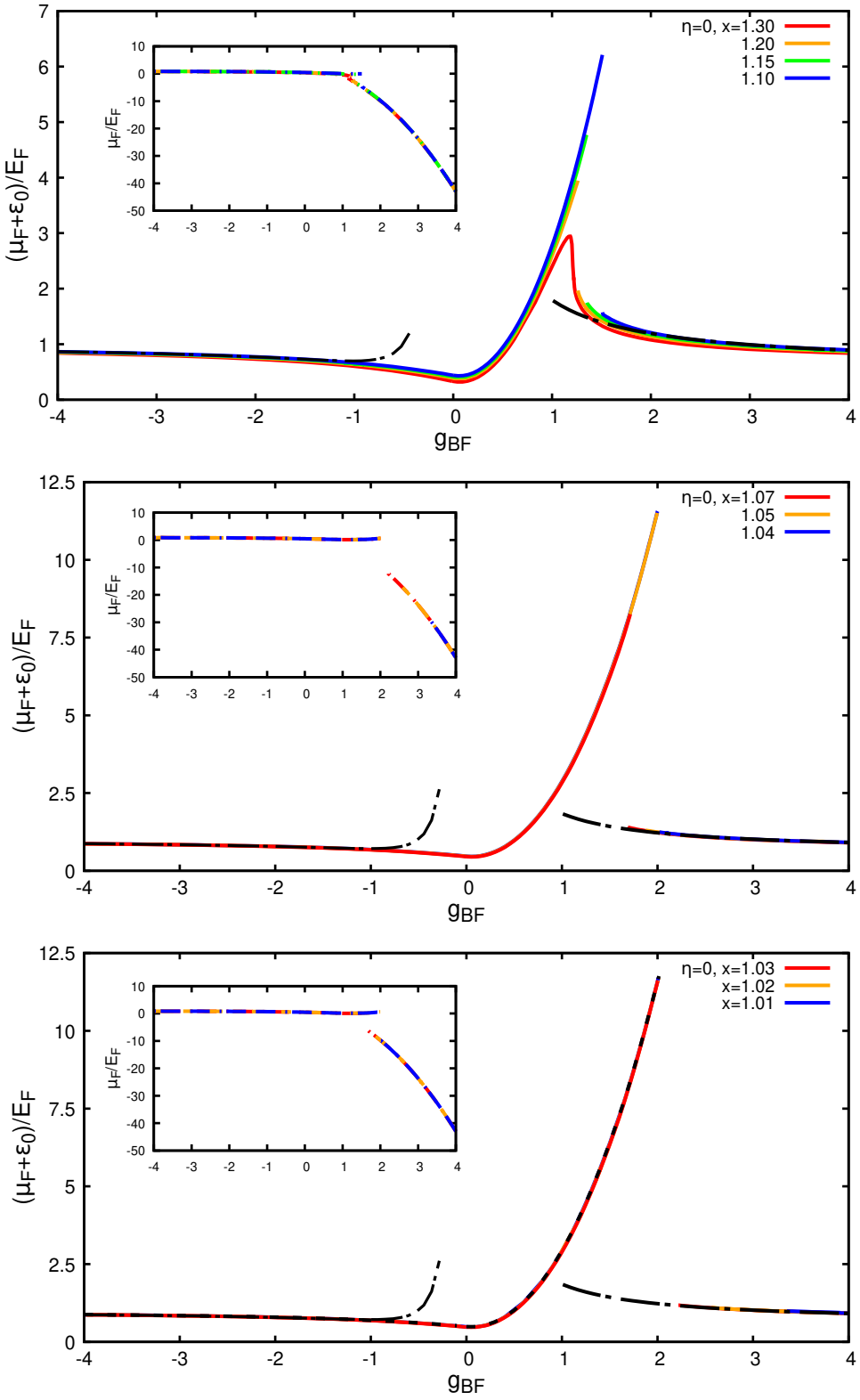

Figure 5.18: Fermionic chemical potentials minus the binding energy (for $g_{\mathrm{BF}} \geq 0$) obtained for different values $1.01 \leq x \lesssim 1.3$ and $\eta = 0$. The dash-dotted lines represent the asymptotic values for μ_{F} given by Eq. (5.2) in the weak-coupling region and by Eq. (5.11) in the strong-coupling region. The dotted line corresponds to the case $x = 1$.

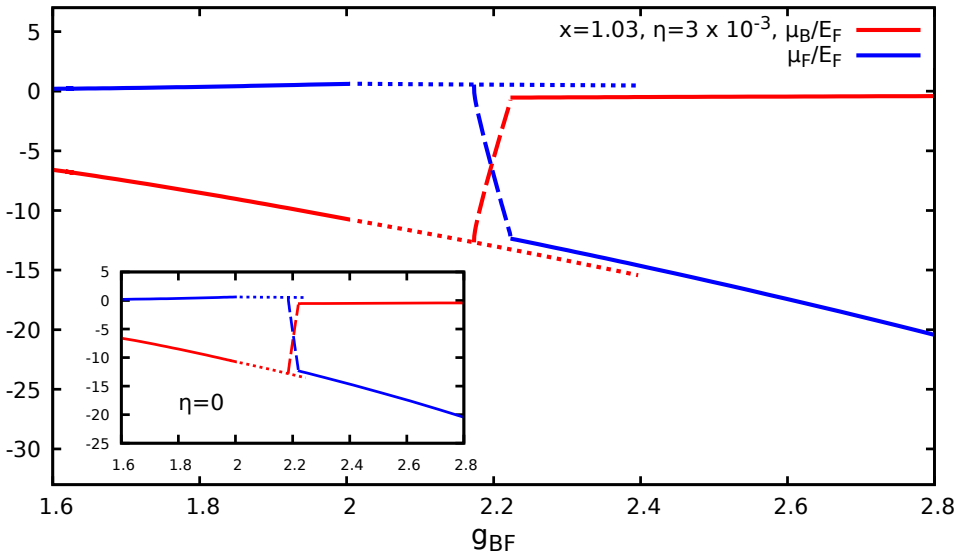

Figure 5.19: Bosonic and fermionic chemical potentials vs g_{BF} for $x = 1.03$ and $\eta = 3 \times 10^{-3}$. The full lines represent the chemical potentials obtained for $n_0/n_{\mathrm{B}} > 0$, while the dashed and dotted lines are different solutions with $n_0 = 0$. In the inset the chemical potentials are plotted for a BF mixture with $\eta = 0$.

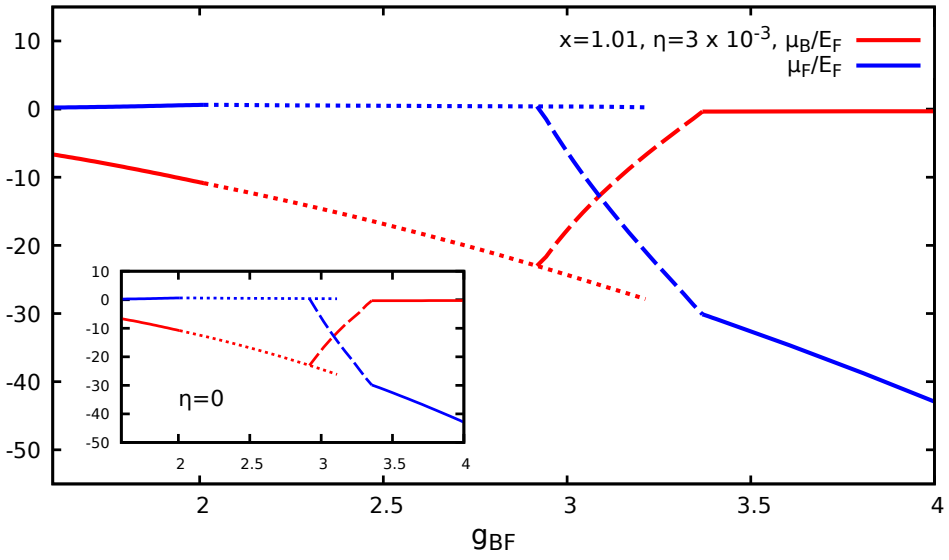

Figure 5.20: Bosonic and fermionic chemical potentials vs g_{BF} for $x = 1.01$ and $\eta = 3 \times 10^{-3}$. The full lines represent the chemical potentials obtained for $n_0/n_{\mathrm{B}} > 0$, while the dashed and dotted lines are different solutions obtained with $n_0 = 0$. In the inset the chemical potentials are plotted for a BF mixture with a bosonic gas parameter $\eta = 0$.

5.3 Fermi momenta of Γ, T and G_F

In this section I will present the results of the Fermi momenta of the Γ-matrix, T-matrix, and dressed fermionic Green's function G_F obtained for a BF mixture with a majority of bosons. In particular I will focus on the case with a BB repulsion given by a gas parameter $\eta = 3 \times 10^{-3}$ (the results obtained for $\eta = 0$ are very similar and will not be presented). The Fermi momenta of the Γ-matrix and of the T-matrix have been found by solving the equations $\mathrm{Re}\,\Gamma(\mathbf{P},0)^{-1} = 0$ and $\mathrm{Re}\,\mathrm{T}(\mathbf{P},0)^{-1} = 0$, respectively. $\mathrm{Re}\,\Gamma(\mathbf{P},0)^{-1}$ is a monotonically increasing function of $|\mathbf{P}|$, and presents a zero P^0_Γ above a certain value of g_{BF} which depends on x. On the contrary, $\mathrm{Re}\,\mathrm{T}(\mathbf{P},0)^{-1}$ has a divergence for $|\mathbf{P}| = k_{\mu_F}$ and has a zero at position $P^0_{T1} > k_{\mu_F}$ throughout the entire BF resonance. For $x \geq 1.07$, our numerical results indicate that the T-matrix presents a second Fermi momentum at $P^0_{T2} < k_{\mu_F}$ for g_{BF} greater than a certain value. It is important to notice that this second jump appears, for $x > 1$, only in the range of x where the condensate fraction has a double solution or a gap in g_{BF} (see the last two panels of Fig. 5.13).

The various results for the Fermi momentum P^0_Γ are reported in Fig. 5.21. Starting from $x = 1.9$, the value of g_{BF} at which P^0_Γ appears decreases with x

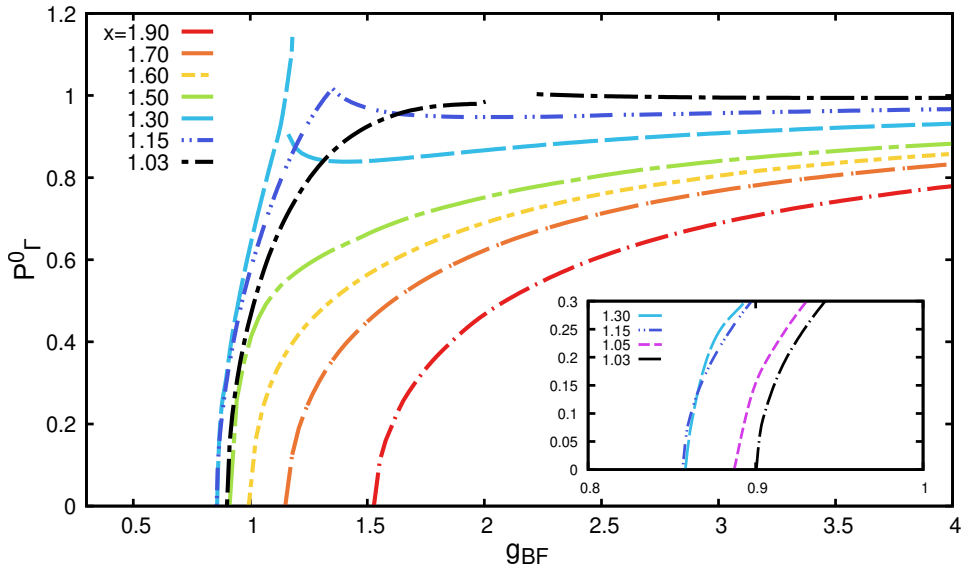

Figure 5.21: Fermi momenta of the Γ-matrix for various values of $x > 1.0$ as functions of g_{BF}. The gas parameter η is fixed to 3×10^{-3}. In the inset the appearance P^0_Γ in the limit $x \to 1^+$ has been highlighted.

until $x \sim 1.15$ (see inset of Fig. 5.21). At this point the value of g_{BF} at which the Γ-matrix starts to present a jump increases, reaching then the value found

for $x = 1.0$ (not shown in this picture). One can notice that the general shape of P^0_Γ as a function of g_{BF} undergoes a distinct change for $x \leq 1.3$, i.e. in the region where n_0 vanishes (at a single value of g_{BF} or over an extended range).

The Fermi momenta of the T-matrix are reported in Fig. 5.22. In the left

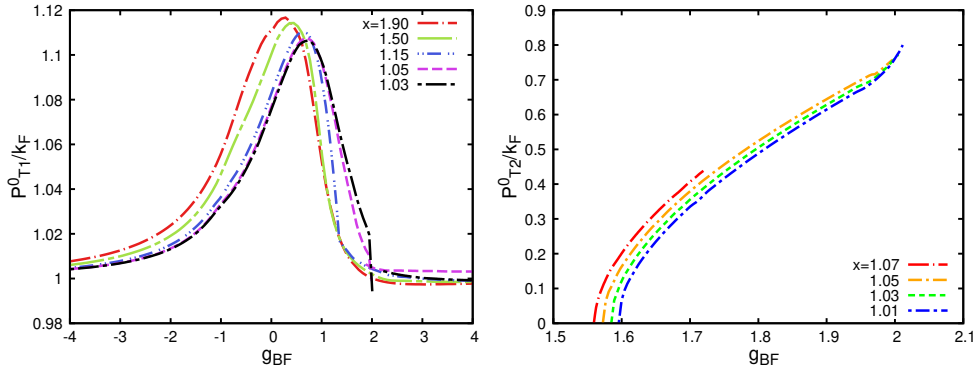

Figure 5.22: Fermi momenta of the T-matrix for various values of $x > 1.0$. The gas parameter η is fixed to 3×10^{-3}. In the left panel the first momentum $P^0_{T1} > k_{\mu_F}$ appears for all the values of $x > 1.0$ studied throughout the entire resonance. In the right panel the second momentum $P^0_{T2} < k_{\mu_F}$ is present only for $x \leq 1.07$ and above a certain value of the BF coupling.

panel, the momentum P^0_{T1} is showed throughout the entire resonance for various BF concentrations. The presence of a peak in the unitarity region ($g_{BF} \simeq 0$) is common to all values of x and its position is shifted to higher values of g_{BF} as n_B/n_F is reduced. The right panel shows the second Fermi momentum P^0_{T2} of the T-matrix, which appears only in the strong-coupling region and for values of x at which double solutions of n_0/n_B, or an extended region with $n_0 = 0$, were found. This second momentum P^0_{T2} is found only for the left branch of n_0.

The Fermi momenta of the dressed fermionic Green's function were found numerically by solving the equation $\mathrm{Re}\, G_F(\mathbf{P}, 0)^{-1} = 0$, with G_F given by Eq. (3.33). The results are reported in Fig. 5.23. As it was for the T-matrix, also G_F has a Fermi momentum $k_{F1} > P^0_\Gamma$ throughout the entire resonance and a second momentum $k_{F2} < P^0_\Gamma$ only above a certain value of BF coupling. The Fermi momentum k_{F1} remains pinned at k_F from the weak-coupling limit until $g_{BF} \simeq 0$. We recall that the Luttinger theorem [56] states that in a Fermi liquid the value of the Fermi momentum (i.e. the position of the jump in the momentum distribution) is not changed by interaction. We thus see that in our BF mixture deviations from the Fermi liquid behaviour start to occur at $g_{BF} \simeq 0$. After this coupling value, k_{F1} begins to depart from k_F, with a non-monotonic behaviour which depends on the value of x (with qualitative differences between the behaviour found for $x \gtrsim 1.4$ and $1 < x \lesssim 1.4$). The position of the second Fermi momentum is presented in

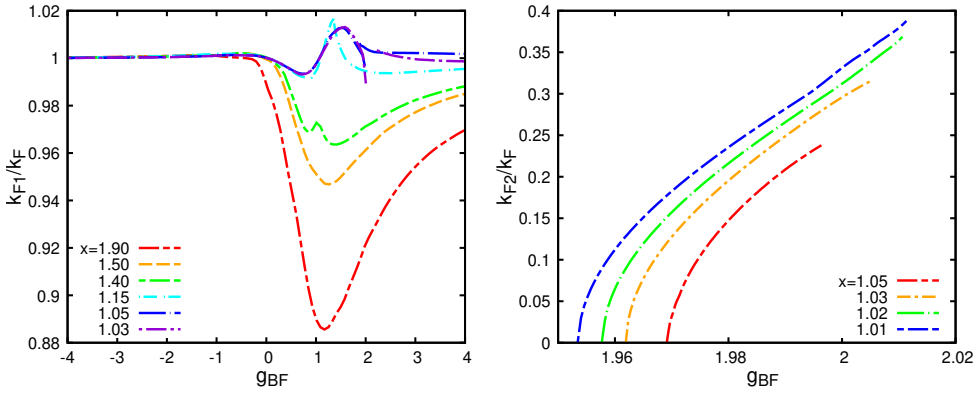

Figure 5.23: Fermi momenta of $G_{\rm F}$ for various values of $x > 1$, and $\eta = 3 \times 10^{-3}$. In the left panel the first Fermi momentum $k_{\rm F1} > P_\Gamma^0$ appears for all values of $x > 1.0$ studied, while in the right panel the second momentum $k_{\rm F2} < P_\Gamma^0$ is present only for $x \leq 1.05$ and above a certain value of the BF coupling.

the right panel of Fig. 5.23 for the values of x and $g_{\rm BF}$ at which it appears.

As a final remark to this section, we wish to comment on the meaning of the different Fermi momenta we have just discussed. The Fermi momenta of $G_{\rm F}$ have a clear meaning as they are associated with Fermi steps in the fermionic momentum distribution $n_{\rm F}(k)$. Any departure of the value of the Fermi momentum $k_{\rm F1}$ from $k_{\rm F}$ (and, even more, the presence of the second Fermi momentum $k_{\rm F2}$) signals deviations from Fermi liquid behaviour for the Fermi component (as a result of pairing correlations with bosons). This non-conventional behaviour could in principle be observed experimentally by measuring the Fermi momentum distribution.

The interpretation of the Fermi momenta $P_{\rm T1}^0$, $P_{\rm T2}^0$ and P_Γ^0 is less clear-cut. The momentum P_Γ^0 is associated with an internal building block of the theory (the Γ-matrix) which only for mixtures with $x \leq 1$ acquires the meaning of the propagator of molecules in the strong-coupling limit. Its knowledge is however useful to determine the Fermi momenta of $G_{\rm F}$, as for $k = P_\Gamma^0$ (and $n_0 \neq 0$) $\mathrm{Re}\, G_{\rm F}(k,0)^{-1}$ diverges, and thus has to be taken into account when solving the equation $\mathrm{Re}\, G_{\rm F}(k,0)^{-1} = 0$. In Ref. [30] the momentum $P_{\rm T2}^0$ was tentatively interpreted as the Fermi momentum of molecules, which are forming for sufficiently strong coupling. This interpretation is rebut by our results for $x > 1$, since $P_{\rm T2}^0$ is different from zero only in a very narrow region of concentrations and couplings. The momentum $P_{\rm T1}^0$, on the other hand, tends to $k_{\rm F}$ in both the weak-coupling limit and strong-coupling limit. Since T is a two-particle (one boson and one fermion) Green's function, we interpret $P_{\rm T1}^0$ differently in the two limits. In weak-

coupling it reflects the Fermi momentum of unpaired fermions (corresponding to the propagation of one essentially free fermion plus a condensate boson). In the strong-coupling limit it corresponds instead to the Fermi momentum of molecules that, in mixtures with $x > 1$, have density $n_{\rm M} = n_{\rm F}$ since all fermions will be bound into molecules in this limit, and thus $P^0_{\rm T1} = k_{\rm F}$ again.

We finally stress that, independently from their interpretation, the determination of all these Fermi momenta is crucial in the numerical algorithm as they are used to construct efficient grid of integration.

5.4 Mechanical Stability

The mechanical stability of Bose-Fermi mixtures has been studied both from a theoretical and experimental point of view over the last years. Ref. [57] has shown that the stability of a degenerate mixture ^{40}K-^{87}Rb is strongly influenced by BF interaction. A sudden disappearance of ^{40}K atoms from the trap was observed when the number of particles (for both bosons and fermions) exceeded certain critical values. Quite generally, the mechanical stability of a BF mixture requires the 2×2 compressibility matrix $\mathcal{M}$

$$\mathcal{M} = \begin{pmatrix} \dfrac{\partial \mu_{\rm F}}{\partial n_{\rm F}} & \dfrac{\partial \mu_{\rm F}}{\partial n_{\rm B}} \\ \dfrac{\partial \mu_{\rm B}}{\partial n_{\rm F}} & \dfrac{\partial \mu_{\rm B}}{\partial n_{\rm B}} \end{pmatrix} \tag{5.13}$$

to be positive definite. Physically, when the compressibility matrix becomes negative definite, the mixture becomes unstable towards a mechanical collapse and cannot exist any longer as a uniform phase (even as a metastable phase). In the first theoretical studies, the stability of a BF mixture was analysed using perturbation theory [33,58]. In particular, in those works the stability of mixtures with bosons and fermions fully mixed was treated using a mean-field approximation introducing an effective fermion-fermion interaction mediated by bosons. The mean-field internal energy of the system is given by

$$E/V = \frac{3}{5} E_{\rm F} n_{\rm F} + \frac{2\pi a_{\rm BB}}{m_{\rm B}} n_{\rm B}^2 + \frac{2\pi a_{\rm BF}}{m_r} n_{\rm B} n_{\rm F} \tag{5.14}$$

where the first term represents the kinetic energy of fermions, while the last two terms represent the mean-field interaction energy between bosons and between

bosons and fermions, respectively. The bosonic and fermionic chemical potentials can be found by differentiating Eq. (5.14) with respect $n_{\rm B}$ and $n_{\rm F}$. In order to have the compressibility matrix positive definite, it is sufficient to require that $\mathrm{Det}(\mathcal{M}) > 0$ and $\mathrm{Tr}(\mathcal{M}) > 0$. In this mean-field case the trace of $\mathcal{M}$ is always positive for positive values of $a_{\rm BB}$, then the stability condition can be expressed by requiring that the dimensionless BB coupling $\zeta = k_{\rm F} a_{\rm BB}$ satisfies

$$\zeta \geq \frac{(m_{\rm B} + m_{\rm F})^2}{2\pi m_{\rm B} m_{\rm F}} \frac{1}{g_{\rm BF}^2}. \tag{5.15}$$

The problem of the mechanical stability in presence of a BF Fano-Feshbach resonance was firstly approached in Ref. [34] using a Jastrow-Slater variational wave function and the lowest-order constrained variational (LOCV) approximation in the limit $x \ll 1$. This study followed the first experimental investigations of resonant ^{40}K - ^{87}Rb interacting mixtures [59–62]. In the limit $x \ll 1$, with a small quantity of bosons with respect to the number of fermions, the BB interaction can be studied as a perturbation with respect to the kinetic energies and the BF interaction part. The total energy density of the mixture can be written in terms of the condensate depletion $n'_{\rm B}/n_{\rm B}$ and the polaron binding energy $A_p E_{\rm F}$ as

$$E/V = \frac{3}{5} n_{\rm F} E_{\rm F} + \frac{2\pi a_{\rm BB}}{m_{\rm B}} n_{\rm B}^2 \left[1 + 4\frac{n'_{\rm B}}{n_{\rm B}}\right] + \frac{m_{\rm B} + m_{\rm F}}{2m_{\rm B}} n_{\rm B} A_p E_{\rm F}. \tag{5.16}$$

The polaron binding energy which appears in Eq. (5.16) is the one for a system with $m_{\rm B} = m_{\rm F}$. The modification of this contribution for $m_{\rm B} \neq m_{\rm F}$ are taken into account by the multiplicative prefactor $(m_{\rm B} + m_{\rm F})/2m_{\rm B}$, within the LOCV approximation. We recall that the polaron binding energy is defined for the problem of a single mobile impurity added to a single-component ideal Fermi gas as

$$A_p = \frac{E(N_{\rm F}, 1 \text{ impurity}) - E(N_{\rm F})}{E_{\rm F}} \tag{5.17}$$

where $E(N_{\rm F})$ is the ground-state energy of the ideal Fermi gas with $N_{\rm F}$ fermions, and $E(N_{\rm F}, 1 \text{ impurity})$ is the ground-state energy of the system with an impurity added (which interacts with the Fermi gas). The polaron binding energy is defined in the thermodynamic limit ($N_{\rm F}$, $V \to \infty$, with $n_{\rm F} = N_{\rm F}/V$ constant).

In Ref. [34] the values of the condensate depletion and the polaron binding energy were reported as functions of $g_{\rm BF}$. Differentiating Eq. (5.16) with respect

$n_{\rm B}$ and $n_{\rm F}$ one can find the expression for the critical value of ζ above which $\mathcal{M}$ has positive determinant and eigenvalues:

$$\zeta_{\rm c} = \frac{\pi\left(1+\frac{m_{\rm B}}{m_{\rm F}}\right)^2}{32\frac{m_{\rm B}}{m_{\rm F}}\left(1+4\frac{n'_{\rm B}}{n_{\rm B}}\right)}\left[2A_p - g_{\rm BF}\frac{\partial A_p}{\partial g_{\rm BF}}\right]^2. \tag{5.18}$$

The values of $\zeta > \zeta_{\rm c}$ are those that make the BF mixture stable.

In order to investigate the mechanical stability with our formalism, in this work I will present stability curves obtained numerically with TMA. In particular, I have evaluated numerically the compressibility matrix in Eq. (5.13) by slightly changing $n_{\rm B}$ and $n_{\rm F}$ one at a time. Then I have obtained the new values for the chemical potentials by solving Eqs. (3.36 - 3.38) with these new values of densities. The curve $\zeta_{\rm c}$ vs $g_{\rm BF}$ obtained in this way for a BF mixture with $x = 0.175$ and mass ratio $m_{\rm B}/m_{\rm F} = 1.0$ is reported in Fig. 5.24, where we also report the stability curve presented in Ref. [34]. The agreement between the two results is good only

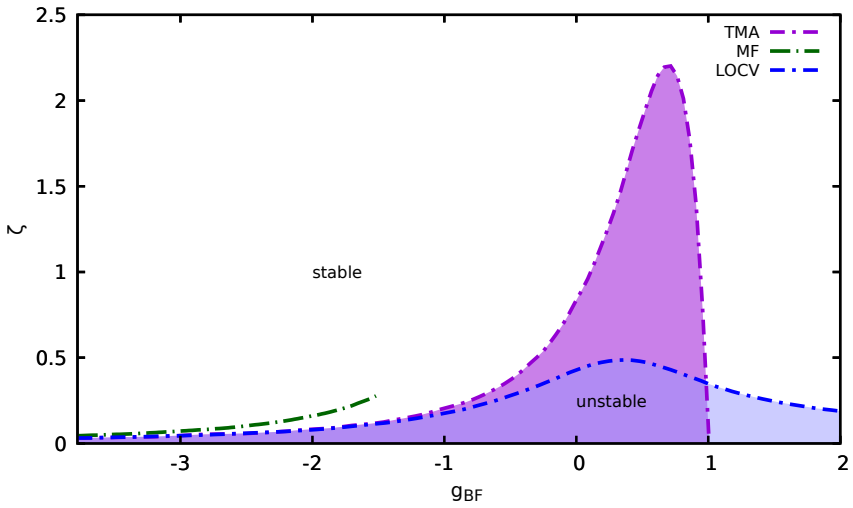

Figure 5.24: Stability diagram obtained numerically with a T-matrix approximation with $x = 0.175$ and $m_{\rm B}/m_{\rm F} = 1.0$ compared with the result reported in Ref. [34], got with LOCV approximation in the polaronic limit.

in the weak-coupling limit, while for $g_{\rm BF} \sim -1.0$ the two curves start to deviate, with a large disagreement for $0 \lesssim g_{\rm BF} \lesssim 0.6$. The BB repulsion required by TMA to ensure the stability near unitarity is much higher than the prediction by LOCV.

Even though the results obtained by LOCV are not exact, it should be mentioned that FNDMC simulations [22] have shown that, for $m_{\rm B} = m_{\rm F}$, the mixture is certainly stable across the whole resonance for $\zeta \geq 1$ (for all $x \leq 1$). We thus

conclude that the value of ζ_c obtained by TMA is too large in the region about unitarity. We believe that the origin of this problem is in the use of the Bogoliubov approximation to include BB repulsion. This approximation is well justified when the condensate depletion is small. This condition is verified when the BF coupling is weak, but ceases to be valid for $g_{BF} \gtrsim -1$, when the increasing of the BF correlations deplete the condensate (even when the BB repulsion is weak).

The treatment of the BB repulsion can be improved by replacing the Bogoliubov approximation with the so-called Popov approximation [32]. In this approximation, the contribution Σ_{11} to the normal bosonic self-energy due to the interaction between the bosons is given by $\Sigma_{11} = 8\pi a_{BB} n_B/m_B$ (instead of $\Sigma_{11} = 8\pi a_{BB} n_0/m_B$ of the Bogoliubov theory). The anomalous self-energy is instead not changed and thus remains given by $\Sigma_{12} = 4\pi a_{BB} n_0/m_B$.

Before moving to the new stability curve, I have repeated all the numerical calculations performed for all values of x and mass ratio $m_B/m_F = 0.575$ using this modification to the bosonic self-energy. In Fig. 5.25 the condensate fraction n_0/n_B vs g_{BF} using a BB repulsion given by the mean-field Popov (Pop) term $8\pi a_{BB} n_B/m_B$ is compared with the corresponding condensate fraction obtained using a mean-field BB repulsion given by the Bogoliubov (Bog) term $8\pi a_{BB} n_0/m_B$. We see that the modification of the bosonic self-energy by Popov's theory intro-

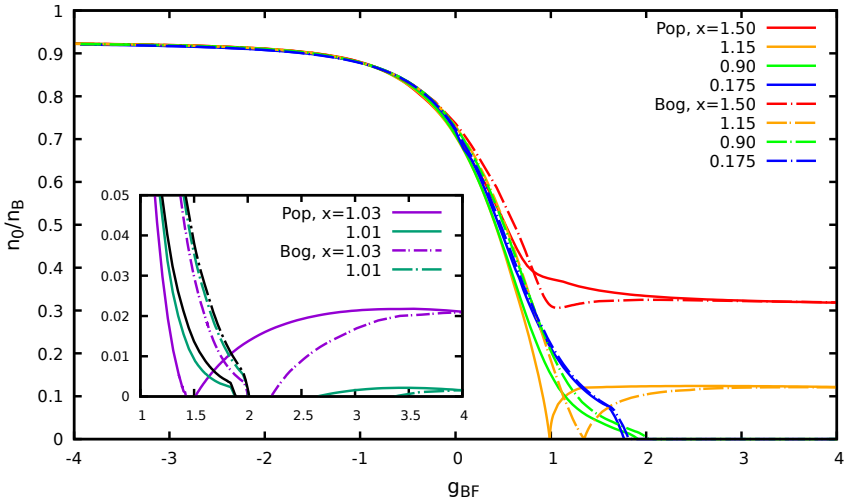

Figure 5.25: Condensate fractions n_0/n_B vs g_{BF} for various values of x and $\eta = 3 \times 10^{-3}$. The full lines represent the condensate fractions obtained using a mean-field BB repulsion given by the Popov term $8\pi a_{BB} n_B/m_B$, while dash-dotted lines show the results obtained with a BB repulsive interaction given by the mean-field Bogoliubov term $8\pi a_{BB} n_0/m_B$. In the inset the comparison is shown for values of x just above 1, where there are no solutions for $n_0 \neq 0$ in a certain range of BF pairing for both theories. The black lines represent the solutions found for $x = 1$.

duces only some quantitative changes on the curve of n_0. These changes are really minor for $x \lesssim 1$; for $x > 1$ they are more significant (in particular the inclusion of the Popov term shifts the vanishing of n_0 to smaller values of $g_{\rm BF}$ in the region $1 < x \leq 1.3$, but the qualitative behaviour of the curve remains exactly the same).

The comparison of the chemical potentials for the minority species is reported in Fig 5.27, while the chemical potentials for the majority species are compared in Fig. 5.26. Also for $\mu_{\rm B}$ and $\mu_{\rm F}$ the changes introduced by the Popov self-energy are only quantitative and more important for $x > 1$.

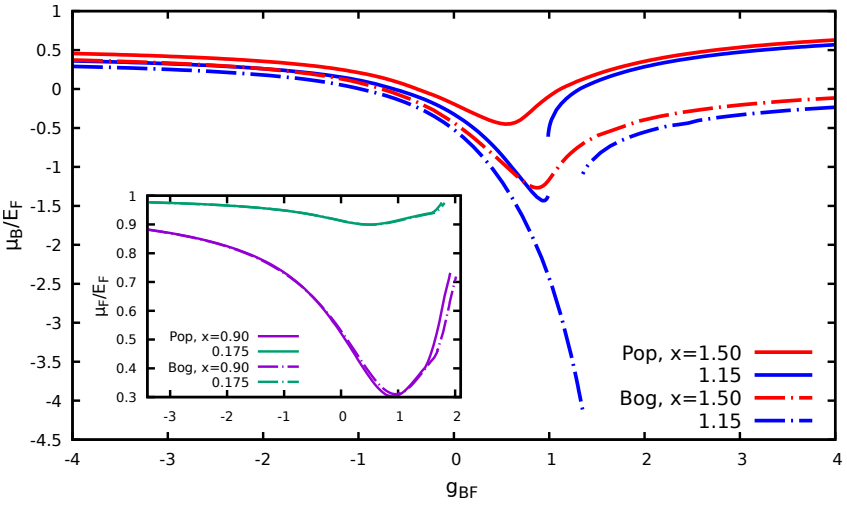

Figure 5.26: Comparison between bosonic chemical potentials (for $x > 1$) vs $g_{\rm BF}$ using a BB repulsion given by the Popov term (full lines) and the corresponding values obtained with a BB repulsion given by the Bogoliubov mean-field term. In the inset ($x < 1$) the comparison is shown for the fermionic chemical potential.

In Fig. 5.28 the stability curve presented in [34] is compared with that obtained using our new TMA formalism for a mass ratio $m_{\rm B}/m_{\rm F} = 1.0$ and $x = 0.175$. We see that the modifications to the compressibility matrix introduced by Popov's theory for the BB repulsion change drastically the stability curve for $g_{\rm BF} \gtrsim -1$. In particular, the new curve is much closer to the curve obtained by LOCV in the region about unitarity. For $g_{\rm BF} \gtrsim 1$, the TMA curves obtained with Bogoliubov or Popov approximation rapidly go to zero, implying a stable mixture even in the absence of BB repulsion. Physically, this behaviour can be explained by the fact that, in this limit, the mixture effectively reduces to a FF mixture, with a small repulsion between unpaired fermions and molecules, which is known to be stable. The LOCV stability curve does not capture this behaviour because, as mentioned in Ref. [34], is based on a variational wave-function which is not longer valid in the molecular limit.

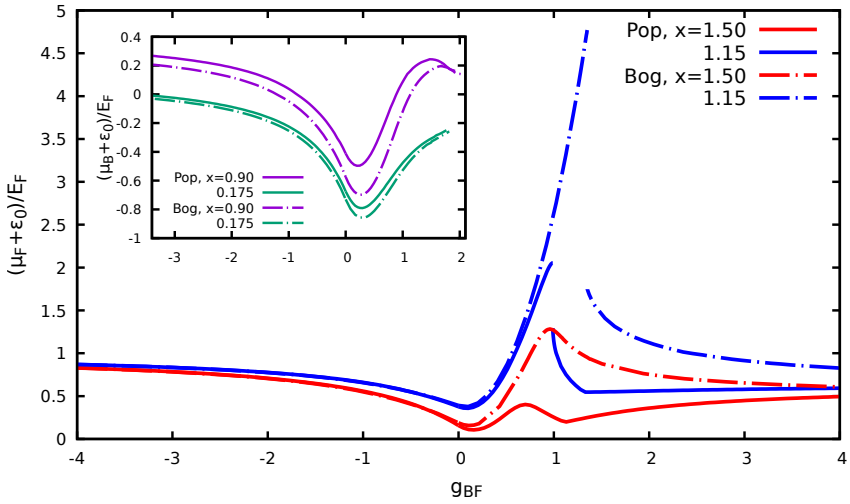

Figure 5.27: Comparison between fermionic chemical potentials minus the binding energy for positive values of g_{BF} (for $x > 1$) vs g_{BF} using a BB repulsion given by the Popov term (full lines) and the corresponding values obtained with a BB repulsion given by the Bogoliubov mean-field term. In the inset (for $x < 1$) the comparison is shown for the bosonic chemical potentials minus the binding energy for $g_{\mathrm{BF}} > 0$.

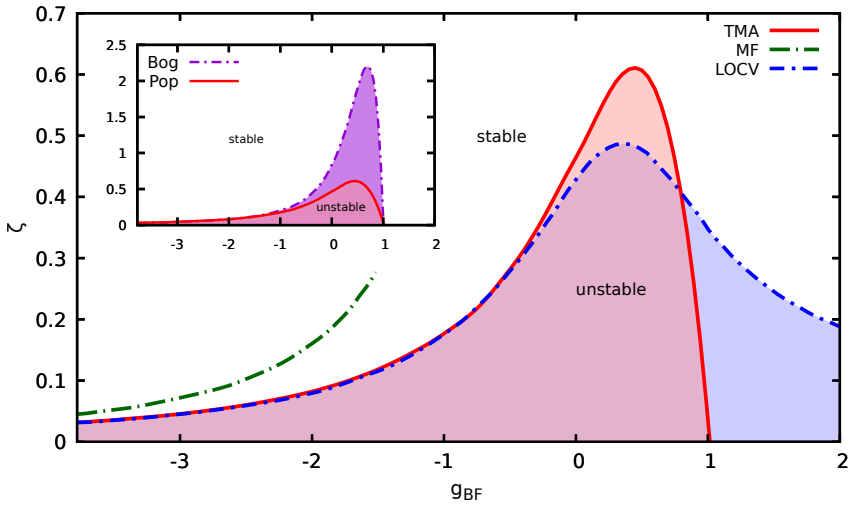

Figure 5.28: Stability diagram in ζ vs g_{BF} plane for $x \ll 1$ and $m_{\mathrm{B}}/m_{\mathrm{F}} = 1.0$. The regions under the curves are those where the system is unstable against mechanical collapse. The blue dash-dotted line represents the critical condition given in Eq. (5.18) using LOCV approximation in the limit $x \to 0$. The full red curve has been obtained for $x = 0.175$ imposing the matrix in Eq. (5.13) to have positive determinant and positive eigenvalues, using μ_{B} and μ_{F} obtained numerically with TMA + Popov's theory for BB repulsion. The green dash-dotted line represents the stability condition in weak-coupling limit using a mean-field approximation. In the inset the results obtained with TMA + Bogoliubov approximation are compared with those obtained with TMA + Popov approximation.

In Figs. 5.29 and 5.30 the stability curves obtained numerically with our TMA + Popov formalism are presented for different mass ratios and two different concentrations ($x = 0.175$ and 0.9). The mass ratios $m_B/m_F = 0.57$, 2.18, and 6.83 correspond to the cases of ^{23}Na - ^{40}K, ^{40}K - ^{87}Rb, and ^{6}Li - ^{41}K mixtures, respectively. In both figures, the stability condition depends weakly on the mass ratio

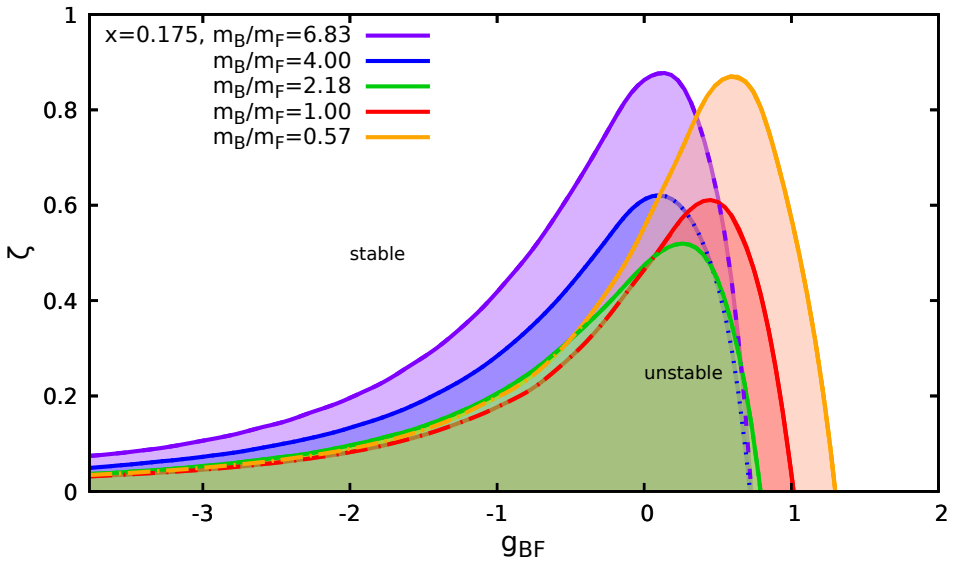

Figure 5.29: Stability diagram using TMA + Popov approximation with $x = 0.175$ for different values of mass ratios.

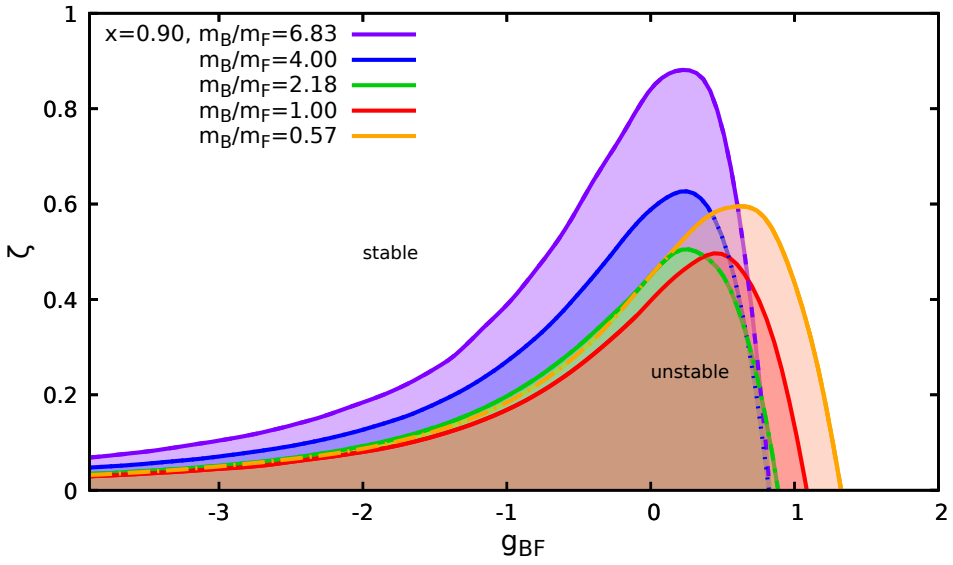

Figure 5.30: Stability diagram using TMA + Popov approximation with $x = 0.9$ for different values of mass ratios.

in the weak-coupling limit for $m_B/m_F \leq 2.18$, while for the larger mass ratios

considered the critical value ζ_c moves to higher values in the weak-coupling limit. In the range of BF coupling between unitarity and the strong-coupling limit ζ_c has a maximum for all values of x and m_B/m_F considered. The position of the maximum moves to smaller values of g_{BF} when m_B/m_F becomes larger, setting around unitarity for $m_B/m_F \gg 1$. For higher values of g_{BF}, the stability curves in Figs. 5.29 and 5.30 rapidly fall toward negative values of ζ_c for all mass ratios for the reason explained above. The BF coupling above which the mixture is stable even without BB repulsion becomes higher when $m_B/m_F \to 0$. Figs. 5.29 and 5.30 thus suggest that in the strong-coupling limit a BB repulsion is no longer necessary to ensure the mechanical stability of the mixture.

Finally, Fig. 5.31 presents the value ζ_c vs m_B/m_F at unitarity, for $x = 0.175$ and 0.9. In both cases, a minimum occurs for $m_B/m_F \sim 1$. In the two extremal regions, when $m_B/m_F \ll 1$ or $m_B/m_F \gg 1$, the critical value ζ_c assumes higher values, with a more rapid increase in the limit $m_B/m_F \to 0$. We thus conclude that isotopic mixtures are the most stable ones at unitarity.

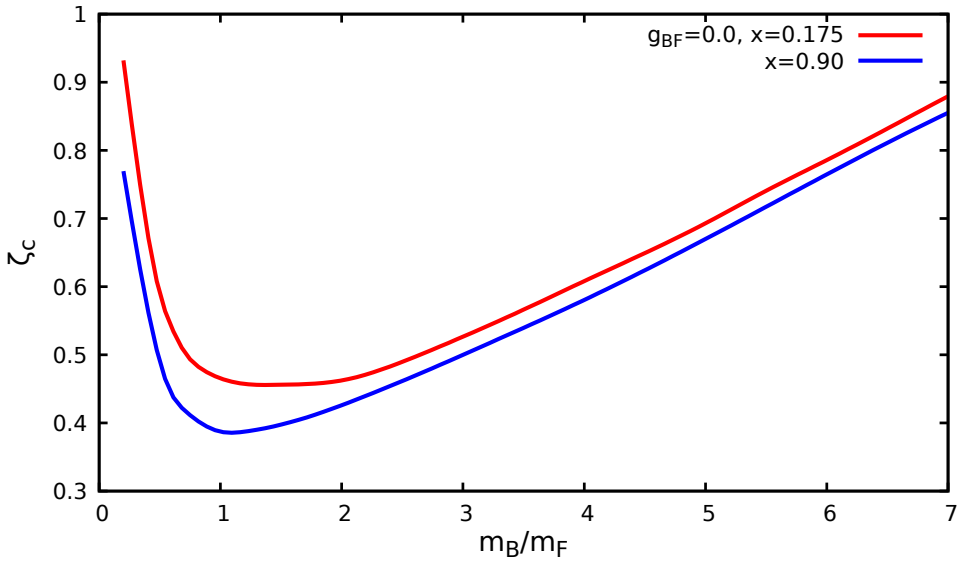

Figure 5.31: Critical value ζ_c vs mass ratio m_B/m_F for two values of x and for a BF coupling fixed at $g_{BF} = 0$.

5.5 Mixture in harmonic trap

In this last section I will present the numerical results for the bosonic and fermionic density profiles obtained for a BF mixture confined in a harmonic trap within a local density approximation.

A dilute and interacting bosons gas confined in a harmonic potential can be described by the Gross–Pitaevskii equation. An analytic solution of the Gross–Pitaevskii equation can be found by neglecting the kinetic term, which is small with respect to the interaction energy when the number of particles in the system is large. This is the so called "Thomas–Fermi" approximation. In this approximation, the local density is given by

$$n_{\mathrm{B}}(r) = \frac{m_{\mathrm{B}}}{4\pi a_{\mathrm{BB}}} \left[\mu_{\mathrm{B}} - V_{\mathrm{B}}(r)\right] \tag{5.19}$$

for $\mu_{\mathrm{B}} - V_{\mathrm{B}}(r) > 0$, while $n_{\mathrm{B}}(r)$ is identically zero when the term inside the square brackets is negative. In the last equation μ_{B} is the bosonic chemical potential at the center of the trap and $V_{\mathrm{B}}(r)$ is the harmonic trapping potential. The density distribution for a trapped cloud of non-interacting fermions in its ground state can be obtained by using the Thomas–Fermi approximation (see, e.g. [48]). In this case the fermionic gas at the point r in the trap is treated as a uniform fermionic gas with a density equal to the local density $n_{\mathrm{F}}(r)$. The density profile is given by

$$n_{\mathrm{F}}(r) = \frac{1}{6\pi^2} \left\{ \frac{2m_{\mathrm{F}}}{\hbar} \left[\mu_{\mathrm{F}} - V_{\mathrm{F}}(r)\right] \right\}^{3/2} \tag{5.20}$$

when $\mu_{\mathrm{F}} - V_{\mathrm{F}}(r) > 0$, and it is equal to zero otherwise. In Eq. (5.20) μ_{F} is the fermionic chemical potential at the center of the trap and $V_{\mathrm{F}}(r)$ is the harmonic trapping potential. This approximation is valid provided the local Fermi wavelength $2\pi/k_{\mathrm{F}}(r)$ is small compared with the spatial dimension of the cloud of fermions.

In order to study a BF interacting mixture confined in an isotropic harmonic trap we extend the local density approximation to our model. The bosonic and fermionic chemical potentials as functions of r are set to be

$$\mu_{\mathrm{B}}(r) = \mu_{\mathrm{B}}^{\star} - \frac{1}{2} m_{\mathrm{B}} \omega_{\mathrm{B}}^2 r^2 \tag{5.21}$$

$$\mu_{\mathrm{F}}(r) = \mu_{\mathrm{F}}^{\star} - \frac{1}{2} m_{\mathrm{F}} \omega_{\mathrm{F}}^2 r^2 \tag{5.22}$$

where $\mu_{\mathrm{B}}^{\star}$ and $\mu_{\mathrm{F}}^{\star}$ are the chemicals potentials at the center of the trap, and they are given by the numerical values obtained for a non-trapped homogeneous system for a certain mass ratio, density imbalance and for certain values of BF and BB couplings. ω_{B} and ω_{F} in Eqs. (5.21) and (5.22) are the harmonic frequencies of

confinement. Bosonic and fermionic local densities are given by

$$n_{\mathrm{B}}(r) = n_0(r) - \int \frac{d\mathbf{k}}{(2\pi)^3} \int \frac{d\omega}{2\pi} G_{\mathrm{B}}\Big(\mathbf{k}, \omega \Big| \mu_{\mathrm{B}}(r), \mu_{\mathrm{F}}(r), n_0(r)\Big) \tag{5.23}$$

$$n_{\mathrm{F}}(r) = \int \frac{d\mathbf{k}}{(2\pi)^3} \int \frac{d\omega}{2\pi} G_{\mathrm{F}}\Big(\mathbf{k}, \omega \Big| \mu_{\mathrm{B}}(r), \mu_{\mathrm{F}}(r), n_0(r)\Big) \tag{5.24}$$

where G_{B} and G_{F} are given by Eqs. (3.32) and (3.33) with the self-energies and free dispersion relations calculated with local values of $\mu_{\mathrm{B}}(r)$ and $\mu_{\mathrm{F}}(r)$ in Eqs. (5.21) and (5.22). In order to ensure the mechanical stability of the system, the bosonic self-energy includes a Popov mean-field interaction term between bosons. $n_0(r)$ is a function of $\mu_{\mathrm{B}}(r)$, $\mu_{\mathrm{F}}(r)$, $n_{\mathrm{B}}(r)$ and it is found locally using the Hugenholtz-Pines relation

$$\mu_{\mathrm{B}}(r) = \frac{8\pi a_{\mathrm{BB}} n_{\mathrm{B}}(r)}{m_{\mathrm{B}}} + \Sigma_{\mathrm{BF}}\Big(\mathbf{0}, 0 \Big| \mu_{\mathrm{B}}(r), \mu_{\mathrm{F}}(r), n_0(r)\Big) - \frac{4\pi a_{\mathrm{BB}} n_0(r)}{m_{\mathrm{B}}}. \tag{5.25}$$

For each value of r, the system of Eqs. (5.23 - 5.25) gives the local density of bosons, fermions and condensed bosons, respectively, for $\mu_{\mathrm{B}}^{\star}$ and $\mu_{\mathrm{F}}^{\star}$ at the center of the isotropic trap. The strategy adopted for the numerical solutions of the system is as follows. In the first step, starting from the center of the trap ($r = 0$) with $\mu_{\mathrm{B}}^{\star}$ and $\mu_{\mathrm{F}}^{\star}$, one moves away to a small value of $r = \delta r > 0$ where the local chemical potentials are given by Eqs.(5.21) and (5.22). The condensate density $n_0(r)$ is found by solving Eq. (5.25) with a bisection method using as total boson density $n_{\mathrm{B}}(r)$ in the first term of Eq. (5.25) a trial value given by $n_{\mathrm{B}}(r - \delta r)$, corresponding to the boson density obtained in the previous step. With this first value of $n_0(r)$, a new value of $n_{\mathrm{B}}(r)$ can be calculated using Eq. (5.23). This new value of $n_{\mathrm{B}}(r)$ is used to compute with Eq. (5.25) the local condensate density. The process is iterated until the difference (in absolute value) between the bosons local density calculated at the iteration j and the one calculated at the iteration $j + 1$ is smaller than a certain quantity δn_{B}, which has been fixed to 1×10^{-5}. At this point the corresponding value of $n_0(r)$ is used to compute $n_{\mathrm{F}}(r)$ with Eq. (5.24).

The starting values $\mu_{\mathrm{B}}^{\star}$ and $\mu_{\mathrm{F}}^{\star}$ are those obtained solving the system of Eqs. (3.36 - 3.38) with a density ratio $n_{\mathrm{B}}/n_{\mathrm{F}} = 0.9$ at the center of the trap, a mass ratio $m_{\mathrm{B}}/m_{\mathrm{F}} = 0.57$ and various combinations of g_{BF} and ζ such that the mechanical stability against collapse reported in Fig. 5.30 for $m_{\mathrm{B}}/m_{\mathrm{F}} = 0.57$ is fulfilled.

The trap frequencies have been fixed to $\omega_B/\omega_F = 1/3$ in order to reproduce the experimental conditions of Ref. [29] where an anisotropic harmonic trap was used to study a BF interacting mixture with ratio $\overline{\omega}_B/\overline{\omega}_F = 1/3$, where $\overline{\omega}_B = \left(\omega_x^B \omega_y^B \omega_z^B\right)^{1/3}$ and $\overline{\omega}_F = \left(\omega_x^F \omega_y^F \omega_z^F\right)^{1/3}$. The density profiles at unitarity ($g_{BF} = 0$) obtained numerically are reported in Fig. 5.32. Starting from the density for a homogeneous

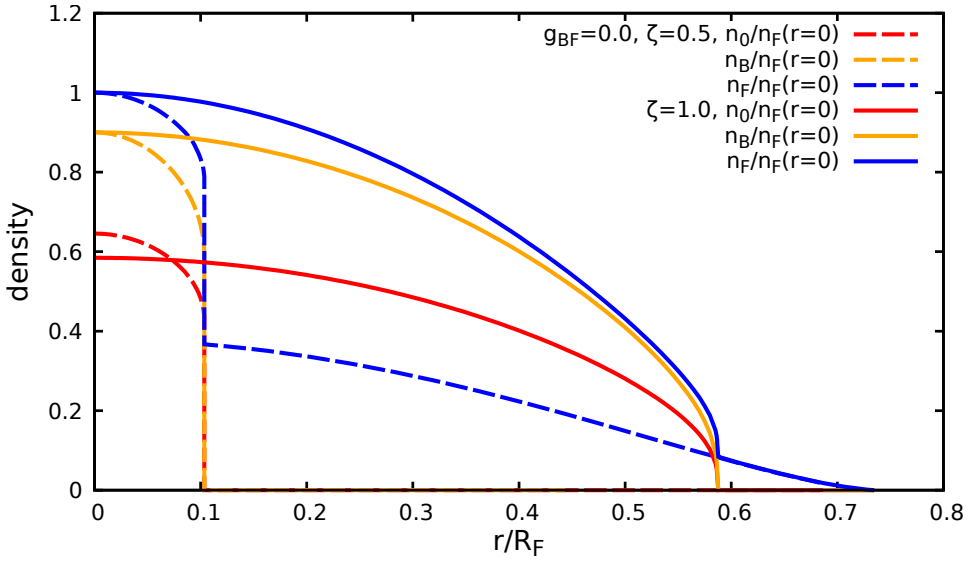

Figure 5.32: Densities profiles obtained numerically starting from a density ratio $x = 0.9$ at the center of the trap. Densities are in units of $n_F(0)$, while r is in units of R_F, with $R_F = \sqrt{2E_F(0)/(m_F\omega_F^2)}$, where $E_F(0) = (6\pi^2 n_F(0))^{2/3}/2m_F$ is the Fermi energy at the center of the trap. We set the mass ratio $m_B/m_F = 0.575$ and $\omega_B/\omega_F = 1/3$, as in the experiment [29].

system at the center of the trap, the densities decrease with r. As one can see from Fig. 5.32 the profiles are strongly influenced by the BB repulsion term when the same densities are enforced at the center of the trap, as in our calculation. Following the profiles, at a certain value of r they experience a jump: $n_B(r)$ and $n_0(r)$ go to zero while $n_F(r)$ starts to follow the Thomas-Fermi profile, given in Eq. (5.20), for a non-interacting Fermi gas.

The local values of x and ζ just before the jump are $x(r_{JUMP}^-) = 0.76$ and $\zeta(r_{JUMP}^-) = 0.46$ for $\zeta = 0.5$ at the center of the trap, and $x(r_{JUMP}^-) = 0.43$ and $\zeta(r_{JUMP}^-) = 0.49$ for $\zeta = 1.0$. On the other hand, from our previous calculations for the homogeneous system, we know that the mixture is certainly unstable for $\zeta < \zeta_c = 0.465$ for $x = 0.175$, and $\zeta < \zeta_c = 0.443$ for $x = 0.9$. A linear interpolation of these two results yields $\zeta_c = 0.457$ and $\zeta_c = 0.447$ for $x = 0.43$ and 0.76, respectively. We thus see that the jump (which corresponds to phase separation) occurs when the local value of ζ is approaching the critical value ζ_c, avoiding in this way the mechanical instability.

The total numbers of particles in the trap are given by the integrals over three-dimensional space of densities in Eqs. (5.23), (5.24), and $n_0(r)$ which can be obtained from Eq. (5.25). The total fraction of condensate $N_0/N_{\rm B}$ obtained numerically is similar to $n_0(0)/n_{\rm B}(0)$ at the center of the trap for both values of ζ considered. In particular, for $\zeta = 0.5$ we got $N_0/N_{\rm B} = 0.721$ compared with $n_0(0)/n_{\rm B}(0) = 0.717$ at the center, while for $\zeta = 1.0$ we obtain $N_0/N_{\rm B} = 0.673$ and $n_0(0)/n_{\rm B}(0) = 0.650$ at the center. This finding is important because it confirms the validity of the comparison made in Ref. [29] between the condensate fraction $N_0/N_{\rm B}$ integrated over the trap and the corresponding results obtained in Ref. [26] for a uniform system. Specifically, the comparison is made with a uniform system with couplings $g_{\rm BF}$ and concentration $n_{\rm B}/n_{\rm F}$ equal to the local values $(k_{\rm F}(0)a_{\rm BF})^{-1}$ and $n_{\rm B}(0)/n_{\rm F}(0)$ at the center of the trapped system. The integration over the trap of $n_{\rm F}(r)$ allows us to determine the ratio between the trap Fermi energy $E_{\rm F}^{\rm TRAP} = (6N_{\rm F})^{1/3}\omega_{\rm F}$ and the local Fermi energy $E_{\rm F}(0)$ which we have used in the normalization of Fig. 5.32. By defining $\tilde{r} = \frac{r}{R_{\rm F}}$, $\tilde{n}(r) = \frac{n(r)}{n(0)}$, with $E_{\rm F}(0) = \frac{1}{2}m_{\rm F}\omega_{\rm F}^2 R_{\rm F}^2$, one has

$$\frac{E_{\rm F}^{\rm TRAP}}{E_{\rm F}(0)} = \left[\frac{8}{\pi^2}\int d^3\tilde{r}\;\tilde{n}_{\rm F}(\tilde{r})\right]^{1/3}. \tag{5.26}$$

For the two cases of Fig. 5.32 we have $\frac{E_{\rm F}^{\rm TRAP}}{E_{\rm F}(0)} = 0.401$ and 0.579 for $\zeta = 0.5$ and 1, respectively.

Finally in Fig. 5.33 our numerical results for $n_0/n_{\rm B}$ obtained for densities ratios $x = 0.9$ (first panel) and $x = 1.3$ (second panel) are compared to the experimental results found in Ref. [29] for a BF interacting mixture confined in a harmonic trap, with the same values $x = 0.9$ and $x = 1.3$ at the trap center. Our numerical results agree well with the experimental data throughout almost the entire interaction regime given by $g_{\rm BF} = (a_{\rm BF}k_{\rm F})^{-1}$. A similar comparison was already made in the experimental work [29] with the TMA data calculated in Ref. [26] for $n_{\rm B}/n_{\rm F} = 1$ (see Fig. 1.4). The present comparison improves that of Ref. [29] because: *i*) the calculations are made at the exactly same values of x as in the experiment *ii*) a BB repulsion $\eta = 3 \times 10^{-3}$ is added and described within Popov's theory to guarantee the stability of the mixture *iii*) the comparison in made separately for the two values of x considered in the experiment. For the case $x = 0.9$, the present comparison shows an even better agreement with the experimental data compared to Ref. [29]. For $x = 1.3$ the agreement is also very good until n_0 vanishes in the theoretical calculation. The subsequent rise of the

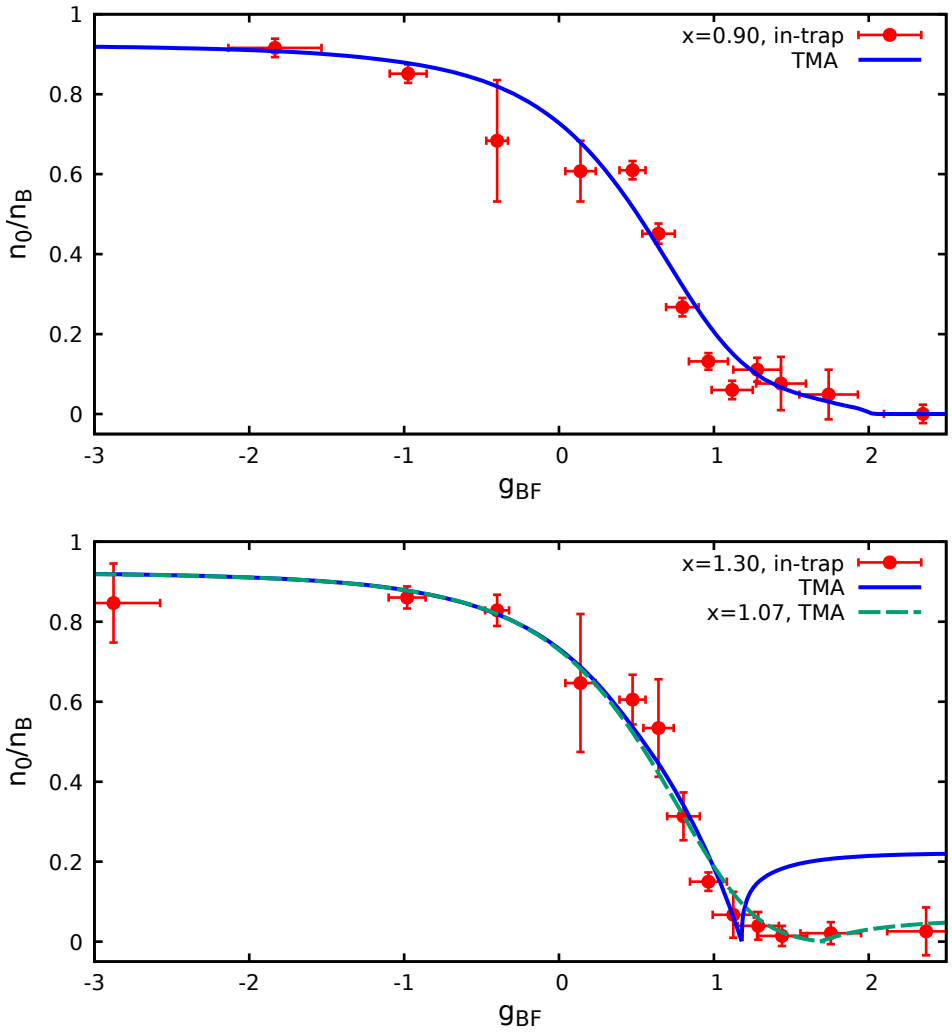

Figure 5.33: Comparison of condensate fraction vs $g_{\rm BF} = (a_{\rm BF} k_{\rm F})^{-1}$ obtained numerically with T-matrix approximation theory at zero temperature (blue lines) and experimental results of Ref. [29]. We have used $\eta = 3 \times 10^{-3}$ in the theoretical calculation. The dashed line in the bottom panel represents the numerical results obtained numerically for $x = 1.07$.

condensate in the theoretical curve (right branch) is definitely larger. Still it is quite interesting that a small residual of the condensate seems to occur also in the experimental data (last three points in the bottom panel of Fig. 5.33). The dashed line represents the theoretical data obtained with a density ratio $n_{\rm B}/n_{\rm F} = 1.07$.

As a final comment on this comparison, we mention that, clearly, the experiment was performed at finite temperature. The effect of temperature was somehow eliminated by experimentalists by removing the thermal bosons in their definition of condensate fraction. In addition, the experimental value of the boson gas parameter was quite small ($\eta \sim 10^{-5}$), with no evidence however of collapse or phase separation (at least in the control region). A possible explanation is that

the time scale for phase-separation or collapse to set in was longer than the time scale for reaching a quasi-stationary state which can be compared with theoretical calculation at equilibrium (with a larger boson repulsion to guarantee stability).

Conclusions

In this master degree thesis I have studied three-dimensional Bose-Fermi mixtures at zero temperature, with BF pairing tuned by a broad Fano-Feshbach resonance. I have used a diagrammatic formalism based on the so-called T-matrix approximation, solved with numerical computations implemented with a Fortran 90 program. I focused mostly on BF mixtures with a mass ratio $m_{\mathrm{B}}/m_{\mathrm{F}} = 23/40$, corresponding to a ^{23}Na-^{40}K gas. I analysed the system from the weak-coupling limit to a strong-coupling limit for different values of concentration $n_{\mathrm{B}}/n_{\mathrm{F}}$, and with a mean-field repulsion between bosons. The main results obtained are:

i) A complete analysis of BF mixtures with a majority of bosons, which were previously analysed only cursorily in Ref. [30]. In particular, I studied BF mixtures from the case of a bosonic number density double with respect to the fermionic density, to the case of a slight majority of bosons. In this last limit, I found a possible (unexpected) quantum phase transition from a condensed to a normal phase, signaled by a complete depletion of the condensate fraction in a certain range of BF coupling.

ii) A possible improvement of the TMA approach with the mean-field repulsion between bosons described by Popov's theory instead of Bogoliubov approximation (the latter was used in previous studies of BF mixtures with a T-matrix approximation). This improvement provides a more accurate description of the BB repulsion in the strong-coupling limit, when the condensate depletion is large. This improvement was motivated by the discrepancy between the results on the mechanical stability obtained numerically with the TMA + Bogoliubov approximation and the results presented in Ref. [22] using FNDMC for isotropic BF mixtures.

iii) A numerical study of the mechanical stability of BF mixtures with different concentrations $n_{\mathrm{B}}/n_{\mathrm{F}}$ and various mass ratios $m_{\mathrm{B}}/m_{\mathrm{F}}$, using the Popov's theory to describe the BB repulsion. The stability curves indicate the amount of BB repulsion required to guarantee the stability of the system as a function of the BF coupling. We have found that the highest BB repulsion for stability is required

slightly above the unitarity limit, while in the the strong BF coupling limit the mixture is stable even in the absence of a BB repulsion.

iv) A first analysis of the effect of the harmonic trapping potential within local density approximation. An important finding for the comparison with the experiment is that the condensate fraction at the center of the trap is very close to the condensate fraction for all bosons in the trap. A second finding is the presence of a jump in the density profiles, which corresponds to the occurrence of phase separation. Phase separation occurs when the local BB repulsion $k_{\rm F}(r_{\rm JUMP})a_{\rm BB}$ is close to the critical value found for a homogeneous mixture.

v) A comparison between the experimental results for the condensate fraction obtained for a double-degenerate trapped BF mixture of ^{23}Na - ^{40}K [29], with the present numerical results obtained with a TMA. The comparison has been made with a BB repulsion described by Popov's theory, and for a homogeneous BF mixtures with BF couplings and density ratios equal to the experimental concentrations at the center of the trap. The good agreement between the theory and the experiments is very encouraging.

This thesis work could be further extended. For example, a more detailed calculations of trapped BF mixtures can be carried out using different BF couplings and different densities ratios. The stabilities curves here presented could be employed in more detailed analysis of BF mixtures with different mass ratios, in particular to study ^{6}Li - ^{41}K mixtures, which were used in some experimental work over the last years. Finally, an implementation of the three-body problem to BF mixtures with a majority of bosons would allows one to explore more extreme cases of density imbalance, with systems formed by a larger majority of bosons.

Bibliography

[1] S. N. Bose, "Plancks gesetz und lichtquantenhypothese", Zeitschrift für Physik **26**, no. 1, pp. 178–181, (1924).

[2] A. Einstein, "Quantentheorie des einatomigen idealen Gases", Sitzungsberichte der Preußischen Akademie der Wissenschaften **1**, p. 3, (1925).

[3] M. H. Anderson, J. R. Ensher, M. R. Matthews, C. E. Wieman, and E. A. Cornell, "Observation of Bose-Einstein condensation in a dilute atomic vapor", Science **269**, no. 5221, pp. 198–201, (1995).

[4] K. B. Davis, M. O. Mewes, M. R. Andrews, N. J. van Druten, D. S. Durfee, D. M. Kurn, and W. Ketterle, "Bose-Einstein Condensation in a Gas of Sodium Atoms", Phys. Rev. Lett. **75**, pp. 3969–3973, (1995).

[5] C. C. Bradley, C. A. Sackett, J. J. Tollett, and R. G. Hulet, "Evidence of Bose-Einstein Condensation in an Atomic Gas with Attractive Interactions", Phys. Rev. Lett. **75**, pp. 1687–1690, (1995).

[6] E. Fermi, "Sulla quantizzazione del gas perfetto monoatomico", Rendiconti Lincei **145**, (1926).

[7] P. A. M. Dirac, "On the theory of quantum mechanics", Proc. Roy. Soc. A **112**, no. 762, pp. 661–677, (1926).

[8] C. Chin, R. Grimm, P. Julienne, and E. Tiesinga, "Feshbach resonances in ultracold gases", Rev. Mod. Phys. **82**, no. 2, p. 1225, (2010).

[9] J. Bardeen, L. N. Cooper, and J. R. Schrieffer, "Theory of Superconductivity", Phys. Rev. **108**, pp. 1175–1204, (1957).

[10] Q. Chen, J. Stajic, S. Tan, and K. Levin, "BCS–BEC crossover: From high temperature superconductors to ultracold superfluids", Phys. Rep. **412**, no. 1, pp. 1–88, (2005).

[11] R. Haussmann, W. Rantner, S. Cerrito, and W. Zwerger, "Thermodynamics of the BCS-BEC crossover", Phys. Rev. A **75**, no. 2, p. 023610, (2007).

[12] W. Ketterle and M. W. Zwierlein, "Making, probing and understanding ultracold Fermi gases", La Rivista del Nuovo Cimento **31**, no. 5, pp. 247–422, (2008).

[13] S. Giorgini, L. P. Pitaevskii, and S. Stringari, "Theory of ultracold atomic Fermi gases", Rev. Mod. Phys. **80**, no. 4, p. 1215, (2008).

[14] W. Zwerger, *The BCS-BEC crossover and the unitary Fermi gas*, vol. 836. Springer Science & Business Media, (2011).

[15] M. Randeria and E. Taylor, "Crossover from Bardeen-Cooper-Schrieffer to Bose-Einstein condensation and the unitary Fermi gas", Annu. Rev. Condens. Matter Phys. **5**, no. 1, pp. 209–232, (2014).

[16] G. C. Strinati, P. Pieri, G. Röpke, P. Schuck, and M. Urban, "The BCS–BEC crossover: From ultra-cold Fermi gases to nuclear systems", Phys. Rep. **738**, pp. 1–76, (2018).

[17] C. Regal, M. Greiner, and D. S. Jin, "Observation of resonance condensation of fermionic atom pairs", Phys. Rev. Lett. **92**, no. 4, p. 040403, (2004).

[18] J. Kinast, S. Hemmer, M. Gehm, A. Turlapov, and J. Thomas, "Evidence for superfluidity in a resonantly interacting Fermi gas", Phys. Rev. Lett. **92**, no. 15, p. 150402, (2004).

[19] T. Bourdel, L. Khaykovich, J. Cubizolles, J. Zhang, F. Chevy, M. Teichmann, L. Tarruell, S. Kokkelmans, and C. Salomon, "Experimental study of the BEC-BCS crossover region in Lithium 6", Phys. Rev. Lett. **93**, no. 5, p. 050401, (2004).

[20] C. Chin, M. Bartenstein, A. Altmeyer, S. Riedl, S. Jochim, J. H. Denschlag, and R. Grimm, "Observation of the pairing gap in a strongly interacting Fermi gas", Science **305**, no. 5687, pp. 1128–1130, (2004).

[21] G. B. Partridge, K. E. Strecker, R. I. Kamar, M. W. Jack, and R. G. Hulet, "Molecular probe of pairing in the BEC-BCS crossover", Phys. Rev. Lett. **95**, no. 2, p. 020404, (2005).

[22] G. Bertaina, E. Fratini, S. Giorgini, and P. Pieri, "Quantum Monte Carlo study of a resonant Bose-Fermi mixture", Phys. Rev. Lett. **110**, no. 11, p. 115303, (2013).

[23] E. Fratini and P. Pieri, "Pairing and condensation in a resonant Bose-Fermi mixture", Phys. Rev. A **81**, p. 051605, (2010).

[24] E. Fratini and P. Pieri, "Mass imbalance effect in resonant Bose-Fermi mixtures", Phys. Rev. A **85**, p. 063618, (2012).

[25] A. Guidini, G. Bertaina, E. Fratini, and P. Pieri, "Bose-Fermi mixtures in the molecular limit", Phys. Rev. A **89**, p. 023634, (2014).

[26] A. Guidini, G. Bertaina, D. E. Galli, and P. Pieri, "Condensed phase of Bose-Fermi mixtures with a pairing interaction", Phys. Rev. A **91**, no. 2, p. 023603, (2015).

[27] A. Perali, P. Pieri, and G. Strinati, "Quantitative comparison between theoretical predictions and experimental results for the BCS-BEC crossover", Phys. Rev. Let. **93**, no. 10, p. 100404, (2004).

[28] P. Pieri, L. Pisani, and G. C. Strinati, "Comparison between a diagrammatic theory for the BCS-BEC crossover and quantum Monte Carlo results", Phys. Rev. B **72**, p. 012506, (2005).

[29] M. Duda, X.-Y. Chen, A. Schindewolf, R. Bause, J. von Milczewski, R. Schmidt, I. Bloch, and X.-Y. Luo, "Transition from a polaronic condensate to a degenerate Fermi gas of heteronuclear molecules", preprint arXiv:2111.04301 (2021).

[30] A. Guidini, *Superconductivity and Superfluidity in Multicomponent Systems*. PhD thesis, Università degli studi di Camerino, (2016).

[31] H. Shi and A. Griffin, "Finite-temperature excitations in a dilute Bose-condensed gas", Phys. Rep. **304**, no. 1-2, pp. 1–87, (1998).

[32] V. N. Popov, *Functional integrals and collective excitations*. Cambridge University Press, (1987).

[33] R. Roth and H. Feldmeier, "Mean-field instability of trapped dilute boson-fermion mixtures", Phys. Rev. A **65**, p. 021603, (2002).

[34] Z.-Q. Yu, S. Zhang, and H. Zhai, "Stability condition of a strongly interacting boson-fermion mixture across an interspecies Feshbach resonance", Phys. Rev. A **83**, p. 041603, (2011).

[35] K. Günter, T. Stöferle, H. Moritz, M. Köhl, and T. Esslinger, "Bose-Fermi mixtures in a three-dimensional optical lattice", Phys. Rev. Lett. **96**, no. 18, p. 180402, (2006).

[36] C. Ospelkaus, S. Ospelkaus, L. Humbert, P. Ernst, K. Sengstock, and K. Bongs, "Ultracold heteronuclear molecules in a 3D optical lattice", Phys. Rev. Lett. **97**, no. 12, p. 120402, (2006).

[37] S. Ospelkaus, C. Ospelkaus, L. Humbert, K. Sengstock, and K. Bongs, "Tuning of heteronuclear interactions in a degenerate Fermi-Bose mixture", Phys. Rev. Lett. **97**, no. 12, p. 120403, (2006).

[38] J. Zirbel, K.-K. Ni, S. Ospelkaus, J. D'Incao, C. Wieman, J. Ye, and D. Jin, "Collisional stability of fermionic Feshbach molecules", Phys. Rev. Lett. **100**, no. 14, p. 143201, (2008).

[39] C.-H. Wu, I. Santiago, J. W. Park, P. Ahmadi, and M. W. Zwierlein, "Strongly interacting isotopic Bose-Fermi mixture immersed in a Fermi sea", Phys. Rev. A **84**, no. 1, p. 011601, (2011).

[40] C.-H. Wu, J. W. Park, P. Ahmadi, S. Will, and M. W. Zwierlein, "Ultracold fermionic Feshbach molecules of ^{23}Na^{40}K", Phys. Rev. Lett. **109**, no. 8, p. 085301, (2012).

[41] M.-J. Zhu, H. Yang, L. Liu, D.-C. Zhang, Y.-X. Liu, J. Nan, J. Rui, B. Zhao, J.-W. Pan, and E. Tiemann, "Feshbach loss spectroscopy in an ultracold ^{23}Na-^{40}K mixture", Phys. Rev. A **96**, no. 6, p. 062705, (2017).

[42] T. D. Cumby, R. A. Shewmon, M.-G. Hu, J. D. Perreault, and D. S. Jin, "Feshbach-molecule formation in a Bose-Fermi mixture", Phys. Rev. A **87**, no. 1, p. 012703, (2013).

[43] R. S. Bloom, M.-G. Hu, T. D. Cumby, and D. S. Jin, "Tests of universal three-body physics in an ultracold Bose-Fermi mixture", Phys. Rev. Lett. **111**, no. 10, p. 105301, (2013).

[44] M.-S. Heo, T. T. Wang, C. A. Christensen, T. M. Rvachov, D. A. Cotta, J.-H. Choi, Y.-R. Lee, and W. Ketterle, "Formation of ultracold fermionic NaLi Feshbach molecules", Phys. Rev. A **86**, no. 2, p. 021602, (2012).

[45] R. Combescot, S. Giraud, and X. Leyronas, "Analytical theory of the dressed bound state in highly polarized Fermi gases", Europhys. Lett. **88**, no. 6, p. 60007, (2010).

[46] J. Vlietinck, J. Ryckebusch, and K. Van Houcke, "Quasiparticle properties of an impurity in a Fermi gas", Phys. Rev. B **87**, no. 11, p. 115133, (2013).

[47] H. T. Stoof, K. B. Gubbels, and D. B. Dickerscheid, *Ultracold quantum fields*, vol. 1. Springer, (2009).

[48] C. J. Pethick and H. Smith, *Bose–Einstein condensation in dilute gases*. Cambridge university press, (2008).

[49] T. Nicholson, S. Blatt, B. Bloom, J. Williams, J. Thomsen, J. Ye, and P. S. Julienne, "Optical Feshbach resonances: Field-dressed theory and comparison with experiments", Phys. Rev. A **92**, no. 2, p. 022709, (2015).

[50] A. Moerdijk, B. Verhaar, and A. Axelsson, "Resonances in ultracold collisions of ^{6}Li, ^{7}Li, and ^{23}Na", Phys. Rev. A **51**, no. 6, p. 4852, (1995).

[51] E. Timmermans, P. Tommasini, M. Hussein, and A. Kerman, "Feshbach resonances in atomic Bose–Einstein condensates", Phys. Rep. **315**, no. 1-3, pp. 199–230, (1999).

[52] A. L. Fetter and J. D. Walecka, *Quantum Theory of Many-Particle Systems*. Boston: McGraw-Hill, (1971).

[53] N. M. Hugenholtz and D. Pines, "Ground-State Energy and Excitation Spectrum of a System of Interacting Bosons", Phys. Rev. **116**, pp. 489–506, (1959).

[54] A. P. Albus, S. A. Gardiner, F. Illuminati, and M. Wilkens, "Quantum field theory of dilute homogeneous Bose-Fermi mixtures at zero temperature: General formalism and beyond mean-field corrections", Phys. Rev. A **65**, p. 053607, (2002).

[55] L. Viverit and S. Giorgini, "Ground-state properties of a dilute Bose-Fermi mixture", Phys. Rev. A **66**, no. 6, p. 063604, (2002).

[56] J. Luttinger, "Fermi surface and some simple equilibrium properties of a system of interacting fermions", Phys. Rev. **119**, no. 4, p. 1153, (1960).

[57] G. Modugno, G. Roati, F. Riboli, F. Ferlaino, R. J. Brecha, and M. Inguscio, "Collapse of a degenerate Fermi gas", Science **297**, no. 5590, pp. 2240–2243, (2002).

[58] L. Viverit, C. J. Pethick, and H. Smith, "Zero-temperature phase diagram of binary boson-fermion mixtures", Phys. Rev. A **61**, (2000).

[59] C. A. Stan, M. W. Zwierlein, C. H. Schunck, S. M. F. Raupach, and W. Ketterle, "Observation of Feshbach Resonances between Two Different Atomic Species", Phys. Rev. Lett. **93**, p. 143001, (2004).

[60] S. Inouye, J. Goldwin, M. Olsen, C. Ticknor, J. Bohn, and D. Jin, "Observation of Heteronuclear Feshbach Resonances in a Mixture of Bosons and Fermions", Phys. Rev. Lett. **93**, p. 183201, (2004).

[61] F. Ferlaino, C. D'Errico, G. Roati, M. Zaccanti, M. Inguscio, G. Modugno, and A. Simoni, "Feshbach spectroscopy of a K-Rb atomic mixture", Phys. Rev. A **73**, no. 4, p. 040702, (2006).

[62] M. Zaccanti, C. D'Errico, F. Ferlaino, G. Roati, M. Inguscio, and G. Modugno, "Control of the interaction in a Fermi-Bose mixture", Phys. Rev. A **74**, no. 4, p. 041605, (2006).

[63] K.-K. Ni, S. Ospelkaus, M. De Miranda, A. Pe'er, B. Neyenhuis, J. Zirbel, S. Kotochigova, P. Julienne, D. Jin, and J. Ye, "A high phase-space-density gas of polar molecules", Science **322**, no. 5899, pp. 231–235, (2008).

[64] G. Modugno, G. Roati, F. Riboli, F. Ferlaino, R. J. Brecha, and M. Inguscio, "Collapse of Degenerate Fermi Gas", Science **297**, pp. 2240–2243, (2002).

[65] C. Ospelkaus, S. Ospelkaus, L. Humbert, P. Ernst, K. Sengstock, and K. Bongs, "Ultracold Heteronuclear Molecules in a 3D optical Lattice", Phys. Rev. Lett. **97**, p. 120402, (2006).

[66] S. Giorgini, L. P. Pitaevskii, and S. Stringari, "Condensate fraction and critical temperature of a trapped interacting Bose gas", Phys. Rev. A **54**, pp. R4633–R4636, (1996).